Master's thesis

NTNU
Norwegian University of Science and Technology
Faculty of Engineering
Department of Geoscience and Petroleum

Martin Valand Feldmann

Structural and lithological controls on Quaternary rock slope failures in the interior of the Devonian Hornelen basin, western Norway

Master's thesis in Geology
Supervisor: Reginald Hermanns
Co-supervisor: Ivanna Penna and François Noël
May 2021

NTNU
Kunnskap for en bedre verden

NORGES GEOLOGISKE UNDERSØKELSE
NGU

Martin Valand Feldmann

Structural and lithological controls on Quaternary rock slope failures in the interior of the Devonian Hornelen basin, western Norway

Master's thesis in Geology
Supervisor: Reginald Hermanns
Co-supervisor: Ivanna Penna and François Noël
May 2021

Norwegian University of Science and Technology
Faculty of Engineering
Department of Geoscience and Petroleum

NTNU
Norwegian University of
Science and Technology

Abstract

Aerial photographs reveal a large abundance of rock slope failure deposits on the Hennøy peninsula, located within the interior of Hornelen Devonian basin, Vestland county. East of Svelgen village, multiple relict rock avalanches rest along the Svelgsegga ridgeline with respective deposits fanning into the Svelgsvatnet lake. Open fractures along the slope reveal further rock slope deformation. This study aims to investigate the structural and lithological controls that control the distribution and abundance of rock slope failures on the peninsula.

Detection and mapping of geological structures and rock slope failure deposits was performed by combining field measurements and remote sensing on point cloud models. Resulting data led to the creation of a detailed, regional-scale landslide inventory and structural map for the Hennøy peninsula. Further structural analysis reveals a study-area wide consistency in the spatial distribution of discontinuities. The total structural composition of the peninsula can be attributed to five discontinuity sets (dipdir/dip): SS (122/33), J1 (033/83), J2 (292/78), J3 (354/86), J4 (303/35). Parallel to the bedding occur minor fault zones that transect the rock mass.

Furthermore, a detailed characterization of slide scars and deposits of rock slope failures was conducted, accounting for: topography, structural morphology and failure magnitude. Spatial and statistical analysis indicate that rock slope failure is not uniformly distributed. Rock slope failure exceeding (>10.000 m^3) are concentrated in the eastern portion of the field area, clustered on cataclinal dip-slopes. The orientation of the bedding is the strongest conditioning factor for rock slope failures exceeding 10.000 m^3, indicated by 93% of documented events failing along the bedding. Interpretation of slide scar morphology and spatial variability in structures suggests that clustering of failures exceeding 10.000 m^3 is also conditioned by the presence of the highly persistent discontinuity set J1 (033/83), acting as lateral flanks. This bedding-joint intersection form long wedge-shaped slide scars, involving most relict rock slope failures exceeding 10.000 m^2.

Rockfalls (<10.000 m^3) display an apparent clustering on southern and northwestern slope aspects. The distribution of rockfalls correlate to the distribution of steep slopes within the study area. On southern slopes kinematic feasibility tests indicate that rockfalls are mostly related to joint delimited direct toppling from steep cliff bands. Failure on northwestern aspects are largely facilitated by joint delimited wedge failure.

Lithological control on bedding conditioned failure exceeding 100.000 m^3 was further analyzed by probabilistic stability analysis according to Eurocode recommendations. Lab and in-situ testing of the rock mass defined the failure criterion applied in the modelling of rock mass strength. Analysis emphasize the degree of fracturing along the sub-vertical lateral structure and emplacement of bedding parallel minor faults as the most important controls on high magnitude bedding conditioned failure. Seismic loading additionally represent a feasible triggering mechanisms for failures.

Furthermore, three fracture delimited instabilities exceeding 100.000 m^3 were defined along the Svelgseggen ridgeline located west in the study area. InSAR data indicate no movement within either of the instabilities. It is recommended that a full hazard assessment is conducted to elaborate the conditions of stability and consequence for potential future failure.

Sammendrag

Flyfoto avslører en stor konsentrasjon av steinsprang og fjellskredavsetninger på Hennøy halvøya, tilhørende den indre delen av Hornelen devonbasseng i Vestland fylke. Øst for Svelgen bysentrum ligger Svelgsegga, hvor flere store skredarr etter fjellskred utspiller seg langs den sørøstvendte skråningen, med tilhørende avsetninger som munner ut i Svelgsvatnet. Åpne sprekker avslører ytterligere deformasjon og mulig ustabilitet. Denne studien har som mål å undersøke hvilke strukturelle og litologiske faktorer som tilrettelegger fordelingen og mengden av steinsprang og fjellskredavsetninger på halvøya.

Feltarbeid og ytterligere fjernmåling på punktskymodeller ligger til grunn for kartleggingen av geologiske strukturer og skredavsetninger. Datagrunnlaget ble brukt til å lage et detaljert regionalt strukturkart og skreddatabase. Videre strukturell analyse avslører en lav regional variasjon i den romlig fordelingen av diskontinuiteter. Den totale strukturelle sammensetningen på Hennøy halvøya kan beskrives av fem diskontinuitetssett (dipdir/dip): SS (122/33), J1 (033/83), J2 (292/78), J3 (354/86), J4 (303/35). Parallelt med den sedimentære lagningen opptrer forkastningssoner som danner tydelige sjikt i bergmassen.

Videre følger en detaljert karakterisering av kartlagte skredarr og avsetninger etter steinsprang og fjellskred i henhold til topografi, strukturell sammensetning og volum. Romlig og statistisk analyse viser at steinsprang- og fjellskredhendelser ikke er uniformt fordelt i studieområdet. Tar man skredenes volum i betrakting er det tydelig at skred med volum over 10.000 m^3 er konsentrert til den østlige delen av studieområdet på skråninger som er parallelle med den sedimentære langingen. Lagparallelle diskontinuiteter er videre gjenkjent som den viktigste kontrollerende faktoren for skredmasser over 10.000 m^3. Hele 93% av alle de dokumenterte skredhendelsene er gjenkjent som planutglidinger langs lagningen. Tolkninger av skredmorfologien og romlig fordeling av diskontinuiteter tilsier at fordelingen av skred med volum over 10.000 m^3 også er betinget av et svært utholdende sprekkesett J1 (033/83). Settet fungerer som lateral avgrensning for skredmassen og danner sammen med lagningen avlange skredarr som karakteriserer alle de kartlagte skredhendelsene med volum over 100.000 m^3.

Steinsprang viser til forskjell tydelig skjev romlig fordeling, med størst andel avsetninger på sørlig og nordvestlig orienterte skråninger. Fordelingen gjenspeiler den skjeve fordelingen av bratte skråninger innenfor studieområdet. Kinematisk analyse indikerer videre at steinsprang på sørlig orienterte skråninger kan relateres til sprekkeavgrenset utvelting. På nordøstlig orienterte skråninger er steinsprang i stor grad tilrettelagt av sprekkeavgrenset kileutglidning.

Den litologiske kontrollen for fjellskred ble videre analysert ved probabilistisk stabilitetsanalyse i henhold til Eurokode. Lab og in-situ testing av bergmassen ble gjennomført for å definere bruddkriterier for videre bruk i stabilitetsanalysen. Modelleringen presenterer sprekkeutviklingen langs den laterale J1 orienterte bruddflaten og lagningsparallelle forkastningssoner som de viktigste tilretteleggende faktorene for fjellskred. Seismisk last vektlegges videre som mulig utløsningsmekanisme for fjellskred.

Den morfologiske kartleggingen resulterte avslutningsvis til gjenkjenningen av tre sprekkeavgrensede ustabiliteter med volum over 100.000 m^3 langs den sørøstlige skråningen på Svelgsegga. InSAR analyse viser at det ikke forekommer signifikant bevegelse ved noen av ustabilitetene. Det anbefales at det videre gjennomføres en fareklassifisering for å fastslå stabilitetsforholdene og konsekvensene ved utrasing.

Preface

This work concludes my time as a Master of Science (M.sC) student in geology at the Norwegian University of Science and Technology (NTNU). The thesis was written in collaboration with NGU, supervised by Reginald Hermanns (NTNU/NGU), Ivanna Penna (NGU) and François Noël (NGU).

First of all I would like to thank my supervisor Reginald Hermanns and co-supervisors Ivanna Penna and François Noël for all the guidance and help you have given me throughout the process of writing my thesis. My largest gratitude goes out to all for the useful discussions and inputs I have received.

Secondly, I would like to thank Gunnar Vistnes (NTNU) and Jon Runar Drotninghaug (NTNU) for all the help I received in preparing rock samples and carrying out laboratory tests.

Gerben Boer and Børre Dyrkorn at Bremanger Quarry AS, you have my biggest gratitude for the unconditional access you gave us to your facilities. Our findings turned out to be crucially important for the concluding remarks of the thesis.

Lastly I would like to thank my eminent study partner, field assistant, but most of all good friend Sondre Svevad. Thanks for all the experiences I have had the pleasure of shearing with you over the years. Forever fondly I will remember the warm sunsets at Stokkrå and likewise adventurous afternoons on the horn of Hennøya. It has all been a great adventure, with more to come.

I am all so thankful for getting the opportunity to study one of my greatest fascinations in life: the mountains.

Trodheim, 10.05.21

Table of contents

Abbreviations

ALS	Aerial laser scan
COV	Coefficient of variation
DEM	Digital elevation model
DSB	Norwegian Directorate for Public Safety
FS	Factor of safety
GIS	Geographic information system
GSI	Geological strength index
JCS	Joint compressive strength
JRC	Joint roughness coefficient
LEM	Limit equilibrium
NGU	Geological Survey of Norway
NVE	Norwegian Water Resources and Energy Directorate
PBL	The planning and building act
TLS	Terrestrial laser scan
TOBIA	Topographic Bedding plane Intersection Angle
UCS	Uniaxial compressive strength

1 Introduction

1.1 General introduction

Landsliding is an integral part of the Norwegian landscape development. Steep slopes where rock-slope failures takes place correspond to deeply incised valleys and fjords, mostly west of the Scandes**.** Adverse climate conditions and the large spread of the Norwegian population settling in most valleys and fjords, has resulted in excess of 4000 landslide related fatalities in historic time (Hermanns et al., 2013a). Rock slope failures have the second largest fatality rate of all mass movements in the last century in Norway, only surpassed by snow avalanches.

Rock avalanches and resulting displacement waves when rock avalanches impact water bodies poses among the most serious landslide related hazards in western Norway. Within the last century three large events (Loen in 1905 and 1936) and (Tafjord in 1934) resulted in 175 total casualties (Blikra et al., 2006). Damming of valleys by landslides and subsequent dam burst with downstream flooding are another important hazard that caused substantial historic casualties. Of the largest rock slope failures in recorded history are secondary effects accounting for 80% of the total fatalities (Hermanns et al., 2013a).

The Geological Survey of Norway (NGU) is tasked with mapping all potentially unstable rock slopes in Norway, financed by the Norwegian Water and Energy Directorate (NVE). More than 500 unstable slopes has been identified within Norway, recording post-glacial deformation. The rock slope deformations is located mostly north of Narvik and South of Trondheim (Hermanns et al., 2013b). Although smaller in volume and scope, rockfalls ("steinsprang" and "steinskred") still pose a risk for people and infrastructure. Its frequency is magnitudes larger than for rock avalanches (daily/weekly frequency), resulting in multiple road closures a year. Rockfalls additionally pose a hazard in urban areas and can strike settlements directly (Devoli et al., 2011).

The prospects of increasing urbanization in landslide susceptible areas requires an increased knowledge of landslide dynamics to ensure the safety of communities and infrastructure. This became largely evident from the recent tragic quick clay flow-slide in Gjerdrum of 2020 and Jølster debris flows of 2019, resulting in respectively 10 and 1 fatalities and substantial economic losses. NVE and NGU are tasked with supplying mapping, databases, method development and expertise (Hermanns et al., 2013a) and therefore hold an important responsibility. Therefore, as the central research based administrative agency in geoscientific matters, developing an increased understanding of landslide dynamics is a part of NGUs contribution to the Norwegian model. This master thesis follow this objective, aiming to contribute to the increased understanding of the stability of rock slopes.

After inspection of aerial photographs of the Hennøy peninsula, Vestland county it became apparent that the region holds a large abundance of rock slope failure deposits. East of Svelgen village, multiple relict rock avalanches rest along the Svelgsegga ridgeline with respective deposits fanning into the Svelgsvatnet lake. Open fractures along the slope reveal the presence of further rock slope deformation.

1.2 Aim of Study

This study aims to investigate the structural and lithological controls for rock slope failures along the Hennøy peninsula and how the geometrical interaction with topographic factors influence the size, mode, and distribution of failure.

The detection and mapping of geological structures and rock slope failure deposits will be performed by combining field measurements and remote sensing on point cloud models. Resulting data are then to be used in the creation of a detailed regional-scale landslide inventory and structural map for the Hennøy peninsula. Multiple methodologies will be incorporated to unveil topographical and structural factors influencing spatial distribution and abundance of failures. This includes a detailed characterization of slide scars and deposits of rock slope failures, accounting for topography, structural morphology and failure magnitude. Kinematic analysis and the construction of structural profiles will further be used to investigate feasible failure modes for rock slope failure.

Lastly a probabilistic stability analysis according to Eurocode recommendations will focus on the lithological control of rock slides. The model will incorporate results from lab and in-situ testing of rock mass strength.

1.3 Introduction to area

Western Norway is regionally characterizable by glacially steepened U-shaped valleys reaching below sea level shaped by the multiple glacial cycles of the Quaternary and subsequent isostatic rebound, forming the many fjords of the Sogn og Fjordane region. High relief slopes combined with the large concentration of structures formed from both tectonics and glacial unloading facilitate the formation of large gravitational rock-slope deformations (Ballantyne, 2002). Due to the large abundance of large, historical rock slope failures Sogn and Fjordane county is thus in the high priority bracket of the national systematic mapping of unstable rock slopes in Norway, conducted by NGU (Hermanns et al., 2013b).

The study area is located northernmost in Vestland county (former Sogn og Fjordane county) in the municipality of Bremanger on the Hennøy peninsula. Located in between the coastal cities of Måløy and Florø, the peninsula forms the division of the Frøysjøen and Nordgulen fjord arms. Innermost in the Nordgulen fjord lies the village of Svelgen, home to about 1100 residents and holding a large smelting plant. Field mapping was concentrated to the southern edge of the peninsula (*figure 1.1*).

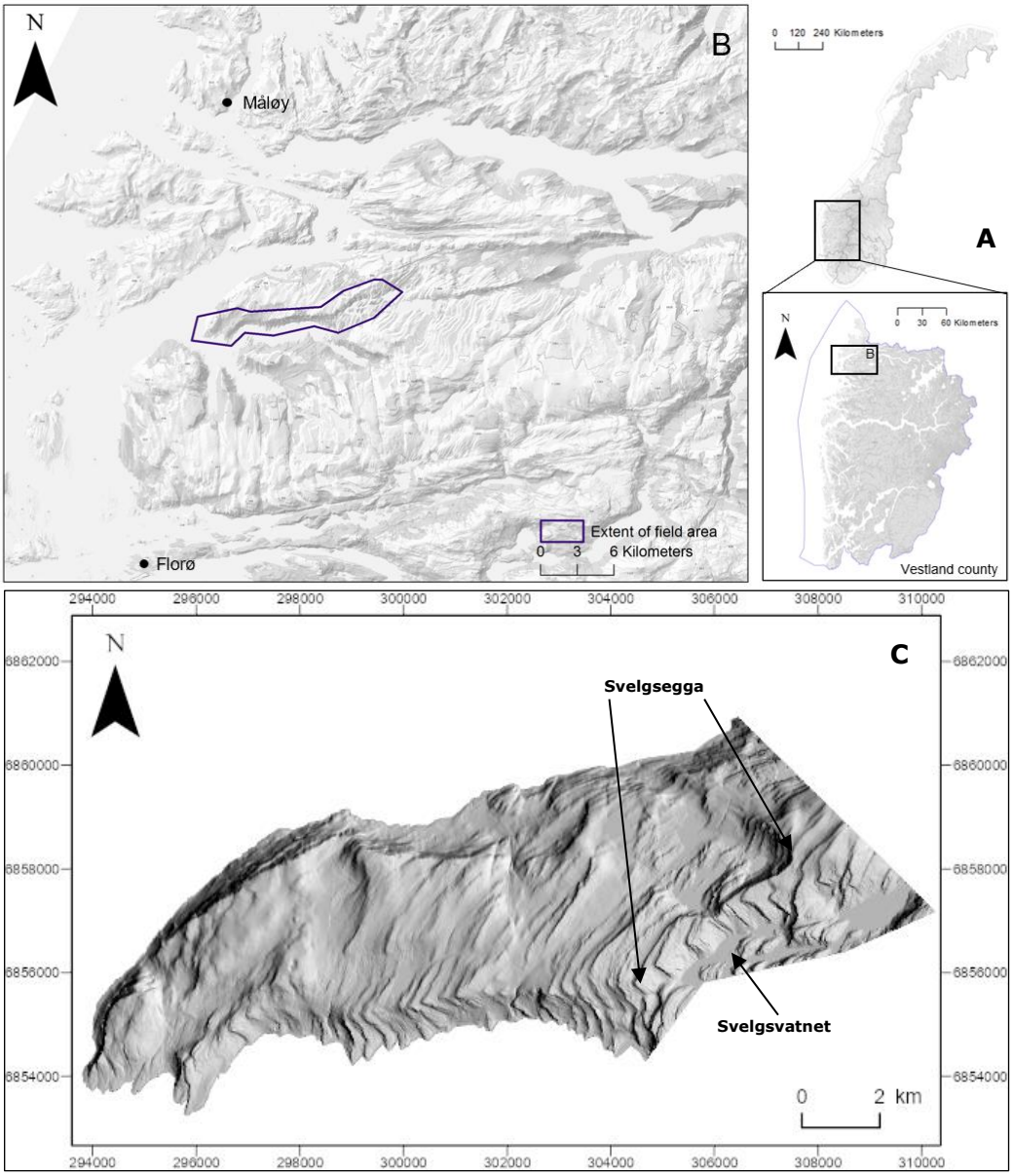

Figure 1.1 *(A and B) Placement of the field area. (C) 10 m DEM covering the study area.*

1.4 Regional setting

Hornelen Basin forms the largest and northernmost of the four Devonian basins of western Norway. Located in between Sognefjord and Nordfjord, they are from N-S comprised of the Hornelen-, Håsteinen-, Kvamshesten- and Solund basins (figure 1.2). Important for the total understanding of the tectonic evolution of Western Norway, basin development and its inherent structural and sedimentological fabrics have been studied in detail (Steel, 1976, Bryhni, 1978, Norton, 1987, Seranne and Seguret, 1987, Wilks and Cuthbert, 1994, Odling and Larsen, 2000)

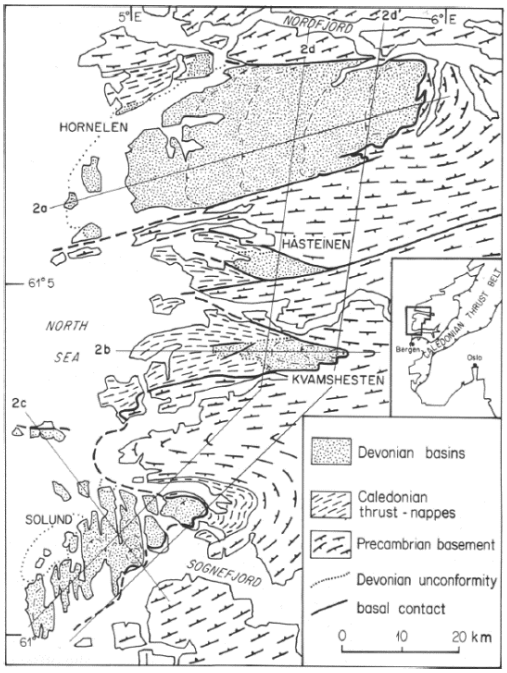

Figure 1.2 *Generalized geological map of the Devonian basins of western Norway (Seranne and Seguret, 1987)*

Formation of Devonian sedimentary basins in Western Norway closely relates to the crustal scale, extensional re-arrangement of the orogenic belt following the Caledonian orogeny (Fossen, 1992, Norton, 1987, Seranne and Seguret, 1987). Regional structural and kinematic analysis reveals two related styles of extension. Firstly, characterized by ductile deformation and a NW to W directed extensional reactivation of thrust zones, later stages involved the formation of mylonitic, W-dipping detachment zones penetrating the entire tectono-stratigraphy (Fossen, 1992). Sinistral, top-to-the W displacement under progressively more brittle conditions resulted in the emplacement of the younger strata in the hanging wall juxtaposed to the eclogite-bearing autochthonous basement in the foot wall. Most prominent of these zones within Western Norway is the low-angle Nordfjord-Sogn detachment zone (NSD) (Norton, 1987). It is largely understood that the associated extension and subsidiary faults facilitated the deposition of non-marine middle Devonian sediments in the hanging wall, following extensional half-graben geometries in sections parallel to the direction of principal extension (Steel, 1976).

The Hardangerfjord Shear Zone and Bergen Arc Shear Zone represents similar detachments within western Norway (Fossen, 1992). In likeness to the NSD, the Bergen Arc Shear Zone similarly juxtapose eclogite-grade metamorphic rocks in the foot wall to the Caledonian nappes and Devonian sedimentary rocks in the hanging wall. Due to their adjacency and similar characteristics, the Bergen Arc Shear Zone is suggested to represent a southward extension of the NSD (Fossen, 1992, Wennberg et al., 1998), underlining the probable regional significance of the structure.

Hornelen basin represents the largest of the four Devonian basins and spans an area of roughly 75 km by 20 km. Mainly consisting of sandstone and minor siltstones in the interior, marginal conglomerate fans and breccias at the fringes together comprise the Hornelen group (Bryhni, 1978). Meter thick beds form 50-200 m laterally continuous, mostly coarsening upwards cycles (Steel, 1976, Bryhni, 1978). The repetitive nature of these cycles suggests syntectonic sedimentation, controlled by the successive

displacement along the NSD resulting in discrete and relatively rapid basin-floor subsidence. Displacement related rollover probably caused tilting of the strata, creating a constant dip of approximately 25° within the interior of the basin (Seranne and Seguret, 1987) (*figure 1.3*). The present-day exposure is fault bounded on all sides except to the W, here unconformably resting on Cambro-Silurian metamorphic rocks. High levels of the NSD makes up the E-margin of the Hornelen basin, occurring as a W-dipping low-angle brittle extensional fault, timely named the Hornelen detachment (Dewey et al., 1993, Wilks and Cuthbert, 1994). N- and S margins are delimited by steeply dipping oblique/strike-slip fault segments striking parallel to the basin axis (Wilks and Cuthbert, 1994) (*figure 1.4*).

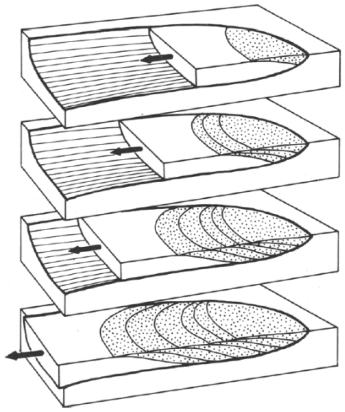

Figure 1.3 *Schematic illustrating successive basin development and consequent back-tilting of strata. No scale applied (Seranne and Seguret, 1987).*

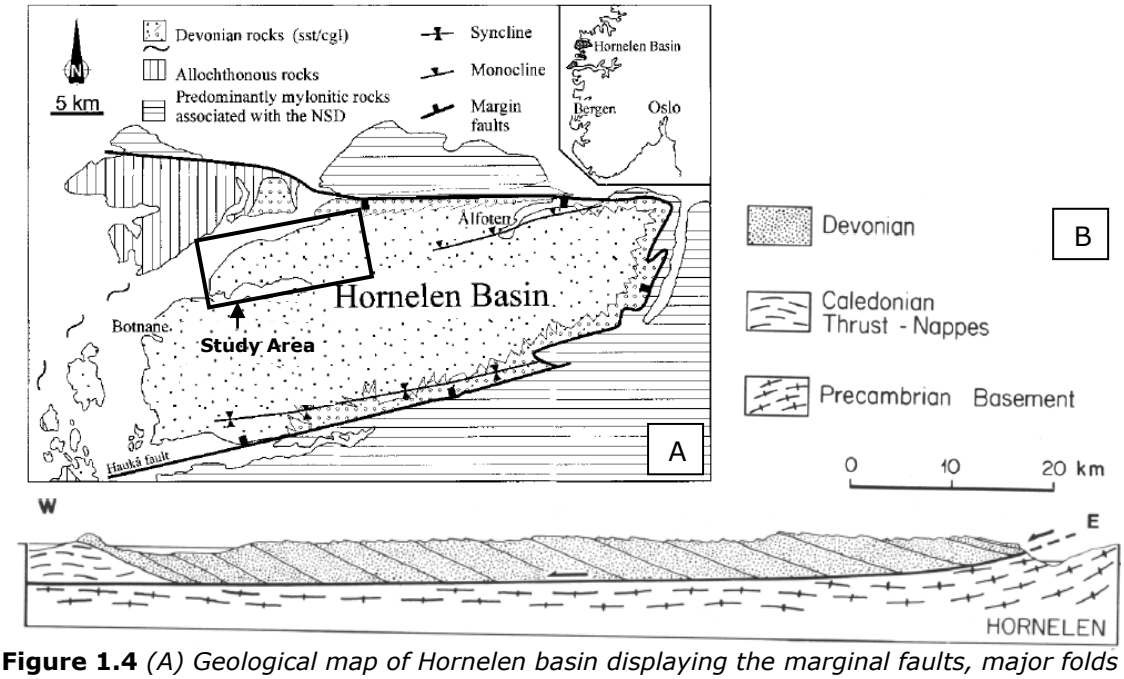

Figure 1.4 *(A) Geological map of Hornelen basin displaying the marginal faults, major folds and location of the study area. (B) Longitudinal cross-section of the Hornelen Basin. Transect of the profile is indicated as 2a in figure 1.2. Modified from Seranne and Seguret, 1987 and Odling and Larsen (2000).*

Deformation of the basin is closely related to the overall strain history of Western Norway and can roughly be roughly grouped after the (1) collapse of the Caledonites and in the Early to Middle Devonian and (2) the rifting of offshore Norway in the Late Devonian to Mesozoic (Seranne and Seguret, 1987, Wilks and Cuthbert, 1994, Odling and Larsen, 2000). Based on a review of current literature, a brief synthesis of the deformational evolution of Hornelen Basin is hereunder presented:

Dated to the Middle Devonian, deposition was tectonically controlled by the aforementioned top-to-the W extension of the NSD. Exposures at the basal contact at lower erosional levels reveals ductile fabrics, presenting a continuous section from relatively undeformed sediments in the top to ductile shearing at the basal contact. The present-day exposure dominantly displays lower greenschist metamorphism. Internal deformation in the upper strata of the basin was largely accommodated by brittle interbed dip-slip, recorded as fine cleavage and minor faults in the present-day interior of Hornelen basin (Øvstedal, 1971, Seranne and Seguret, 1987). Deformational band style faulting created cataclasites before the strata was fully lithified to the present-day state, likely before the basin reached its maximum thickness (Odling and Larsen, 2000).

Early stages of Late Devonian to Early Carboniferious age are suggested to involve N-S shortening and E-W extension (Hartz and Andresen, 1997, Osmundsen et al., 1998, Braathen, 1999, Odling and Larsen, 2000). At this time, the basin had already reached its maximum thickness and probably lithified to present-day state (Odling and Larsen, 2000). The present day-exposure display low-grade metamorphism, bordering greenschist facies (Seranne and Seguret, 1987, Wilks and Cuthbert, 1994), thought to be associated with the later stages of N-S compression (Seranne and Seguret, 1987). It is suggested that the emplacement of E-W trending folds near the N and S basinal margins is related to the Late Devonian to Early Carboniferious compression (Osmundsen et al., 1998, Torsvik et al., 1988, Eide et al., 1999), although this is the matter of some debate. Evidence of tight folds of the same orientation in the underlying autochthon (Krabbendam and Dewey, 1998) and interpretations of sedimentary features as unconformities adjacent to bounding faults (Seranne and Seguret, 1987) could imply folding to be in part syn-depositional in age.

Rapid exhumation in the Early Carboniferous generated early veins and breccias along preexisting weakness zones under low differential stress (Eide et al., 1997, 1999). Late Permian to Triassic marks a shift in the stress field, rotating the extensional direction from NW-SE to WSW-ENE (Andersen et al., 1997, Fossen, 1998, Fossen and Dunlap, 1999), producing fibrous veins (Odling and Larsen, 2000). Late vein assemblages suggest that the rate of exhumation had slowed. Differential stress had then increased probably as response to the North Sea rifting event. Continued exhumation to present day has resulted in complex jointing system. Latter joints are largely unmineralized due to restricted fluid flow and low temperatures (Odling and Larsen, 2000).

2 Theory

2.1 Rock slope failure

Landslides are classified in a large variety of ways. The most common classification systems are categorized according to volume, movement type or material type, mostly dependent on the field of study. One of the most commonly applied systems in the study of landslides is the Varnes (1978) classification system, modified by Hungr et al. (2014). The system is structured in terms om movement type and differentiates bedrock from engineering soil. Movement is divided into six categories: fall, topple, slide, spread, flow and complex slope movements (*figure 2.1*).

Variation also exists in the definition and classification of rock slope failures. This thesis will follow the definition according to Böhme (2014), defining a rock slope failure as: "complete failure of a rock mass resulting in gravitational mass movements down a mountain slope". Rockfalls are hereunder small rock slope failures, involving rapid free falling, bouncing, and sliding movement downslope (Böhme et al., 2013). Rockslides are proportionally larger and involve sliding along a basal failure surface. The catastrophic failure of a rockslide may lead to a rock avalanche, defined as a stream of rapidly moving debris originating from the disintegration of a failed rock mass and reaching long run-outs (Heim, 1932). The Norwegian approach for categorizing rock slope failures relates to the volume of the failed mass. Volume classification is applied by all major actors, including the Norwegian Geotechnical Institute (NGI), NGU and NVE, although grouping vary. NGI distinguish between rockfalls (steinsprang) and rock avalanches (fjellskred) at a threshold value of 10.000 m^3 (Høeg et al., 2014), whereas NGU apply 100.000 m^3, more in line with international literature (Devoli et al., 2011). NVE add "steinskred" in the magnitude range 100 m^3 to 100.000 m^3 to facilitate the transition in transport mode from rockfalls to rock avalanches (NVE, 2019).

This thesis follow a somewhat modified version of the NGU definition. Rock avalanches are accordingly defined as failures exceeding 100.000 m^3 in volume. Additionally, the extra class of rock slope collapse was incorporated to refer to failures in the range of 10.000 to 100.000 m^3. Failures of volumes below 10.000 are defined as rockfalls m^3

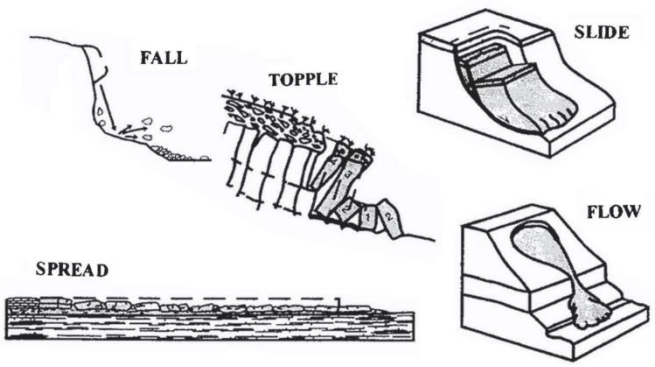

Figure 2.1 *Types of landslide movements, modified by Nicolet (2017) from Cruden and Varnes (1996) and Hungr et al. (2014)*

2.2 Controlling factors for rock slope instability and failure

The stability and magnitude of rock slopes and related rock slope failures are controlled by a large variety of internal and environmental factors. Jaboyedoff et al. (2005) presents a theoretical overview of factors influencing the stability of rock slopes according to internal and external factors. Internal factors include slope morphology, geological and structural properties of the bedrock. These parameters may be altered over time by external factors, including climactic factors, active tectonics and more (*figure 2.2*). The magnitude of influence towards stability is varying. Orientation of discontinuities and groundwater are described by Grøneng (2010) as most important for large rock slope failures in Norway.

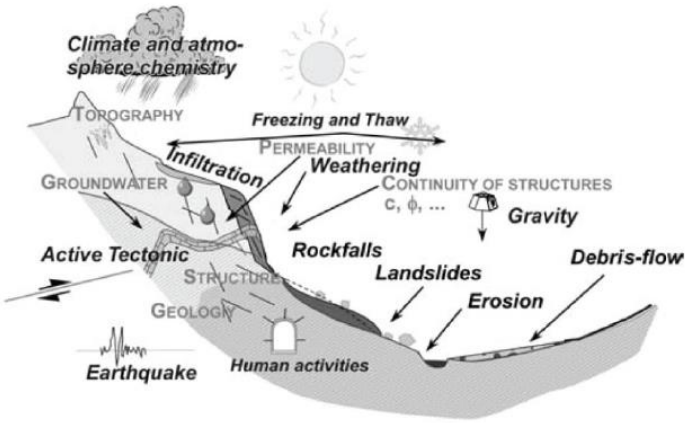

Figure 2.2 *Internal and external factors that may influence rock slope stability according to Jaboyedoff et al. (2005)*

Water affect stability in various ways. Decreased normal stress on the failure plane and failed rock mass induce proportional reduction in shear strength (Wyllie, 2004). Permafrost pose as an important control on rock slope instabilities in cold mountain settings. It is generally accepted that where ice is precent in discontinuities it contributes to maintaining the stability of the slope (Bjerrum and Jrstad, 1968). Permafrost degradation and ice thaw is thus an important control for large rock slope failures in high-mountain and polar regions (Huggel et al., 2010, Blikra and Christiansen, 2014). Freeze-thaw related joint expansion will additionally facilitate smaller rock slope failures in cold temperate climates (Grøneng, 2010).

On the matter of discontinuities, orientation is most important for rock slope stability (Wyllie, 2004). For failure by sliding, dip angle exceeding the friction angle and downslope daylighting of the discontinuity are important for lateral conditions (Hermanns et al., 2012). Joint characteristics, including joint spacing and persistence also influence both the magnitude and stability of rock slope instabilities (Wyllie, 2004). Other modes of failure are also considered and will be further described in section 3.4.

Large, catastrophic rock slope failures are mostly preceded by a phase of slow deformation. Both ductile and brittle creep facilitate this internal deformation of the rock mass. The deformational style of a given rock mass is largely dependent on its ductile potential. Rock masses with large e-modulus is generally known to facilitate large deformation prior to failure (Stead et al., 2006). Acceleration in creep movement is recognized as the most important indicator of impending catastrophic failure and is

integral in rock avalanche monitoring (Hermanns et al., 2012, Loew et al., 2017, Kristensen et al., 2021).

2.2.1 Terzaghi's condition for stability in stratified sedimentary rock slopes

The work of Terzaghi (1962) presents a particular mechanical model for stratified sedimentary slopes based on an inherent fabric. This model is built on the assumption that bedding planes are invariably surfaces of minimum shearing resistance and likely to be continuous over large distances. Commonly occurring cross joints striking sub-perpendicular to the bedding is also assumed to hold no cohesive bonds along the walls. Due to the almost universal presence of bedding and cross joints, stratified sedimentary rocks with no cohesion (c=0) will in its simplest form have the mechanical properties of dry masonry, formed by the interlocking rock blocks. Stability of such a rock slope with the given mechanical profile will according to Terzaghi (1962) depend primarily on the orientation of the bedding planes with reference to the slope. This forms the basis for the critical slope angle β_c, a threshold dip angle for a bedding plane for sliding of the rock mass to occur. In discussing the critical slope angle β_c the geometrical relation of slope orientation and bedding can be evaluated in terms of cataclinal and anaclinal slopes (*figure 2.3*).

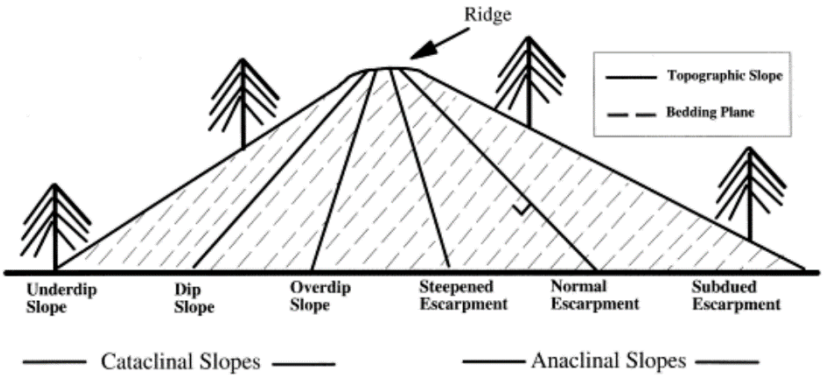

Figure 2.3 *Classification of anaclinal and cataclinal slopes after Meentemeyer and Moody (2000) Thick lines are slope surfaces and thin lines represent trace of bedding. Orientation of the six slopes are plotted in figure 2.4 (Cruden, 2003).*

Young (1975) further implies that the critical slope angle is dependent on the relative spacing and offset of bedding and cross joints. Following the assumptions made by Terzaghi (1962), the critical slope can thus be defined according to *equation 2.1*, where ψ is the dip of the bedding, C is the offset between kathetal joints in successive beds of thickness, D.

$$\beta_c = (90 - \psi) + \tan^{-1}\left(\frac{C}{D}\right) \qquad 2.1$$

The work of Cruden (2003) reviews the possibility of toppling and buckling, further narrowing the stability condition of the slope. Toppling can occur away from steeply dipping bedding on anaclinal slopes or steeply dipping bedding on anaclinal slopes. On steep slopes the largest principal stress acts down-slope and slip on the bedding will occur if the conditions of *equation 2.2* are met (Goodman, 1976). On steep, under-dip, cataclinal slopes where bedding dips under-slope shear will here be possible along the bedding according to *equation 2.3* (Cruden, 1989). Parameter φ is the rock mass friction angle.

$$\beta \geq \varphi + (90 - \Psi) \quad 2.2$$

$$\beta \geq \varphi - (90 - \Psi) \quad 2.3$$

Combining these principles, processes on anaclinal and cataclinal slopes can be considered in terms of slope angle β, bedding dip Ψ and basic friction angle φ_b (Cruden, 2003) (*figure 2.4*)

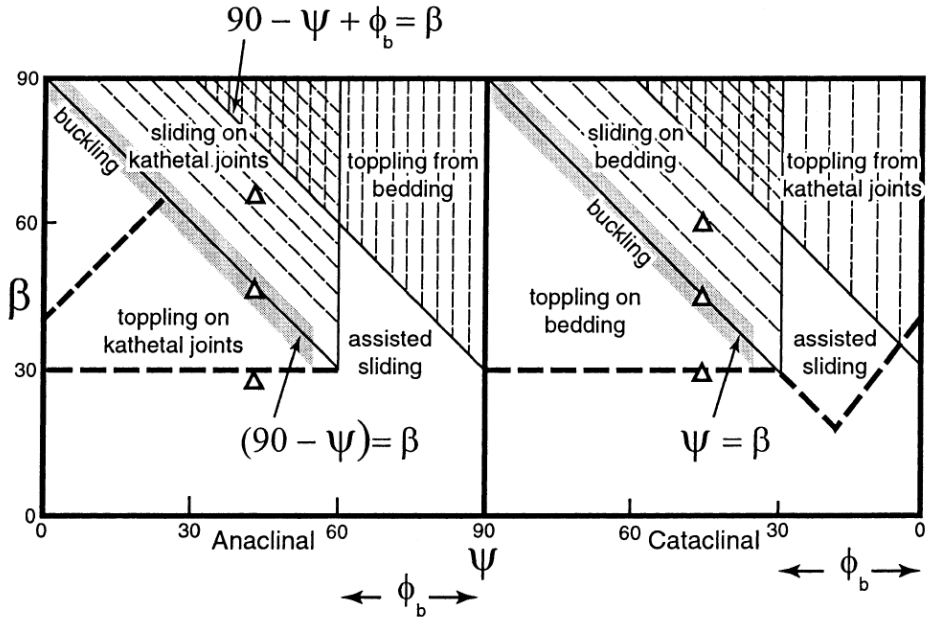

Figure 2.4 *Processes on anaclinal and cataclinal slopes in terms of slope angle β, bedding dip ψ, and basic friction angle φ_b. The six slopes from fig. The six slopes of figure 2.3 are plotted as triangles. Heavy dashed lines represents the hypothesized lower boundary to the failure conditions (Cruden, 2003).*

2.2.2 Spatial controlling parameters

As pointed out by Böhme (2014) statistical analysis of spatial controlling parameters of large rock slope failures are rather rare and challenged by the relatively small inventory dataset often resulting in statistically non-significant spatial relations. Existing studies therefore mainly focus on descriptive statistics, comparing the characteristics of rock slope instability or past failure of all magnitudes to the environmental characteristics of their surrounding area. Pedrazzini (2012) and Pedrazzini et al. (2016) highlights a strong spatial relation between large rock slope deformations in the Rhone valley, Switzerland and existing tectonic structures, orientation of main foliation, high local relief, high uplift gradient and high seismic release energy. Santaneglo et al. (2015) specifically focus on the role of beddings in controlling the distribution and abundance of landslides in the of the Umbria region, Central Italy. The study presents significant evidence related to bedding conditions control on the location and abundance of relict and deep-seated slides. The study finds failures most abundant on cataclinal slopes.

For rockfalls the feasibility of statistical studies is naturally exponentially larger and the distribution of rockfalls in relation to controlling factors is thus more readily discussed (Menéndez-Duarte and Marquínez, 2002, Ruff and Czurda, 2008, Tanarro and Muñoz, 2012). The resulting parameters and their influence on regional spatial variability is used for statistical and probabilistic modelling techniques to predict rockfall source areas, used in susceptibility maps (Marzorati et al., 2002, Marquinez et al., 2003, Zahiri et al., 2006,

Frattini et al., 2008, Blais-Stevens et al., 2012, Shirzadi et al., 2012). Major controls in these studies were lithology, slope angle, bedding, tectonic structures, and morphology.

2.2.3 Influence of deglaciation on rock-slope stability

Throughout the Quaternary, Norway experienced multiple events of glacial advance and retreat, resulting in periods of glacial erosion and paraglacial rock slope adjustment. This released large quantities of rock debris in the form of rock avalanches, rockslides and rockfall talus deposits (Ballantyne, 2002). Most existing rock slope failure deposits in Norway belong to the period after last deglaciation (Böhme et al., 2015, Hermanns et al., 2017). Additionally, the latter also resulted in the weakening of surviving rock slopes. Deglaciation affects the stability of rock slopes in numerous ways but can largely be attributed to the (1) oversteepening of rock walls due to erosion, (2) glacier retreat related debutressing of valley walls and (3) associated isostatic uplift (Ballantyne, 2002, Grämiger et al., 2016).

Glacial erosion will characteristically reshape V-shaped valley cross sections into U-shaped valleys, exhibiting steeper wall configurations (Harbor et al., 1988). Steepening and heightening will lead to a natural increase in gravitationally induced shear stress acting within the rock mass (Radbruch-Hall, 1978). The increase in the in-situ stress field leads to failure after deglaciation if the applied stress exceeds the rock mass strength. In the case of glacial retreat, the removal of support on rock slopes will result in the redistribution of internal stresses and can thus induce rock slope failure (Evans and Clague, 1994, Haeberli, 1997, Selby et al., 1988). In valley environments ice-load causes a compression normal to the induced stress vector, that leads to elastic deformation in most rock types and thereby store residual strain energy. Consequent unloading therefore cause a proportional strain energy release (Ballantyne, 2002). This will typically induce a tensile stress region behind the slope, facilitating stress release in favorably oriented pre-existing weakness zones or by the formation of new joints. This stress related relaxation may lead to the destabilization of rock slopes, including the local expansion of rock joints (Geertsema et al., 2006, Ballantyne et al., 2014, Grämiger et al., 2016).

The effect of glacio-isostatic uplift is less discussed, although presumed to play a part in the destabilization of rock slopes due to the increase in relief (Galadini, 2006, Martino et al., 2004). Ice loading causes an elastic flexural response of the lithosphere proportional to the load (MacGregor et al., 2009, Persaud and Pfiffner, 2004). Subsequent response to ice removal is a gradual return of the down warped areas of ice loaded crust towards its pre-loading state. These uplift rates can be comparatively large in relation to tectonic uplift rates, exceeding 6 mm/yr in central Norway (Vestøl, 2006). Henderson and Saintot (2011) present a clustering of historical gravitational slope failures and instabilities at large uplift gradients within a transect of Møre og Romsdal county, Western Norway.

2.3 Rock mass strength and shear strength of discontinuities

The Mohr-Coulomb failure criterion is one of the most central pillars in the understanding of mechanical behavior of a material. According to Coloumb's law the shear strength τ of the material increase according to the normal stress σ_n acting on a discrete failure plane. This linear relationship is described in terms of the materials cohesion c and friction angle φ (Wyllie, 2004) (*equation 2.4*). When straining a material, the internal shear stress will increase rapidly until the peak strength is reached. This corresponds to the strength of the cohesion binding the two planar surfaces and the planar frictional resistance. After

initial failure, displacement will be accommodated at a residual stress value that will remain constant even for large shear displacements (c=0). When plotting peak residual strength at different normal stress for planar discontinuity surfaces the datapoints will generally fall along a straight line (*figure 2.5*) (Hoek, 2000).

$$\tau = c + \sigma_n tan\varphi \qquad 2.4$$

This theoretical relation described by the Mohr-Coloumb failure criterion has later been modified and expanded to adapt to the non-linear material characteristics observed in rock mechanical testing.

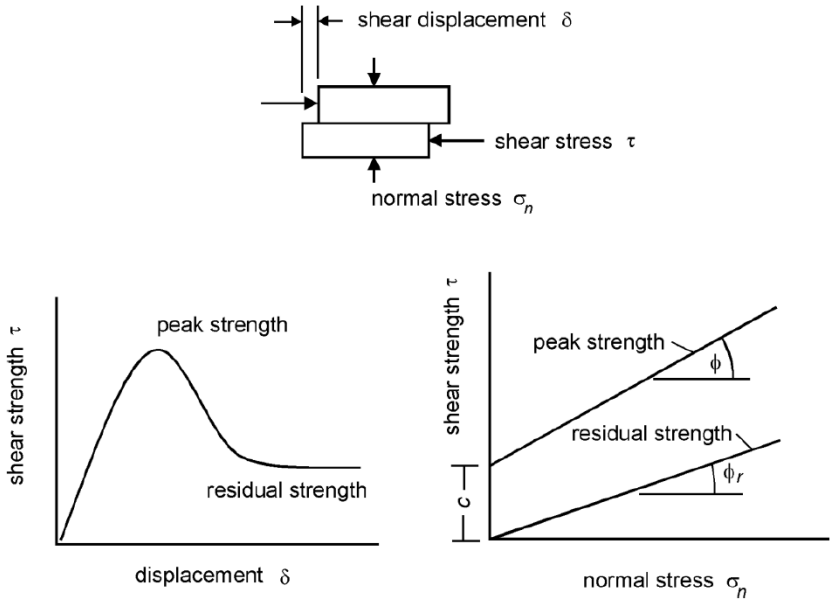

Figure 2.5 *Ideal behavior in shear testing of discontinuities according to Coulomb's law (Hoek, 2000).*

2.3.1 Barton's estimate of shear strenght

To accommodate the apparent strengthening effect of undulations and irregularities on jointed rock surfaces, Patton (1966) assumed an increase according to the planar roughness (*equation 2.5*).

$$\tau = \sigma_n \tan(\varphi_b + i) \qquad 2.5$$

Parameter i describes the inclination of assumed faceted saw-toothed irregularities and φ_b is the basis friction angle. This relation indicates a linear increase, more in line with the description of an intact rock mass rather than the characteristics of a fracture plane. In a fracture plane an increase in normal stress will break down asperities according to the internal strength of the rock. To better accommodate this apparent non-linear relationship Barton (1973) and Barton (1976), later revised by Barton and Choubey (1977) present the relation outlined in *equation 2.6*.

$$\tau = \sigma_n \tan\left(\varphi_r + JRClog\left(\frac{JCS_n}{\sigma_n}\right)\right) \qquad 2.6$$

The friction term is here formed by the residual friction angle φ_r , as well as a joint roughness coefficient JRC and joint compressive strength coefficient JCS.

The Joint roughness coefficient JRC quantifies the roughness of a sliding plane according to an empirical index based on the maximum amplitude of planar asperities in relation to a profile length (Barton and Bandis, 1982). Joint compressive strength JCS aims to quantify the compressive strength of the rock wall. In the case of relatively non weathered rock surfaces UCS can be considered as proportional to the JCS value. On more weathered surfaces the strength reduction can be adequately accounted for by easy field measurements

2.3.2 Hoek-Brown failure criterion

The Hoek-Brown criterion was originally outlined by Hoek and Brown (1980, 1980b) and later revised by Hoek et al. (2002) to be better accommodated for the use in numerical modelling. The criterion is based on an empirical relation describes the non-linear relation of confining pressure and rock strength. The generalized Hoek-Brown failure criterion for jointed rock masses is defined according to *equation 2.7*.

$$\sigma_1^{'} = \sigma_3^{'} + \sigma_{ci}\left(m_b\frac{\sigma_3^{'}}{\sigma_{ci}} + s\right)^a \qquad 2.7$$

Parameters σ_1' and σ_3' are maximum and minimum principals stresses at failure, s and a are material constants dependent on the rock mass characteristics, σ_{ci} is the uniaxial compressive strength of an intact rock sample and m_b is the value of the Hoek-Brown constant m for the rock mass. For an intact rock mass the relation can be rewritten according to *equation 2.8*.

$$\sigma_1' = \sigma_3' + \sigma_{ci}\left(m_i\frac{\sigma_3'}{\sigma_{ci}} + 1\right)^{0,5} \qquad 2.8$$

The relation between principle stresses at failure can thus be described in terms of σ_{ci} and material constant m_i. Hoek (2000) recommends these parameters to be determined through statistical analysis of triaxial tests.

Parameters s and a are dependent of the rock mass characteristics and its degree of fracturing, represented by the Geological Strength Index GSI (*equation 2.9 and 2.10*).

$$s = e^{\frac{GSI-100}{28-D}} \qquad 2.9$$

$$a = \frac{1}{2} + \frac{1}{6}\left(e^{\frac{-GSI}{15}} - e^{\frac{-20}{3}}\right) \qquad 2.10$$

D is the disturbance factor, describing the degree of blast damage on the rock mass. In the Hoek-Brown criterion, the constant a is replaced by the value 0,5. Parameter m_i is additionally adjusted according to GSI according to *equation 2.11*, represented by m_b.

$$m_b = m_i \exp\left(\frac{GSI-100}{24-14D}\right) \qquad 2.11$$

Although the criterion is readily applied in rock engineering it is important to be aware its limitations of use. An important assumption made regarding the estimation of rock strength is that the rock mass is isotropic and behaves isotropic under stress. The criterion is therefore not appropriate for use when the block size is on the same magnitude as the structures, or in rock masses with a clearly defined orientation of a main structure (Hoek, 2000) (*figure 2.6*).

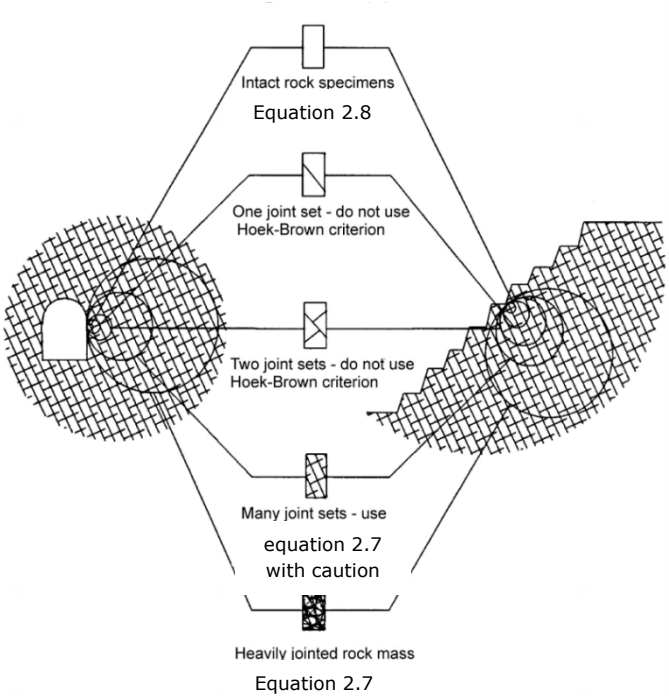

Figure 2.6 *Idealized diagram showing the transition from intact to heavily jointed rock mass and remarks on the appropriate use of the Hoek-Brown failure criterion (Hoek, 2000).*

2.3.3 Geological Strength Index

Geological Strength Index is a tool introduced by for the characterization of rock mass in relation to jointing and weathering of joints. Combined together with the intact rock properties it is used for estimating the reduction in rock mass strength for different geological conditions. The chart presented in *figure 2.7* applies for the characterization of GSI on blocky rock masses. In cases where discontinuity spacing is large compared to the dimensions of the slope, neither GSI nor the Hoek-Brown criterion should be applied.

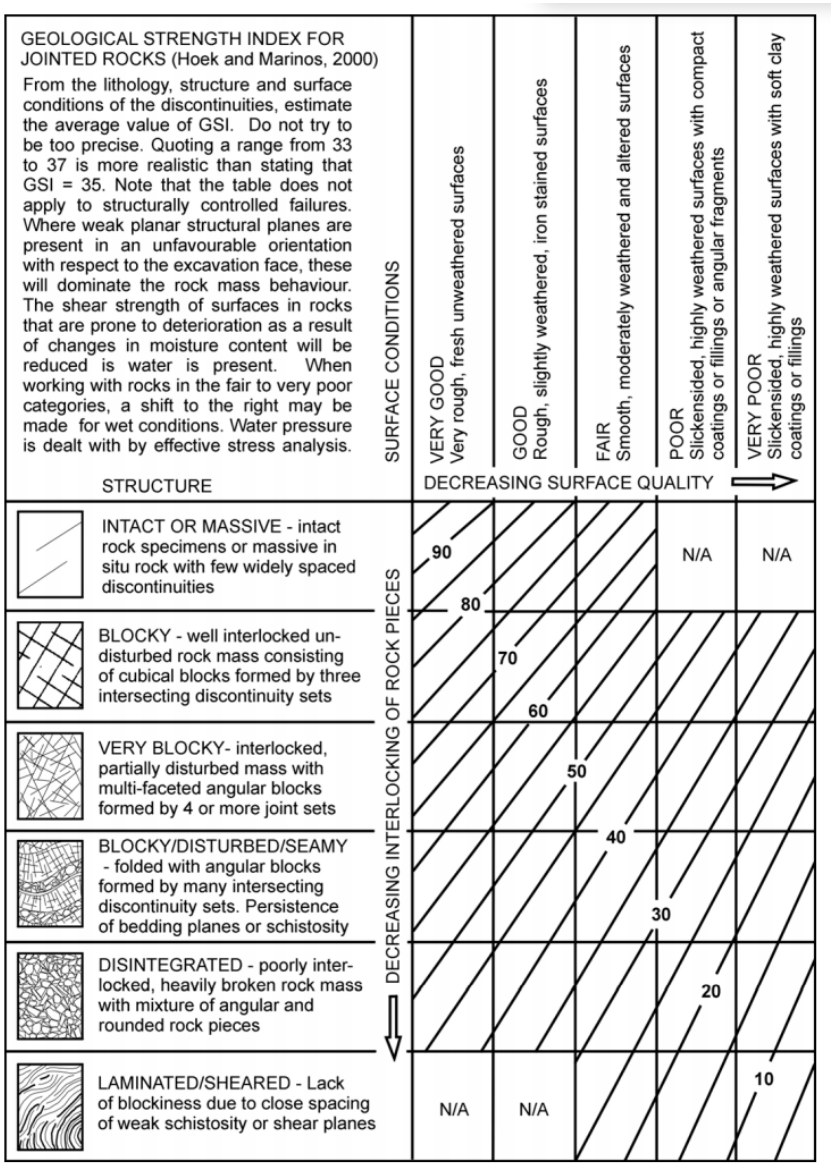

Figure 2.7 *Table for the determination of GSI for blocky rock masses on the basis of interlocking and joint conditions (Marinos and Hoek, 2000).*

2.3.4 Shear strength of filled discontinuities in rock

The now outlined conditions for shear strength apply for discontinuities in which rock wall contact applies for the entire length of the plane. In cases where contact is impaired by a soft filling material, shear strength can be reduced significantly. Its influence can be understood in terms of the geometrical interaction between fill material and joint walls, as well as the mechanical properties of the filling material itself (Barton, 1973).

Filling thickness and plane roughness are regarded as the most important factors in regards to geometrical interaction. For instance, in the case of planar surfaces such as bedding planes in sedimentary rock a thin clay coating will result in a significant shear strength reduction. In difference, a rough undulating joint with filling material thickness lower than the sum amplitude of the two rock planes, shear strength will be little different from that of unfilled rock strength (Barton, 1973). The idealized study of Goodman (1970) illustrates the negative relation between saw-tooth amplitude a and joint filling thickness f and peak shear strength (*figure 2.8*).

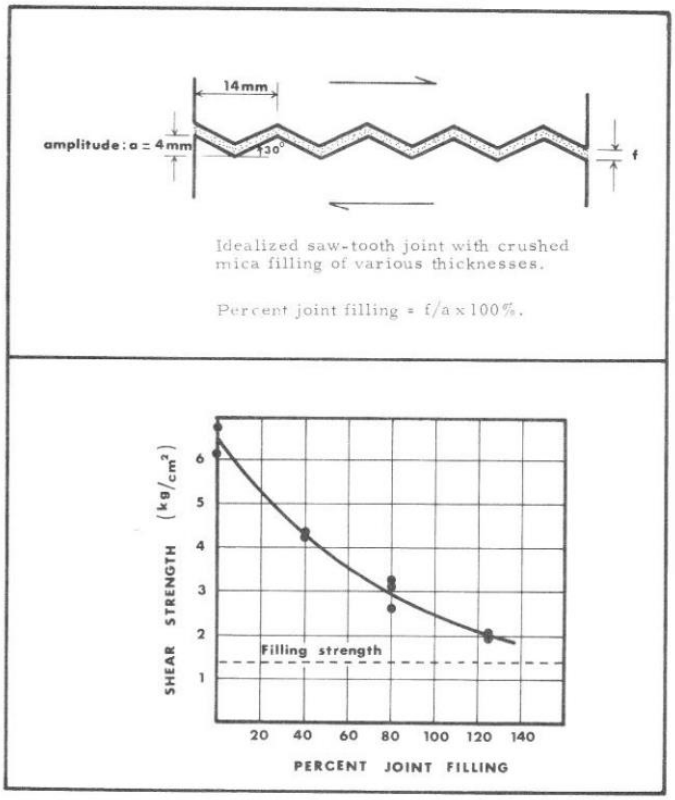

Figure 2.8 *Effects of filling material thickness and rock plane asperities on the shear strength of an idealized discontinuity according to Goodman (1970). Modified after Barton (1973).*

Another important distinction to make is whether the filling material (1) has suffered earlier shear displacement, or (2) if it has suffered no prior displacement (Barton, 1973). The first group is typified by faults, old slide surfaces in rock masses, shear zones, clay mylonites and bedding plane slips. Due to their prior shearing, the strength is therefore at, or close to residual strength. Bedding plane slip normally involve slip along discontinuities that already was clay bearing and merely represent weak horizons during folding or gravitational sliding during basin formation. In contrast, faults and prehistoric slide surfaces probably became filled with breccia and gouge during the slide process itself. The group of no previous displacement is typified in sedimentary rocks by altering beds or seams of clay and weak rocks such as shales, sandstone or limestones, or by various alterations in metamorphic and igneous rocks. For non-displaced conditions the distinction between normally- and over-consolidated states is important, as the difference in peak strength may be substantially large (Barton, 1973).

When it comes to the mechanical properties of the filling material, residual strength of natural soils is found to be strongly dependent on the relative amount of clay-minerals (Horn and Deere, 1962, Kenney, 1967). Soils containing large amounts of montmorillonite or mixed-layer minerals containing montmorillonite exhibited the smallest values of φ_r. In difference, the soils containing large quantities of massive non-clay minerals, small quantities of the montmorillonite minerals, and large quantities of clay minerals from the mica family exhibited the largest values of φ_r (*figure 2.9*). This evident mineralogic control is also partially reflected in part by the clay fraction of the given discontinuity. When the clay fraction is zero the friction angle corresponds to that of the massive minerals (Skempton, 1964). On the other hand, if the clay fraction is very high, the strength corresponds to that of the findings of Horn and Deere (1962) and

Kenney (1967). Figure *2.10* presents shear strength estimates for different filling materials of filled discontinuities in rock after Barton (1973)

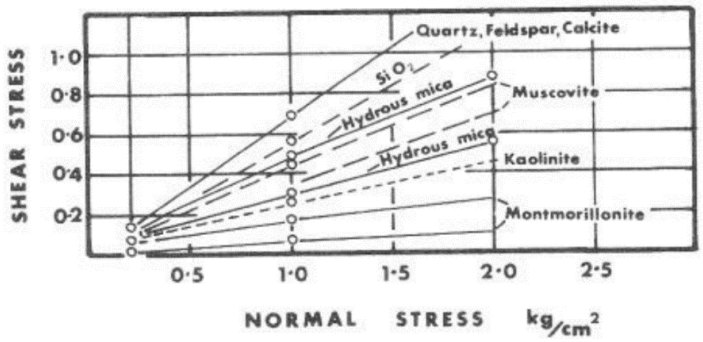

Figure 2.9 *Mineralogic control on the residual strength of clay, presented by Kenney (1967)*

Rock	Description	Peak c' (MPa)	Peak ϕ°	Residual c' (MPa)	Residual ϕ°
Basalt	Clayey basaltic breccia, wide variation from clay to basalt content	0.24	42		
Bentonite	Bentonite seam in chalk	0.015	7.5		
	Thin layers	0.09-0.12	12-17		
	Triaxial tests	0.06-0.1	9-13		
Bentonitic shale	Triaxial tests	0-0.27	8.5-29		
	Direct shear tests			0.03	8.5
Clays	Over-consolidated, slips, joints and minor shears	0-0.18	12-18.5	0-0.003	10.5-16
Clay shale	Triaxial tests	0.06	32		
	Stratification surfaces			0	19-25
Coal measure rocks	Clay mylonite seams, 10 to 25 mm	0.012	16	0	11-11.5
Dolomite	Altered shale bed, ± 150 mm thick	0.04	1(5)	0.02	17
Diorite, granodiorite and porphyry	Clay gouge (2% clay, PI = 17%)	0	26.5		
Granite	Clay filled faults	0-0.1	24-45		
	Sandy loam fault filling	0.05	40		
	Tectonic shear zone, schistose and broken granites, disintegrated rock and gouge	0.24	42		
Greywacke	1-2 mm clay in bedding planes			0	21
Limestone	6 mm clay layer			0	13
	10-20 mm clay fillings	0.1	13-14		
	<1 mm clay filling	0.05-0.2	17-21		
Limestone, marl and lignites	Interbedded lignite layers	0.08	38		
	Lignite/marl contact	0.1	10		
Limestone	Marlaceous joints, 20 mm thick	0	25	0	15-24
Lignite	Layer between lignite and clay	0.014-.03	15-17.5		
Montmorillonite Bentonite clay	80 mm seams of bentonite (mont-morillonite) clay in chalk	0.36 0.016-.02	14 7.5-11.5	0.08	11
Schists, quartzites and siliceous schists	100-15- mm thick clay filling	0.03-0.08	32		
	Stratification with thin clay	0.61-0.74	41		
	Stratification with thick clay	0.38	31		
Slates	Finely laminated and altered	0.05	33		
Quartz / kaolin / pyrolusite	Remoulded triaxial tests	0.042-.09	36-38		

Figure 2.10 *Shear strength of filled discontinuities and filling material after Barton (1973), modified from Hoek (2000)*

2.4 Stability assessment methods

In rock slope engineering, stability analysis techniques are applied to achieve safe and functional design for engineered slopes and to assess the equilibrium conditions of natural slopes. For landslide studies this is helpful in: (1) determining rock slope stability conditions, (2) investigating potential failure modes and (3) determining susceptibility to triggering mechanisms (Eberhardt, 2003). Approach and methodology vary based on local laws and norms (Myrvang, 2001), although most commonly one of the following principles are applied either alone or in combination: (1) empirical analysis, (2) limit equilibrium analysis, (3) numerical analysis or (4) physical modelling (Nilsen and Palmström, 2000). Choice of method should according to Stead et al. (2006) be a matter of the structural complexity of the respective rock slope instability (*figure 2.11*). For rock slopes of lesser complexity he suggests conducting a kinematic analysis for identifying the relevant failure mechanism, followed by a limit equilibrium (LEM) analysis.

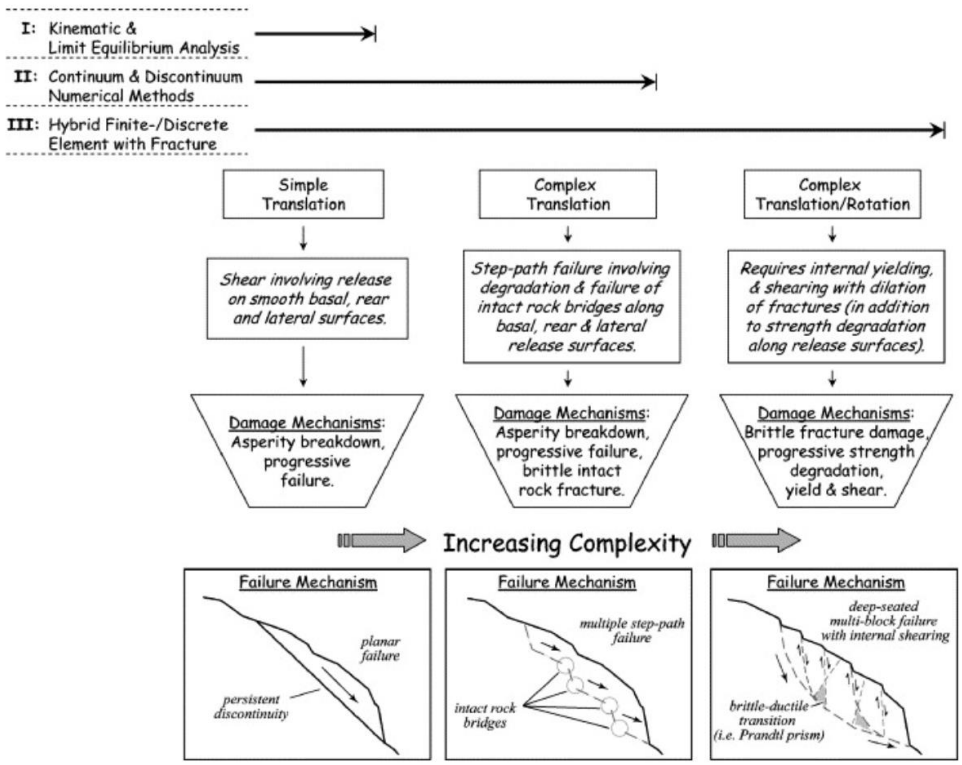

Figure 2.11 *Flowchart outlining three levels of landslide analysis and the modes of failure they are appropriate for (Stead et al., 2006).*

has traditionally been the dominating methodology for the quantification of rock slope stability, and consider the relation between resisting- and driving forces R_k and F_k within the rock mass to quantify factor of safety (FS) (*equation 2.12*). As indicated, FS=1 signifies resisting and driving forces in equilibrium. Stability is normally considered in terms of the parameters outlined in figure 2.12 (Nilsen et al., 2011).

$$FS = \frac{F_k}{R_k} \qquad 2.12$$

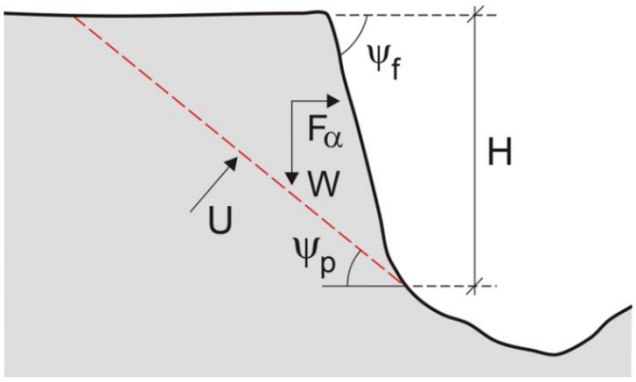

Figure 2.12 *Components contributing to driving and stabilizing forces. Variable H is slope height, ψ_f is slope angle, ψ_p is inclination of potential sliding plane, W is weight of potential slide material, U is water pressure, and F_α is seismic action.*

Whilst deterministic LEM quantify each input parameter in terms of a single value, probabilistic methodologies rely on each parameter being assigned a probability distribution, often according to a mean and standard deviation. Accordingly, a probability distribution for the factor of safety can be approximated. By summing the area of the curve falling within the FS<1 range, probability of failure can be determined (Nilsen et al., 2011).

To further investigate the influence of individual input-parameters, a sensitivity study can be conducted by defining a maximum credible range for individual critical parameters and holding all other parameters constant (Hoek, 2000, Wyllie, 2004). As discussed by Hoek (2000), even with very limited field data, practical and useful information can be obtained from a sensitivity analysis.

2.5 Geotechnical design in Norway

In Norway the legal basis for geotechnical design is set within the regulations on technical requirements for construction works (TEK10, continued in TEK17) as a part of the planning and building act (PBL). Projection should thus be in compliance with Norwegian Standard (Norsk Standard). This includes the Eurocode-series, and belonging national additions (Nilsen et al., 2011).

With the introduction of Eurocode 7 the traditional deterministic principle of calculating one FS was no longer permitted for geotechnical design. LEM should according to the guideline be conducted probabilistic, or according to the partial factor principle. Today the partial factor method is in most cases applied in practice for rock slope stability analysis of simple geometry, although there is a growing trend towards reliability based- and probabilistic design (Nilsen et al., 2011). These methodologies have their natural strength in accounting for the uncertainty and variability in input parameters. An additional advantage is that many countries, including Norway have guidelines and regulations on what magnitude of probability of landsliding is acceptable for localization of infrastructure (DSB, 2011). The guideline stated by the Norwegian Directorate for Public Safety (DSB) is outlined in *table 2.1*.

Table 2.1 *Norwegian requirements for acceptable localization of structures in potential slide susceptible areas (DSB, 2011).*

Landslide/Avalanche safety class	**Impact**	**Greatest nominal annual probability**
S1	Slight	1/100
S2	Moderate	1/1000
S3	Severe	1/5000

3 Methodology

3.1 Available data and software

Data accessed and applied in this thesis is presented in *table 3.1*. Additionally, a variety of software is involved in the making of this thesis, presented in *table 3.2*.

Only the southern part of the Hennøy peninsula is covered high a resolution DEM. For remote surveying of the remaining area of the peninsula, 10 m DEM and orthophoto was used.

Table 3.1 *Central background data used in the thesis.*

Dataset	Use	Source	Date of collection
1 m point cloud	Remote sensing	Available from Hoydedata.no	12.07.20
1 m DEM	Background map	Available from Hoydedata.no	12.07.20
10 m DEM	Background map	Available from Hoydedata.no	12.07.20
Orthophoto	Remote sensing, Background map	Available from Geonorge.no as WMS	24.04.21

Table 3.2 *Software apllied in the thesis.*

Software	Use	License provider
ArcGIS	Rendering maps and spatial analysis	NTNU
DIPS 7.0	Stereonet and kinematic analysis	NTNU
CloudCompare	Structural measurements on point clouds	Free Software
RocData	Rock properties	NTNU
Swedge	Probabilistic stability analysis	NTNU

3.2 Field work

The fieldwork was carried out over ten days in September 2020. A major part of the field work concerned structural mapping and description of rock slope failure deposits along the southern and western parts of the Hennøy peninsula. Structural mapping included oriented structural measurements of discontinuities, as well as landslide morphological descriptions including the mapping of open fractures and slide scars. In total 1060 oriented structural measurements were taken with a Freiberg type geological compass. Structural measurements were conducted around a total of 19 locations. Mapping of rock slope failure deposits focused on the characterization of the deposit and registration of block size. Locational data were registered with a handheld GPS (Garmin eTrex20).

The physical mapping was combined with remote sensing on point cloud models as supplement to the field mapping and to make observations on locations not accessible in the field. This includes structural measurements and delimitation of rock slope failure deposits. A rock sample was also collected for further rock mechanical testing to get an understanding of its mechanical properties and to define its failure criterion.

Supplementarily, estimations of JRC, JCS and residual friction angle φ_r was conducted on bedding planes to estimate a Barton-Bandis shear strength criterion.

3.3 Remote sensing

Remote sensing refers to the application of specific techniques to gather spatial data from a distance without physical interaction (Longley et al., 2015). These techniques can be categorized according to their inherent sensor systems. Passive sensors rely on natural sources of radiation, such as sunlight. Aerial photography falls into this category. In difference, active sensors techniques, such as laser scanning emit their own radiation source. Remote sensing hardware comes in terrestrial, aerial and satellite-based configurations (*figure 3.1*).

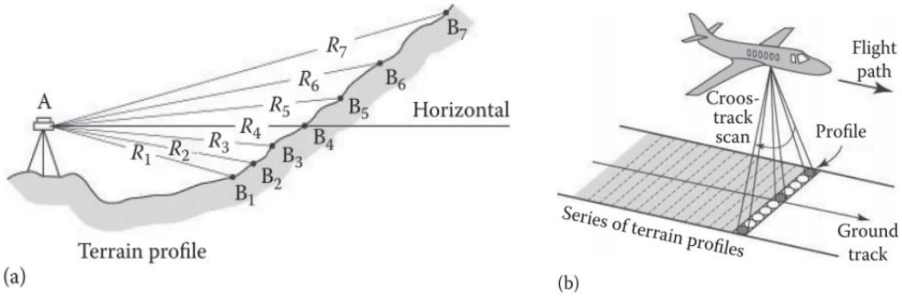

Figure 3.1 *Basic principles of (A) Terrestrial Laser Scanning (TLS) and (B) Aerial Laser Scanning (ALS). Modified after Shan and Toth (2018)*

3.3.1 Light Detection and Ranging (LiDAR)

LiDAR is among the most common active sensor remote sensing techniques in geological surveying. The scanner transmits laser pulses and registers the radiation that is scattered back to the receiver from the scanned object (Jaboyedoff et al., 2012). Knowing the direction and time of the laser pulse, a three-dimensional point representing the position of the reflecting object is calculated. By scanning the terrain in a grid pattern, topography can be recorded in detail. LiDAR systems usually come in terrestrial- (TLS) and aerial (ALS) configurations (*figure 3.1*). Whilst aerial scans have the advantage of covering large areas in a short time, terrestrial scans are often considered to be more accurate due to their fixed position (Oppikofer, 2009). The advantage of LiDAR is the potential of gathering larger amounts of high resolution three-dimensional spatial data in a short amount of time. Although, the initial data capture requires extensive post processing to filter out unwanted features and for error correction to provide a "true ground" point-data set (Shan and Toth, 2018).

Data can either be exported directly into point cloud computing software, as CloudCompare, or be rasterized to be incorporated into a geographic information system (GIS) based analysis. Both approaches are useful in context of the landslide field, as structural data can be mapped from rock slopes, and rasterized data can be applied as input for numerical run-out- and stability analysis. In this thesis ALS based point cloud data supplied by Høydedata.no was incorporated into remote structural mapping in CloudCompare. Rasterized ALS data was incorporated as input for GIS based spatial analysis in ArcGIS.

3.3.2 Structural measurements on point-cloud models

To supplement field data and cover areas not accessed in the field, structural measurements were conducted on ALS based point cloud models in CloudCompare. Structural measurements were primarily conducted by utilizing the compass plugin (Thiele et al., 2017). This method fits a plane to all points sitting within a predefined radius. By adapting the radius to a planar feature, the orientation of the discrete feature can be estimated. The method benefits from its and quick and easy data acquisition and easy to use nature.

It was decided to compare the Compass method to the more readily used Coltop3D method (Jaboyedoff et al., 2007). The Coltop3D software assign color to the topography according to its orientation, where terrain aspect attributes to the Hue (color) and slope angle to the Value (brightness). Orientation of the topography is extrapolated according to the four nearest neighboring points in a square, corresponding to a line passing through the middle of the cell linking the four grid points (*figure 3.2*). Measurements of the structures can be collected and exported to Excel. The methodology is described in detail by Jaboyedoff (2007).

The functionality of the Coltop3D software was adapted for use in CloudCompare, utilizing the qFacets plugin (Dewez et al., 2016). Color was adjusted according to the Hue and Value system based on the local terrain orientation, as described in the Coltop methodology (Jaboyedoff et al., 2007). The qFacets plugin allows for the automatic extraction of planar facets from point clouds based on a kd-tree. Each facet is classified according to its orientation and orthogonal distance. Facets can then be subdivided into families and filtered according to their orientation (Dewez et al., 2016). Resulting structural data can then be exported to Excel for implementation into further structural analysis.

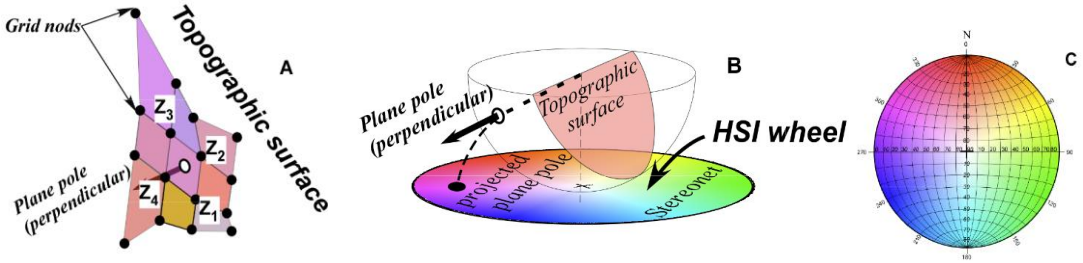

Figure 3.2 *(A) The topographic orientation is defined by the four nearest neighbors of a square grid, (B) Relation between plane orientation and color coding according to a colored stereonet according to the Intensity Hue Saturation System. (C) The Hue Saturation Intensity system projected over an equal area stereonet. Modified after Jaboyedoff (2007).*

Additionally, fractures were mapped on the south facing slope along the Svelgsegga ridgeline on point cloud models in CloudCompare. By inspecting the "inverse" side of the model, datapoints protruding the trend of the topography can be recognized. These datapoints are assumed to be a result of LiDAR rays penetrating open fractures. A limiting factor of the methodology is that only sub-vertical fractures with a substantial aperture are likely to be penetrated by the LiDAR scan.

3.4 Structural analysis

3.4.1 Stereographic Projection

Stereographic projection is a tool commonly used in visualizing three-dimensional structural data in two dimensions. Planar- and linear structures are projected in terms of dip and dip direction according to *figure 3.3*. Multiple different software packages offer this functionality, in addition to further structural analysis. The thesis utilize DIPS 7.0 for visual presentation of structural data and additional structural analysis, including kinematic analysis.

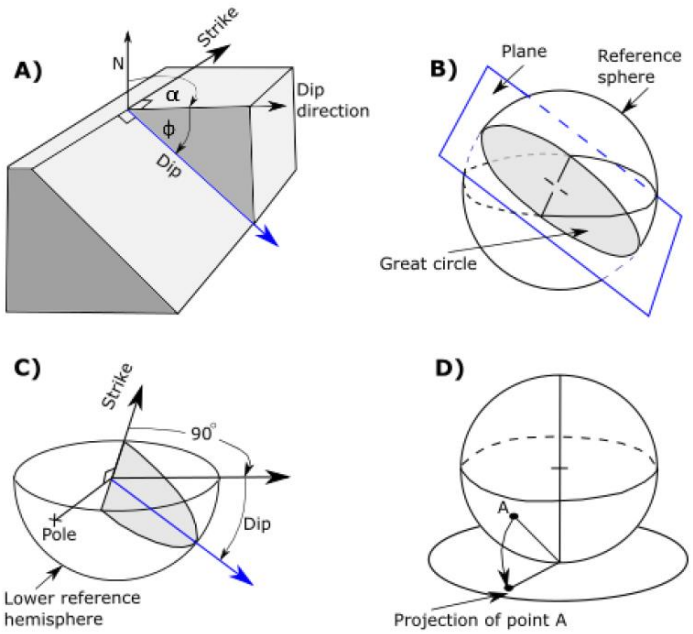

Figure 3.3 *Principle of stereographic projection, modified after Hoek and Bray (1981a) by Mo (2018). (A) Isometric illustration of a plane with indicated dip and dip direction. (B) Plane represented as a great circle in a reference sphere. (C) Pole projected onto the lower hemisphere, at a 90° angle normal to the plane. (D) Pole projected onto a 2D stereonet, indicating the dip and dip direction of the plane.*

3.4.2 Structural domains

When assessing the variability in rock slope stability within an area it is useful to assess the spatial variability in structures and slope orientation. By sub-dividing areas according to homogeneous geometrical relations of structures and topography, further structural analysis can be conducted to represent the given area (Böhme et al., 2013). To assess this spatial variability in structures, all main structure stops were plotted in stereonet and overlain the field map.

3.4.3 Kinematic feasibility test

Kinematic feasibility testing incorporates oriented structural data to assess the feasibility of rock slope failure (Richards et al., 1978, Hoek and Brown, 1980a, Hoek and Bray, 1981a, Wyllie, 2004, Hermanns et al., 2012). Specific criterions apply for different failure mechanisms dependent on the intersectional configuration of discontinuities, including joints, fractures, faults, and cleavage (Oppikofer, 2009). The commonly considered failure mechanisms are: (1) planar failure, (2) wedge failure and (3) toppling failure. Their geometric criterion are hereunder outlined (*figure 3.4*).

Planar sliding is facilitated by sliding on a singular planar feature. Hence, the structure is required to daylight downslope. In the stereonet projection this is indicated by a pole vector daylighting window dictated by the slope orientation. Sliding is further limited by the rock mass friction angle, signified in stereonet by a friction cone (Hermanns et al., 2012, Wyllie, 2004). A lateral tolerance in relation the slope aspect is usually applied. Normally, a window of ±20° is regarded as sufficient (Hoek and Bray, 1981a, Hermanns et al., 2012). However, when considering large rock volumes, this may be too strict when regarding the general complexity in structures and variance in slope aspect. As recommended by Hermanns et al. (2012) a more conservative approach should be applied in these cases, whereas points within a ±30° tolerance should be deemed as possible and values exceeding the threshold as partly possible. Considering the preset requirements, a critical zone not eliminated by any of the factors indicates the condition where sliding is deemed feasible.

In the case of wedge failure, collapse is facilitated by the interaction of two unique planar structures forming a line of intersection, indicated in the steronet as a linear feature (Markland, 1972, Hoek and Bray, 1981a, Hermanns et al., 2012). As failure is facilitated by sliding the same limitations are considered as for planar sliding, including daylighting window and friction cone. Generally, the same restrictions in lateral tolerance are applied as for planar sliding (Hermanns et al., 2012).

Toppling failure is in difference facilitated by the out-slope tilting of rock slabs. This requires the presence of discontinuities dipping into the face within a small angle with respect to the dip direction of the face. The dip of the discontinuities must be steep enough for interlayer slip to occur. "Direct" toppling usually only involve smaller rock volumes (Wyllie and Mah, 2004).

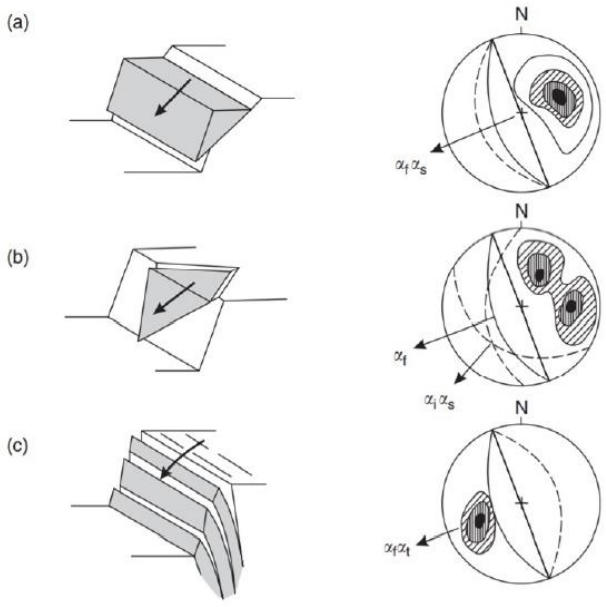

Figure 3.4 *(A) Planar failure, (B) Wedge failure, (C) toppling failure and related stereoplots (Wyllie and Mah, 2004)*

3.4.4 Structural profiles

When assessing rock slope stability, kinematic analysis may not be sufficient to describe many failure geometries due to the inherent simplicity of the test. This is true for complex failure mechanics, such as step-paths, multiplanar and buckling failure (Stead

and Coggan, 2012, Hermanns and Longva, 2012). Five cross-sectional structural profiles were therefore constructed to visualize the interaction of topography and structural composition. In the case of domains containing two characteristic slope aspects, a profile for each aspect is constructed. The topographical profile was extracted from the DEM in ArcMap and edited in Excel. Structures were drawn according to their apparent dip.

3.4.5 Morpho-structural domains

In morphologies dominated by layered rocks, defining the geometrical relationship between the orientation of bedding-planes and terrain is crucial for the understanding of types, patterns and abundance of landslides (Guzzetti et al., 1996). Studies of this relation have applied heuristic (Ruff and Czurda, 2008), statistical (Carrara et al., 1992, Thiery et al., 2007, Rossi et al., 2010), physical (Günther, 2003) or combined methods (Frattini et al., 2008, Santangelo et al., 2015).

Morpho-structural domains refers to the classification of a geographical area according to the homogeneous geometrical relationship between the orientation of bedding planes and the geometry of slopes (Cardinali et al., 2002). The classification of domains is determined according to a set of classification rules. It was chosen to apply the Topographic Bedding plane Intersection Angle (TOBIA) index approach (Meentemeyer and Moody, 2000), as described by Santangelo (2015). The TOBIA index T is a function of the topographic slope and the bedding dip direction and inclination (*equation 3.1*).

$$T = \cos(\beta) * \cos(\varphi) + \sin(\beta) * \sin\varphi * \cos(\alpha - \gamma)\ , (0 \leq T \leq 1) \qquad 3.1$$

Variable β is the bedding dip angle (0°-90°), α is the bedding dip direction (0°-360°), φ is the local terrain gradient (0°-90°) and γ is the local terrain aspect (0°-360°). In *equation 3* the term $\cos(\alpha - \gamma)$ quantify the cosine of the difference between local terrain aspect and bedding dip direction. This relation is used for the classification of domains according to the interaction of bedding dip direction and slope aspect in terms of: cataclinal-, anaclinal- and orthoclinal slopes (*figure 3.5*). The domains are determined according to a set of boundary conditions (*table 3.3*). Cataclinal slopes can be further sub-divided after cataclinal over-dip slopes, cataclinal under-dip slopes and cataclinal dip slopes (*table 3.4*).

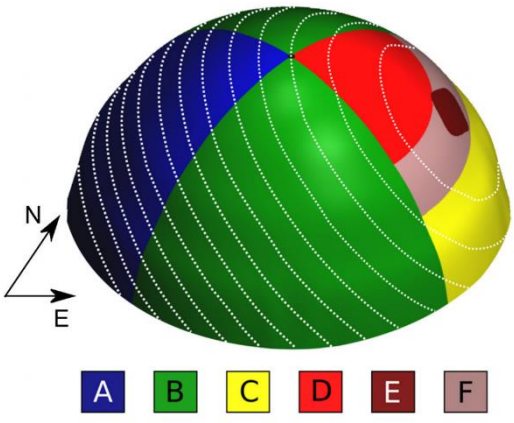

Figure 3.5 Possible plane-slope relations. The half sphere represents a synthetic topography and white dotted lines illustrates a homogeneous bedding with orientation N90E 45°. (A) anaclinal domain, (B) ortoclinal domain, (C) cataclinal over-dip domain, (D) Cataclinal under-dip domain, (E) Cataclinal dip domain (F) cataclinal dip domain (Santangelo et al., 2015).

Table 3.3 *Boundary conditions for morpho-structural domains (Meentemeyer and Moody, 2000).*

Domain	Boundary condition
Cataclinal	$0° \leq \lvert\alpha - \gamma\rvert \leq 45° \; i.e., \cos(\alpha - \gamma) > 0{,}707$
Anaclinal	$135° \leq \lvert\alpha - \gamma\rvert \leq 225° \; i.e., \cos(\alpha - \gamma) < -0{,}707$
Ortoclinal	$45° \leq \lvert\alpha - \gamma\rvert \leq 135°$ and $225° \leq \lvert\alpha - \gamma\rvert \leq 315°. \; i.e., -0{,}707 < \cos(\alpha - \gamma) < 0{,}707$

Table 3.4 *Boundary conditions for morpho-structural cataclinal domains after Meentemeyer and Moody (2000)*

Cataclinal domain	Boundary condition
Over-Dip	$T < 0{,}99$ and $\beta < \varphi$
Under-Dip	$T < 0{,}99$ and $\beta > \varphi$
Dip	$T \geq 0{,}99$

By defining a constant bedding orientation, the morpho-structural classification can be assigned according to the terrain gradient φ and local terrain aspect γ, following the boundary conditions of *table 3.5*. By assuming cataclinal dip conditions ($\cos(\alpha - \gamma) = 1$) we can determine the boundary conditions for cataclinal slopes with constant β and α value. The boundary conditions were applied to a 10m DEM in ArcGisPro using the *spatial analyst* toolkit.

Table 3.5 *Boundary conditions for morpho-structural cataclinal domains rewritten when assuming constant bedding dip angle* $\boldsymbol{\beta}$ *and bedding dip direction* $\boldsymbol{\alpha}$*.*

Cataclinal Domain	Boundary condition
Over-Dip	$\beta < \varphi + Cos^{-1}(0{,}99)$
Under-Dip	$\beta > \varphi + Cos^{-1}(0{,}99)$
Dip	$\beta - \varphi < Cos^{-1}(0{,}99)$

By overlapping the regional morpho-structural terrain zonation with a rock slope failure inventory map, the morpho-structural influence on failure distribution and abundance can be investigated statistically, as done by e.g. Santangelo et al. (2015), Pedrazzini et al. (2012).

3.5 Volume estimation

To investigate the spatial distribution and abundance of rock slope failures, volume estimation of slide scars and corresponding deposits were conducted. Methodologies for the two volume estimation methodologies that was applied is hereunder presented:

3.5.1 Sloping local base level (SLBL)

The "sloping local base level" (SLBL) technique is often applied in volume estimation of rock slope instabilities. The methodology is based on the concept of "base-level" as described by Jaboyedoff and Derron (2005) and refers to the lowest level a stream can erode. All slope volumes not buttressed at the bottom are liable to erosion and thus adhere to this principle. An elliptical failure surface with constant curve can be extrapolated to describe the basal surface of the instability (Travelletti et al., 2010). Volume can then be calculated according to the heigh difference between the failure surface and surface topography (Jaboyedoff and Derron, 2005). This methodology has

been modified by NGU for the use on slope failure deposits, as applied by Velardi et al. (2020) and is used accordingly in this thesis.

When calculating volumes with SLBL the main inputs are a DEM and a polygon delimiting the erodible feature. The curvature parameters are additionally important as they describe the tolerance of the curvature (*figure 3.6*). When considering the tolerance parameter for slope failure deposits one must consider the basal topography. No tolerance should be allowed in wide valleys, fjord bottoms and gentle dipping slopes, as the topology prior to the event is constructed as a straight line between each side of the deposit. For narrow steep-sided valleys tolerance should be considered to account for some curvature underlying the contact to the substrate. The calculation of failure surfaces and volume estimations were done using an SLBL-tool implemented to ArcGIS by NGU. According to the guideline a 10 m DEM should be used for volume estimation of slope failure deposits. Further adjustments of input parameters were adjusted according to the adapted guideline.

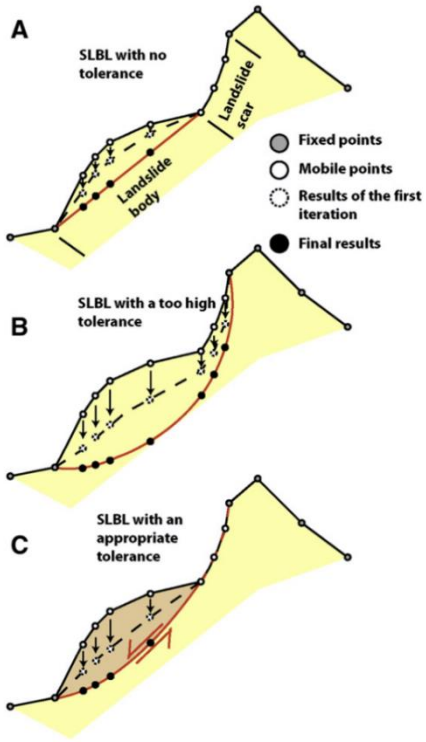

Figure 3.6 *Estimation of failure surface depth according to the SLBL concept. (A) Linear SLBL without tolerance. (B) Model with too high tolerance. (C) Model with appropriate tolerance. The geometry of the failure fits the scar bending (Travelletti et al., 2010).*

3.5.2 Two-and-a-half-dimensional volume estimation on point-cloud models

For the estimation volume of fracture delimited instabilities and pre-failure volume of relict rock slope failures a two-and-a half-dimensional methodology was applied on point cloud models in CloudCompare. The pre-failure geometries of mapped slide scars and basal surface of instabilities were extrapolated as singular planes in CloudCompare. By comparing the pre-failure geometry to the point cloud surface, the volumetric deficit can be calculated according to the height difference multiplied by the cell footprint of the two surfaces.

3.6 Local relief

Local relief refers to the relative elevation of two points. In topographic studies local relief is helpful for visualizing the height of a slope in relation to the slope base. Local relief can be calculated by subtracting the minimum elevation from the maximum elevation within a square around each pixel of a DEM (Pedrazzini et al., 2016). The analysis was conducted in ArcMap on a 10m DEM according to the methodology outlined by Novák (2014). Previous studies of regional topographic controls on rock slope failures and rock slope instabilities suggests the application of a 5 km circular radius (Agliardi et al., 2009, Pedrazzini et al., 2016). A common denominator for these studies is their large survey area in comparison to the study area of this thesis. To accommodate the reduction in magnitude, the box dimension was reduced to 2,5 km.

3.7 Rock properties and classification

3.7.1 Laboratory tests

Rock mechanical testing was carried out at NTNUs lab facilities. The failure criterion of the rock mass was to be determined for input into probabilistic stability analysis and further understanding of the rock strength and ductile behavior. Investigations include Triaxial Compression Test, Uniaxial Compressive Test and Brazil test. Testing was carried out on drilled cores from a single rock block. Due to a limited core sample size all tests under fully saturated water conditions to simulate "worst case" conditions. Core dimensions are listed in *table 3.6*.

Table 3.6 *Cores tested in the rock mechanical laboratory. Overlined samples were not tested.*

Sample	Test	Diameter [mm]	Length [mm]	Weight [kg]	Comment
1.1	UCS	34,22	90,13	222,93	No visible weakness
1.2	UCS	34,23	90,13	223,38	No visible weakness
1.3	Triaxial	34,22	89,70	221,73	No visible weakness
1.4	Triaxial	34,23	89,70	221,81	No visible weakness
1.5	Triaxial	34,22	89,67	221,56	No visible weakness
1.6	Triaxial	34,21	89,67	221,73	No visible weakness
1.7	Triaxial	34,22	90,13	222,96	No visible weakness
1.8	Triaxial	34,21	86,27	213,42	No visible weakness
1.9	Triaxial	34,22	89,70	221,67	No visible weakness
1.10	Triaxial	34,22	89,67	222,39	Small visible joint
~~1.11~~	-	34,22	90,13	223,77	Small visible joint
~~1.12~~	-	34,22	89,69	221,62	Small visible joint
~~1.13~~	-	34,22	86,27	213,27	Visible joint
~~1.14~~	-	34,22	89,66	218,6	Weathered on surface
2.1	Brazil	50,78	24,93	-	No visible weakness
2.2	Brazil	50,81	25,04	-	No visible weakness
2.3	Brazil	50,86	24,70	-	No visible weakness
2.4	Brazil	50,85	24,95	-	No visible weakness
2.5	Brazil	50,80	25,02	-	Small visible joint
2.6	Brazil	50,84	24,93	-	Small visible joint
2.7	Brazil	50,53	24,92	-	Small visible joint
2.8	Brazil	50,80	23,72	-	Small visible joint
2.9	Brazil	50,80	24,47	-	Small visible joint
2.10	Brazil	50,84	24,67	-	Small visible joint
2.11	Brazil	50,76	24,20	-	Weathered joint

3.7.2 Uniaxial compression test

Uniaxial compression testing is carried out by loading the core axially without confining pressure ($\sigma_2 = \sigma_3 = 0$). Uniaxial compressive strength (UCS) is defined according to the maximum stress applied prior to failure. In general, five tests are regarded as ideal for the determination of σ_c according to Brown (1981). Due to the limitation in core samples, only two tests were carried out in the uniaxial configuration. The machine utilized for both the uniaxial and triaxial compression testing is a GCTS RTR – 4000 type, with a loading capacity of 4000 tons.

Both uniaxial and triaxial compression testing requires cylindrical samples, normally with a diameter of approximately 54 mm and a length 2,5-3 times the diameter D. Due to the limited size and surface area of the rock block, it was decided to prepare cores with 31 mm diameter to maximize the sample size. All cores were prepared following a consistent workflow. Samples were cored with a core driller and then cut to its predetermined length of $2{,}7\ x\ D$. The surface of the rock block contained a thin weathered layer and was therefore cut off. To ensure full water saturation, the rock cores were put in water minimum 24 hours prior to testing. Cores were put in a plastic membrane to contain the sample in case of explosive failure. During testing the core is fitted with radial and axial extensometers to monitor rock strain (*figure 3.7*). After testing the fracture angle of both uniaxial and triaxial samples were measured with a protractor.

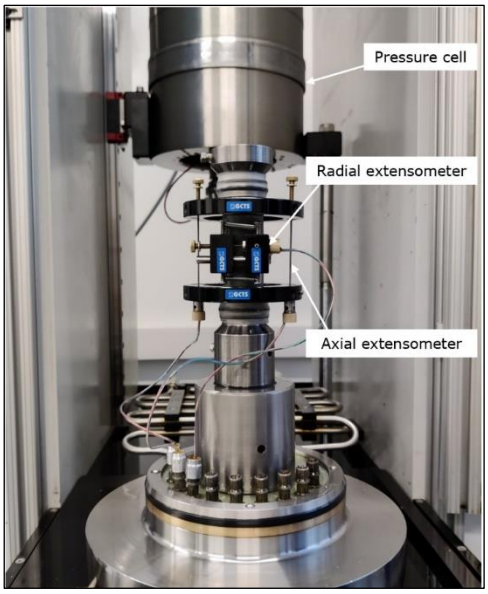

Figure 3.7 *Setup for uniaxial and uniaxial compression testing. Tests were applied a plastic film to contain the sample and isolate from hydraulic fluid. Radial and axial extensometers were fitted to monitor sample deformation. A submergible pressure cell was fitted around the sample and pressurized with hydraulic fluid during triaxial testing.*

As discussed by Hoek (2000), the influence of sample size may influence the peak strength. The relationship is outlined by Hoek and Brown (1980a), suggesting that the UCS of a rock specimen with diameter d is related to the UCS of a 50 mm diameter sample according to *equation 3.1*.

$$\sigma_{cd} = \sigma_{c50}\left(\frac{50}{d}\right)^{0,18} \qquad 3.1$$

It is suggested that the reduction in strength with diameter is related to the greater opportunity of failure in and around grains, as more grains are included within the sample. With a sufficiently large sample the strength should then reach a constant value. Although, this relationship is as pointed out by Mo (2018) somewhat contested. Studies in sedimentary rock imply that it for smaller diameters samples (sub 54 mm) that the relation may in fact be a reversed (Masoumi et al., 2012). It was therefore not conducted any efforts to adjust the UCS to account for scale effects.

Strain over stress data allows for the determination of Young's modulus (E) and Poisson's ratio (v), and are normally considered according to $\sigma_{c(50\%)}$ (*equation 3.2, 3.3, figure 3.8*). Prior to failure the rock was loaded at a constant rate of 0,8MPa/s. Depending on the post failure behavior this was modified according to a desired strain rate, referred to as strain control. This is to ensure the ideal capture of post failure behavior of the rock.

$$E = \frac{\Delta\sigma_{a,50\%}}{\Delta\varepsilon_{a,50\%}} \qquad 3.2$$

$$v = \frac{\Delta\varepsilon_{r,50\%}}{\Delta\varepsilon_{a,50\%}} \qquad 3.3$$

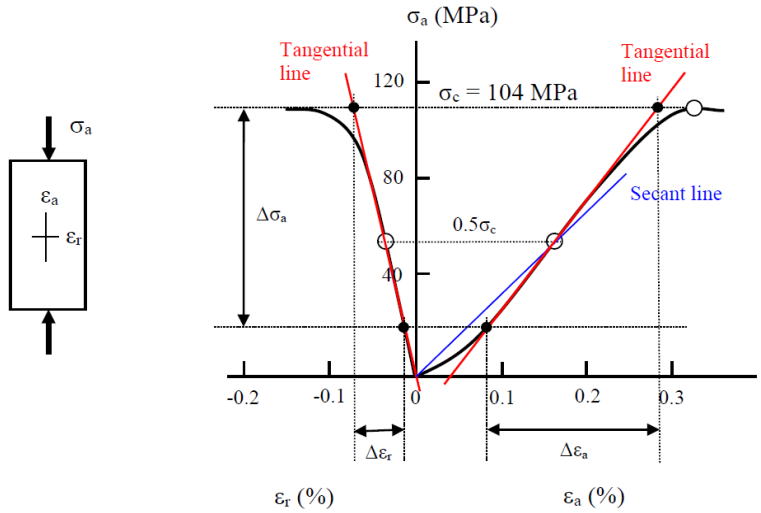

Figure 3.8 *Stress-strain curve of a rock specimen in uniaxial compression testing. Tangent lines are drawn according to $\sigma_{c(50\%)}$ for the determination of Young's modulus and Poisson's ratio (Li 2018).*

3.7.3 Triaxial compression test

Triaxial compression testing is carried out by loading the sample axially under a constant confining pressure ($\sigma_1 > \sigma_2 = \sigma_3$). The sample is confined within a loading cell and filled with hydraulic fluid that is applied pressure to induce confining pressure. Testing was carried out following the same core preparation procedure and test configuration for the UCS testing. Number of tests should be large enough to decisively determine a fracture curve over the different confinement pressures. This is depending on the test methodology, variation within the rock type and the application of the data (Hoek, 2000).

According to Hoek (2000) at least five well-spaced data points should be included in a triaxial analysis. In total 8 cores were tested triaxially. Uniaxial testing revealed a stable ductile zone prior to failure. It was therefore decided to run each test in multiple steps to maximize that data output. This method involves increasing the confining pressure rapidly when the sample has reached its peak compressive strength, indicated by a

distinct increase in radial strain. Confinement pressures applied for each test were based on the dimensions applied by Tønset (2019) (*table 3.7*).

Table 3.7 *Sigma3 values for cores tested in uniaxial and triaxial testing.*

	Sigma3 [MPa]					
Sample #	**0**	**2,5**	**5**	**10**	**15**	**20**
1	x					
2	x					
3			x	x		
4		x	x	x		
5		x	x	x		
6				x		x
7		x	x	x		
8		x	x	x		
9						x
10			x	x	x	

3.7.4 Brazilian test

Brazilian test is an indirect method of estimating the tensile strength of a rock sample. Stress analysis indicates that the stress perpendicular to the diametrical line connecting two loading points on a disc is tensile (*figure 3.8 A*). Thus, the tensile strength of the sample can be determined by recording the maximal load prior to failure (Li, 2018). A standard Brazilian test is conducted by applying load on two steel jaws, interlocking the sample. A hydraulic jacking rig with used to apply load and the maximum load value was recorded by a digital logger (*figure 3.8 B*). Tensile strength is thereby determined according to *equation 3.3*.

$$\sigma_t = \frac{2}{\pi}\frac{P}{Dt} \tag{3.4}$$

Parameter p is load at failure, D is the specimen diameter and t is the thickness of the specimen. It is according to Li (2018) recommended that the disc specimen has a diameter D of 50 mm and that the thickness be half the diameter ($t = 0{,}5D$).

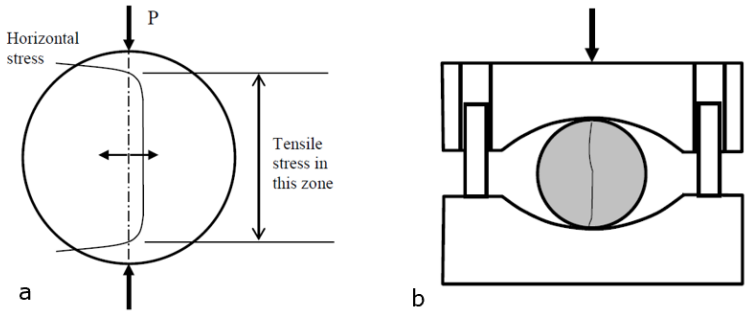

Figure 3.8 *(A) The distribution of stress along the loading diameter in a disk under point loading. (B) Brazilian test setup (Li, 2018).*

3.7.5 JRC, JCS and φ_r

The Barton-Bandis shear strength criterion rely on parameters: JRC, JCS and φ_r (*equation 2.6*) for determination of shear strength. For this thesis it was chosen to approximate values from simple field measurements. The chosen methodology is hereunder described:

Barton and Choubey suggests that φ_r can be determined according to *equation 3.5*.

$$\varphi_r = \varphi_b - 20 + \left(20\frac{r}{R}\right) \qquad 3.5$$

Parameter r is the Schmidt rebound number on wet and weathered fracture surfaces and R is the Schmidt rebound on dry unweathered and sawn surfaces. In field Schmidt-hammer tests were conducted 8 locations. For each location, 10 measurements were taken on both non-weathered and weathered surfaces.

JRC was determined according to the relation outlined by Barton and Bandis (1982) (figure 3.9). The JRC value can thus be determined according to the maximum amplitude of asperities along profile lengths parallel and normal to the strike of theplane. This was easily determined in the field with a ruler. Test were conducted on 9 location with three measurements taken in each profile direction.

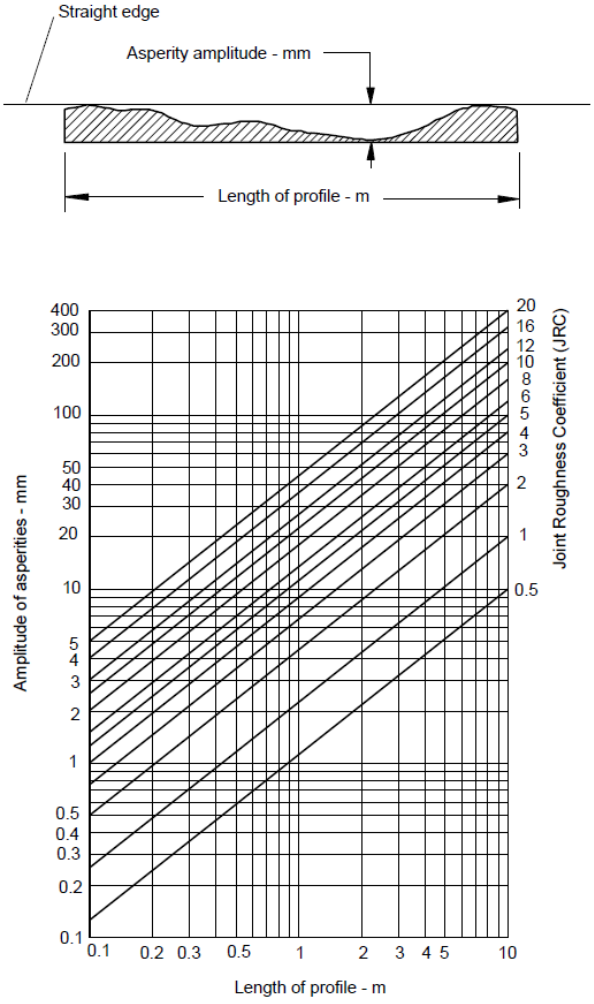

Figure 3.9 Method for estimating JRC from measurements of surface roughness amplitude from in reference to a straight edge (Barton and Bandis, 1982).

The estimation of JCS involves Schmidt rebound testing of the failure surface. Rebound values can then be correlated to a UCS value, according to the relationship proposed by Deere and Miller (1966) (*figure 3.10*). In the field testing was conducted on 9 different locations, consisting of 10 measurements per location.

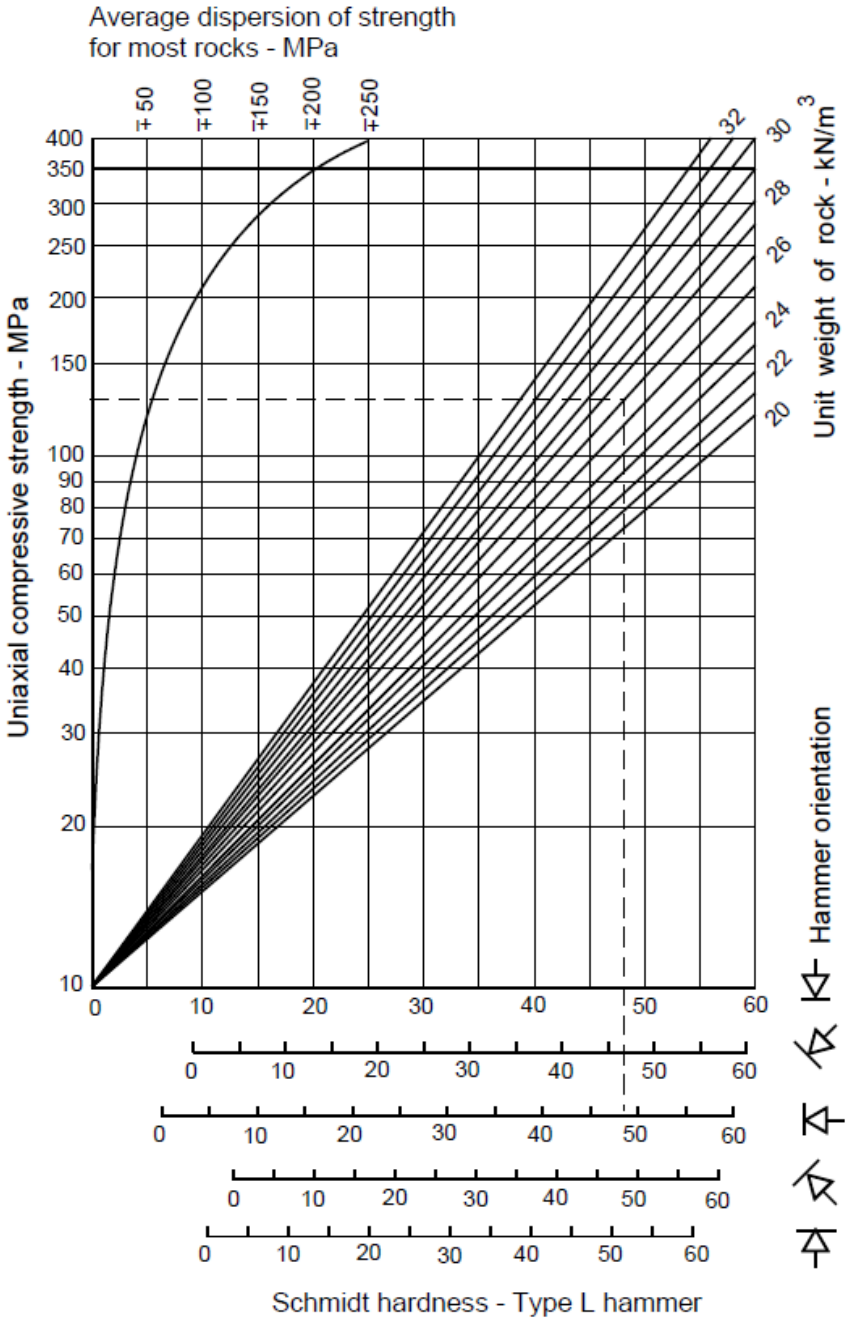

Figure 3.10 *Estimate of JCS from Schmidt hardness (Deere and Miller, 1966)*

3.8 Quantification of input parameters for probabilistic stability analysis

A probabilistic stability analysis was conducted in Swedge. Methodology for quantification of input parameters is hereunder presented:

3.8.1 Geometry

The Swedge software define the wedge geometry as a tetrahedron shape, according to slope geometry and the orientation of two discontinuity planes. These inputs dictate the volume of the wedge, as well as the area of delimiting discontinuities.

3.8.2 Shear strength

In Swedge joint strength is quantified either in terms of the Mohr-Coulomb-, or Barton-Bandis failure criterion. To accounting for the apparent non-linear relation between shear strength and normal stress, failure criterions like the Hoek-Brown criterion has to be adapted to fit the software chriterion. This conversion is simply done by assigning a mean normal stress value that is representative of in-situ basal plane conditions. Values for instantaneous cohesion c_i and friction angle φ_i can then be defined as a tangent on the Hoek-Brown curve (*figure 3.11*), intersecting the in-situ normal stress value. The conversion was done by using the *instantaneous Mohr-Colomb tool* in RocData. The software determines the mean normal stress σ_n as a linear function of the unit weight of the rock mass γ and the overburden z to the basal surface (*equation 3.8*).

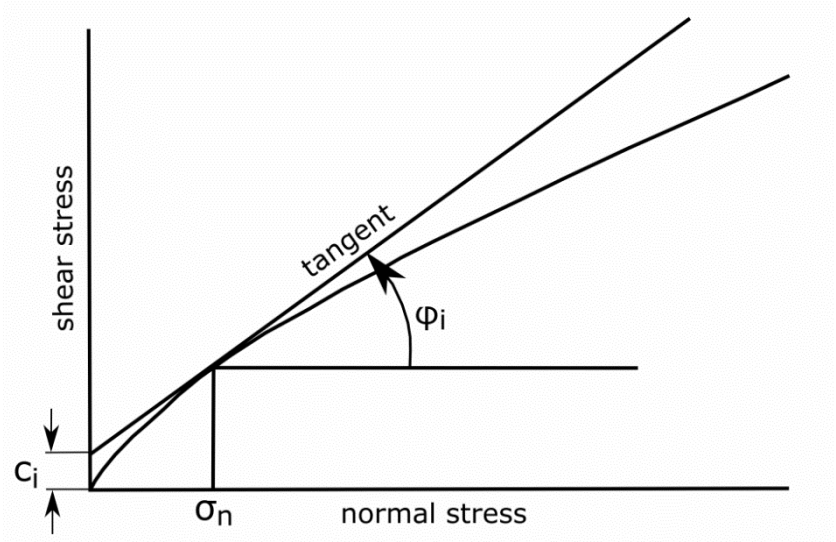

Figure 3.11 *Basic principle for the determination of instantaneous cohesion C_i and friction angle φ_i from a non-linear failure criterion (Hoek, 2000).*

$$\sigma_n = \gamma * z \tag{3.8}$$

Variance in rock mass strength was quantified according to the coefficient of variation (COV) (*equation 3.9*) displayed in the uniaxial and triaxial lab data.

$$COV = \frac{S_r}{m_r} \tag{3.9}$$

Parameter S_r is the standard deviation of the mean m_r. A small uncertainty would according to Hoek (2000) be representative by COV=0,05, whilst considerable uncertainty is present when the coefficient exceed COV=0,25. The coefficient should be assigned a lognormal distribution to ensure that all randomly generated values of shear strength will always be positive (Rocscience, 2021).

3.8.3 Water pressure

As pointed out by Nilsen (2017), reliable quantification of maximum ground water pressure is always difficult. Most commonly used in stability assessment when regarding "worst-case" conditions is the Hoek and Bray (1981b) model (*equation 3.8*). The model assumes that water enter the failure plane at the top of the slope and thereby builds up hydrostatically to a maximum value at the middle of the plane and then drains freely at the bottom (*figure 3.12 A*). This configuration is not regarded very reflective of reality as water normally drain out along cracks and fissures down-slope, considerably reducing the resultant water pressure (*figure 3.12 B*). To evaluate and quantify the worst-case water pressure is however difficult and it is according to Nilsen (2017) wise to consider the more conservative configuration for worst-case conditions.

$$U = \frac{\gamma_w H^2}{4 sin \psi_p} \qquad 3.8$$

Parameter H is slope height, γ_w is the specific gravity of water and ψ_p is the inclination of the potential sliding plane.

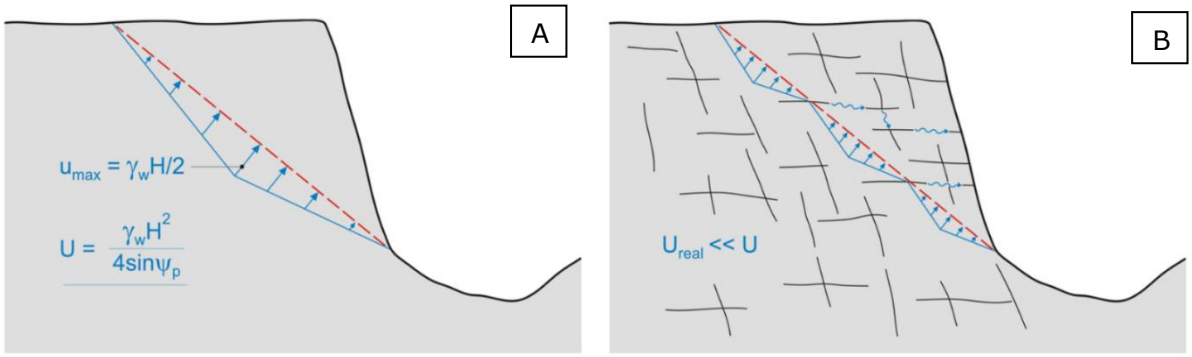

Figure 3.12 (*A) Commonly applied "worst case" conditions for sliding surface water pressure, compared with (B) the more realistic worst case scenario, resulting in* $U_{real} << U$

In Swedge water pressure is quantified in terms of percentage of the failure plane height filled with water. It is assumed that water will accumulate on the sliding surface as a result of direct surface runoff during heavy precipitation events or excessive melt-water from heavy snowmelt during spring. The probability of occurrence for these events can be defined according to a truncated exponential distribution, as the maximum value will occur very rarely. Mean water depth is assumed to be one third the slope height (Hoek, 2000, Nilsen, 2000).

3.8.4 Seismicity

In compliance with Eurocode 8 it is required to account for seismicity in slope stability analysis (Standard-Norge, 2014a). In Norway, reference values for ground acceleration a_{gr} is calculated according to equation 3.9. Parameter a_{g40HZ} is the peak value for seismic acceleration with return period 475 years (*figure 3.12*). Typical values for mainland Norway vary from 0,25 – 1,05 m/s^2 (Standard-Norge, 2014b).

$$a_{gr} = 0{,}8 * a_{g40HZ} \quad 3.9$$

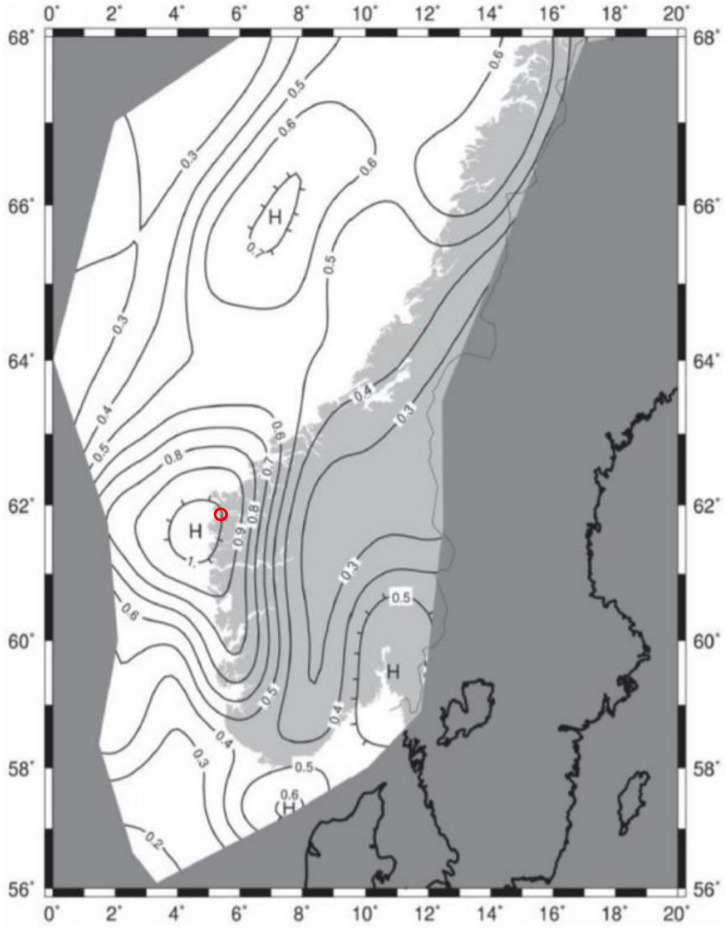

Figure 3.12 *Seismic zones for peak value for ground acceleration a_{g40HZ} (m/s^2) for southern Norway. Location of the study area is indicated (red circle). Modified from Standard-Norge (2014b).*

After the implementation of Eurocode 8, both the component of horizontal- F_H and vertical load F_V should be accounted for (*equation 3.10 and 3.11*). Parameter a is the seismic acceleration and S is an amplification factor. Definition and quantification of theese parameters is further described by Kainya et al. (2017) and Standard-Norge (2014a).

$$F_H = 0{,}5 * a * S * W \quad 3.10$$

$$F_V = \pm 0{,}33 * F_H \quad 3.11$$

As Swedge does not implement probability distributions for external load vectors, the old method of equivalent horizontal seismic load according to Eurocode 7 is here applied. Seismic coefficient a_k and horizontal seismic load F_{ak} was thus calculated according to equation 3*.12 and 3.13* (Nilsen et al., 2011).

$$a_k = \frac{a_{g40HZ}}{g} \quad 3.12$$

$$F_{ak} = W * a_k \quad 3.13$$

The frequency in occurrence for earthquakes of different magnitudes can be represented as an exponential distribution, suggesting that large earthquakes are very rare. Mean

value was defined as $a_{k,max}/3$ and the maximum seismic coefficient ($a_{k,max}$) in terms of a_k, in accordance with Nilsen (2000)

4 Results

4.1 Lithology

The bedrock within the interior of the Hornelen basin is reported to consist of mainly slightly metamorphosed sandstone (Bryhni, 1978). This is true for the field area, where grain size vary from fine to medium sand. Variation within the sandstone occur in cm- to m scale lithofacies, occurring in sometimes repeating and sometimes seemingly random sequences. Distribution and relative abundance of lithofacies seem to vary within the field area. From field mapping, five lithofacies are recognized: (1) siltstone/shale pellet conglomerate, (2) massive sandstone, (3) parallelly laminated sandstone, (4) cross-laminated sandstone, (5) cross bedded sandstone (*figure 4.1*).

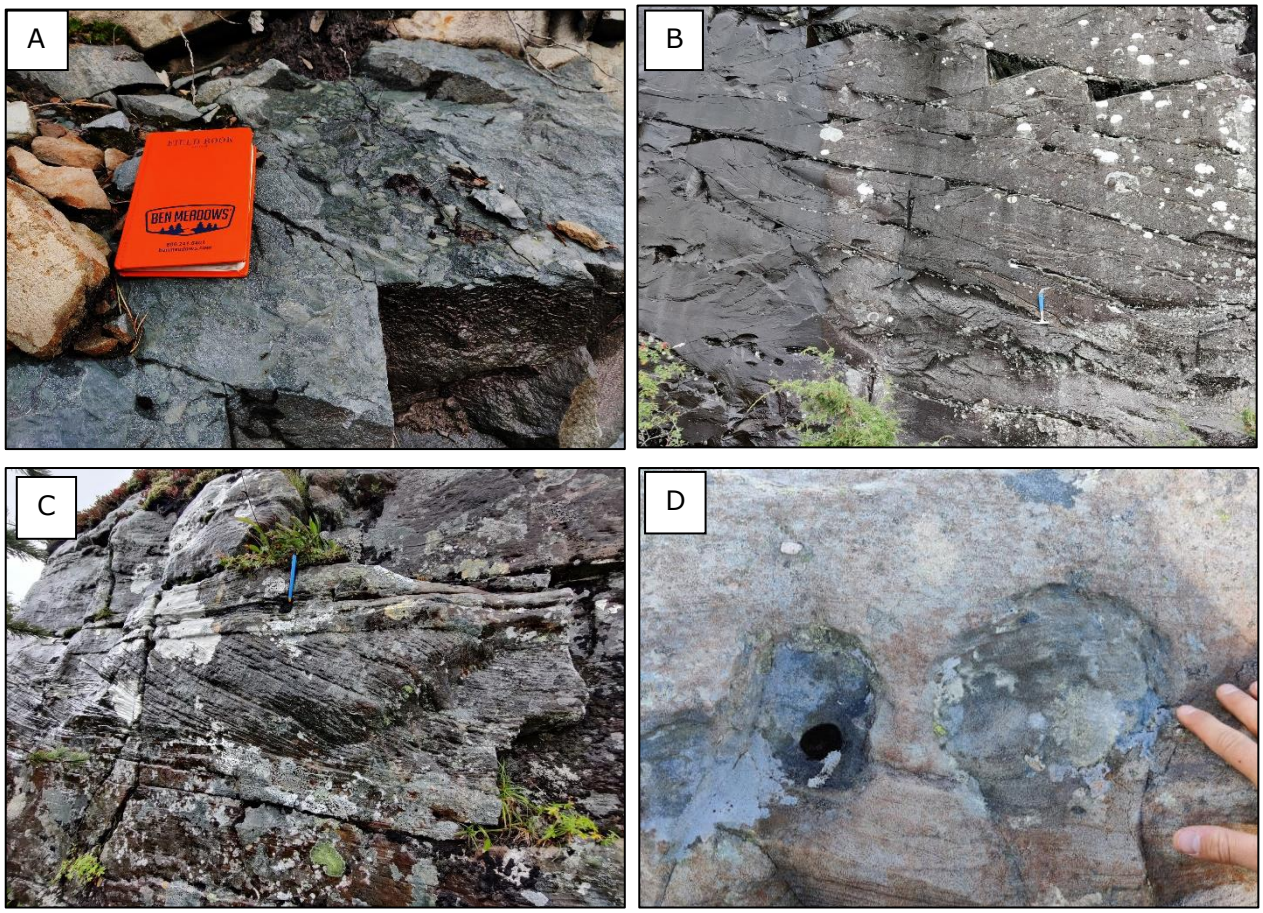

Figure 4.1 *Lithofacies observed in the field. (A) Siltstone/shale pellet conglomerate, (B) cross bedded sandstone, (C) parallelly laminated sandstone and cross-laminated sandstone, (D) Massive sandstone with calcareous concretion.*

Petrographic analysis by Hardie (2017) conducted for Bremanger Quarry AS presents the mineralogic composition of the rock. As indicated in *figure 4.2*, quartz is the dominant mineral, forming 43,7% of the total constituent. The proportion of quartz in relation to feldspar and lithic fragments classifies the sandstone as arkose (McBride, 1963). Mica is present only in minor amounts (3,0%) and is aligned parallel to the sedimentary bedding. Minor chlorite (4,0%) fills pore spaces and the rock is generally without voids, therefore appearing particularly dense and robust. The presence of epidote and chlorite indicates diagenetic modification of the rock, possibly correlating with low grade metamorphism (Hardie, 2017).

A

Components	**Lump Sample**	**Q/F/L** (quartz/feldspar/lithic Proportion)
Detrital Components		
Quartz	43.7%	63%
Feldspar	20.0%	29%
Lithic fragments	5.7%	8%
Mica	3.0%	
Heavy Minerals	3.3%	
Authigenic Minerals		
Quartz Overgrowths	1.0%	
Calcite	14.0%	
Chlorite	4.0%	
Clay minerals	5.0%	
Opaque Minerals	0.3%	
Total	**100%**	**100%**
Visual Porosity	Trace	

B

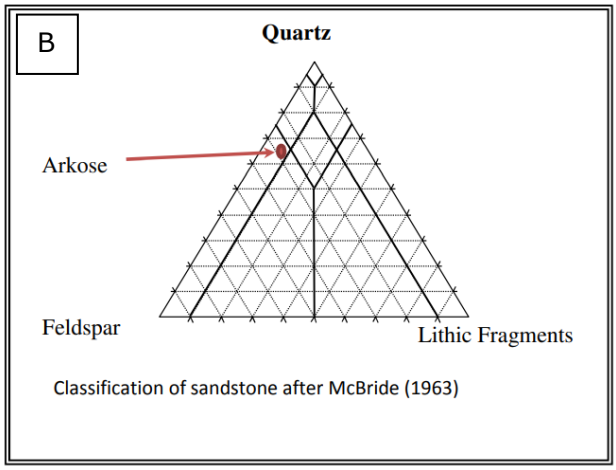

Figure 4.2 (*A) Petrographic analysis of rock sample from Bremanger Quarry AS, (B) Classification of the sample according to McBride (1963). Modified from Hardie (2017)*

4.2 Geomorphological conditions

A geomorphological overview of the southeastern aspect of the Svelgsegga ridgeline and surrounding slopes is given in *figure 4.3*. Fractures mapped on point cloud models in CloudCompare are indicated as green dots.

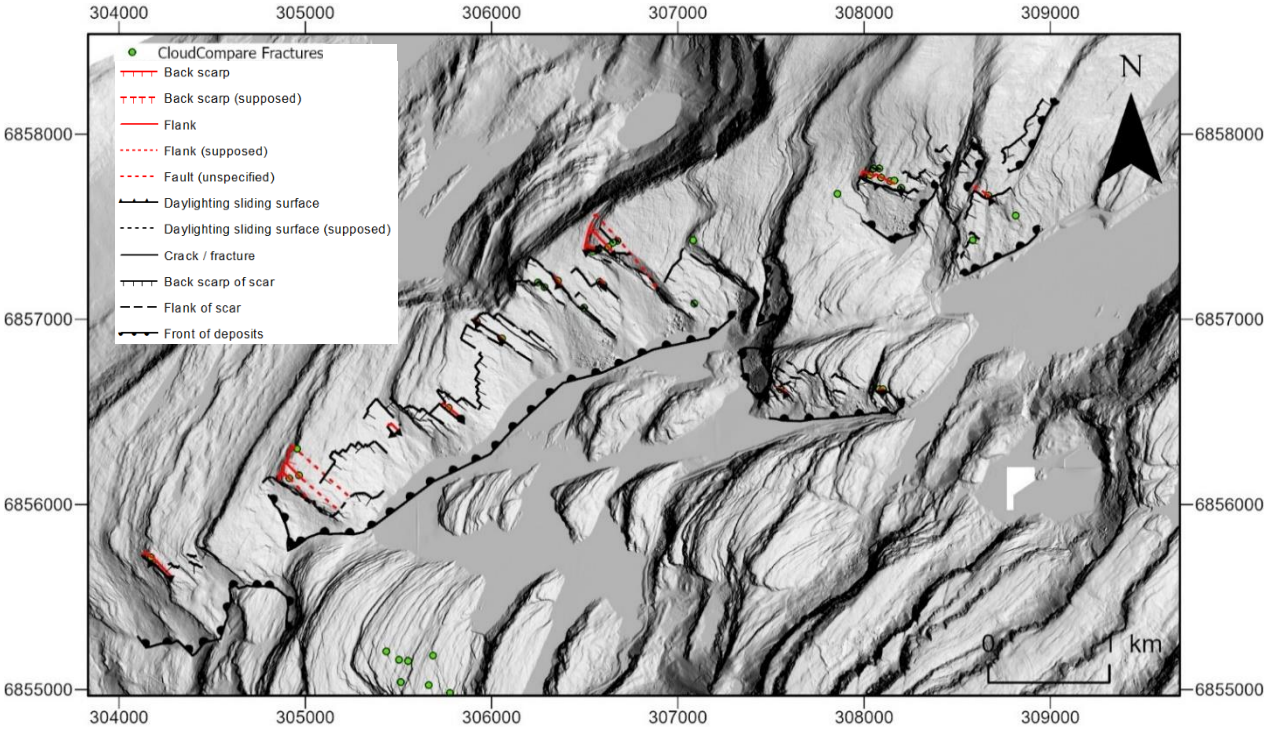

Figure 4.3 *Overview of the morphological conditions around lake Svelgsvatnet. Inventory is derived from both field observations and by remote sensing.*

4.3 Rock slope failure deposits

Rock slope failure deposits were mapped and characterized according to magnitude of failure. Magnitudes were delimited according to categories: rockfall (L_{RF}, <10.000 m^3), rock slope collapse (L_{SC}, 10.000-100.000 m^3) and rock avalanche (L_{RA}, >100.000 m^3). Statistics are presented in *table 4.1 and* distribution in *figure 4.4*. Landslide density is given according to the total study area.

Table 4.1 *Descriptive statistics for rock slope failures on the Hennøy peninsula.*

Failure magnitude	Number [#]	Total covered area [m^2]	Density [#/km^2]
Rockfalls	-	4.751.144	-
Rock slope collapse	*19*	387.955	0,3
Rock avalanche	*11*	473.658	0,2

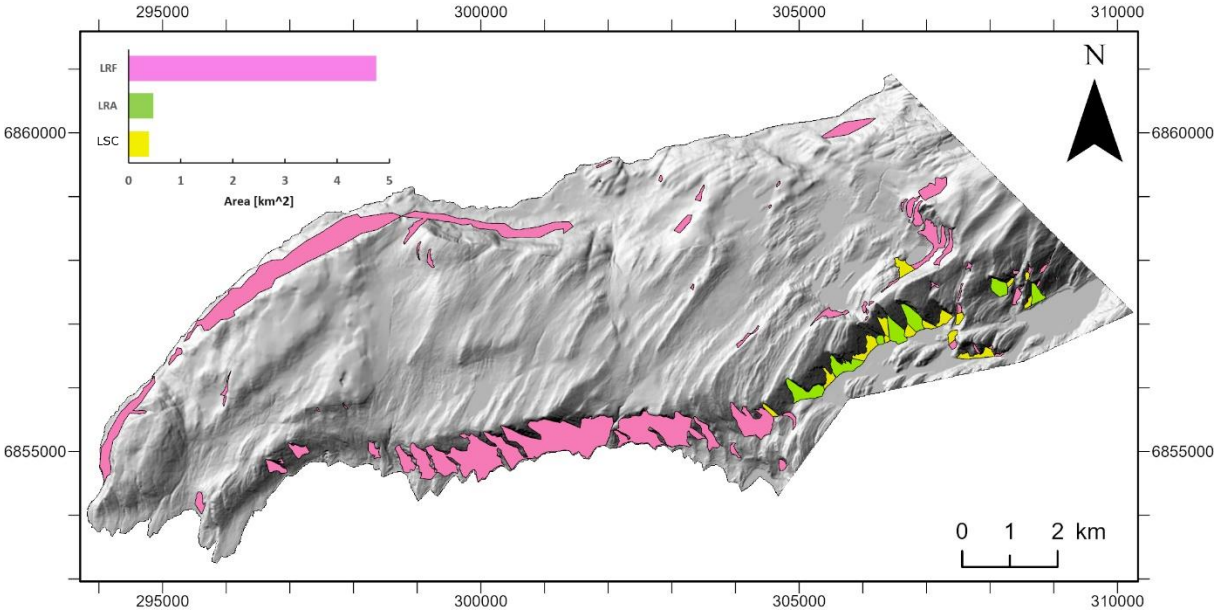

Figure 4.4 *Landslide inventory map for the Hennøy peninsula. Rock slope failure deposits are categorized according to magnitudes: rockfall (LRF), rock slope collapse (LSC) and rock avalanche (LRA).*

4.4 Volume estimations

4.4.1 Rock slope failure deposits and slide scars

Volume estimates for rock slope failure deposits and slide scar volumes exceeding 10.000 m^3 are presented in *table 4.2*. Results are organized according to rock slope failure deposits and respective slide scars. The analysis revels a minimum of 11 rock avalanche deposits (>100.000 m^3) and 19 rock slope collapse (10.000-100.000 m^3) deposits within the study area. Inventory map is presented in *figure 4.5*.

Table 4.2 *Volume estimations of mapped rock avalanche- and rock slope collapse deposits. Deposit number correlates with figure 4.5.*

Failure (#)	Failure type	Volume scar [10^6 m^3]	Area deposit [m2]	Volume deposit [m3]	Comment
1	Rock avalanche	0,82	-	-	Deposit partially submerged in lake
2	Rock avalanche	0,83	-	-	Deposit partially submerged in lake
3	Rock avalanche	0,16	24575	-	Overlapping with deposit 2
4	Rock avalanche	0,65	-	-	Deposit partially submerged in lake
5	Rock avalanche	0,12	-	-	Deposit partially submerged in lake
6	Rock avalanche	0,11	-	-	Deposit partially submerged in lake
7	Rock avalanche	0,12	-	-	Overlapping deposit 24
8	Rock avalanche	0,29	30180	0,34	
9	Rock avalanche	0,22	51351	0,27	
10	Rock avalanche	0,26	57567	0,33	
11	Rock avalanche	0,16	44711	0,19	
12	Rock slope collapse	0,081	22747	0,11	
13	Rock slope collapse	>0,01	-	-	Multiple overlapping deposits
14	Rock slope collapse	>0,01	-	-	Multiple overlapping deposits
15	Rock slope collapse	0,057	21010	0,048	
16	Rock slope collapse	0,013	17423	0,024	
17	Rock slope collapse	0,09	12323	-	Overlapping deposit 1 and 17
18	Rock slope collapse	>0,01	-	-	Deposit partially submerged in lake
19	Rock slope collapse	0,21	-	-	Deposit partially submerged in lake
20	Rock slope collapse	>0,01	-	-	Deposit partially submerged in lake
21	Rock slope collapse	0,71	-	-	Deposit partially submerged in lake
22	Rock slope collapse	>0,01	-	-	Deposit partially submerged in lake
23	Rock slope collapse	0,93	-	-	Deposit partially submerged in lake
24	Rock slope collapse	>0,01	-	-	Deposit partially submerged in lake
25	Rock slope collapse	>0,01	-	-	Multiple overlapping deposits
26	Rock slope collapse	0,044	18026	0,068	
27	Rock slope collapse	>0,01	-	-	Multiple overlapping deposits
28	Rock slope collapse	>0,01	-	-	Multiple overlapping deposits
29	Rock slope collapse	>0,01	-	-	Multiple overlapping deposits
30	Rock slope collapse	-	49120	0,14	Uncertainties in source area

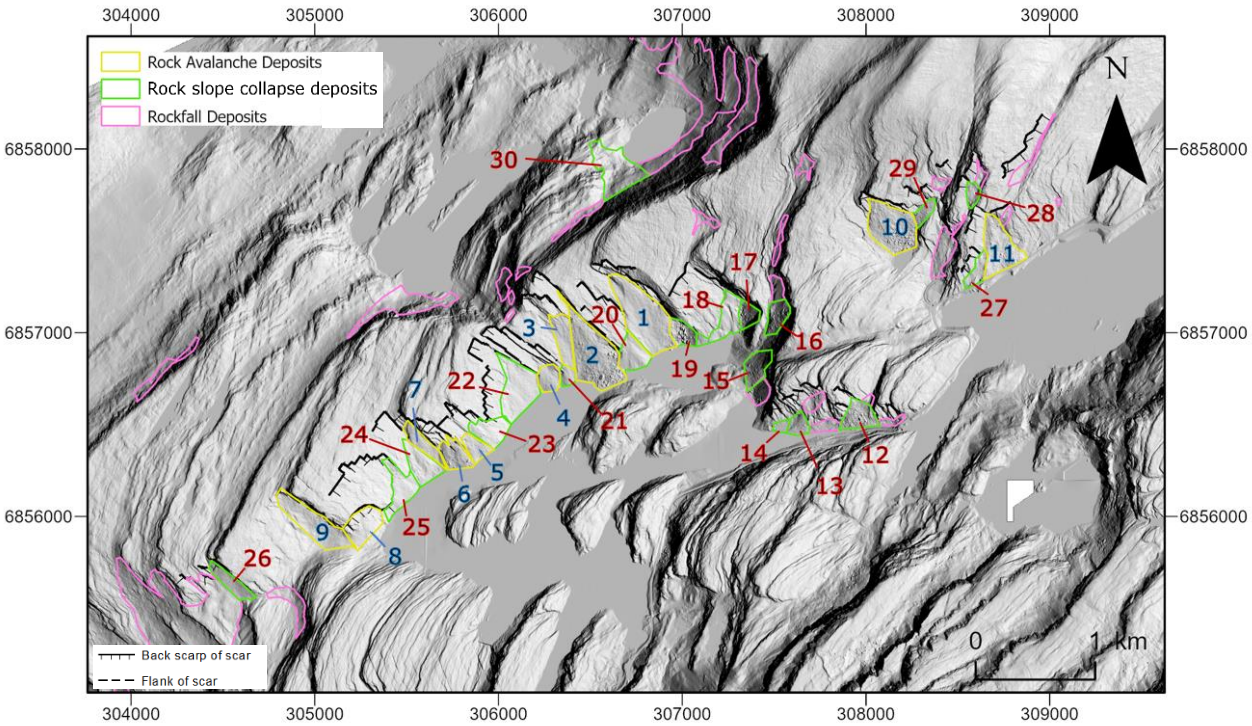

Figure 4.5 *Inventory map of all mapped rock slope collapse and rock avalanche deposits within the study area. Deposits of magnitude >100.000 m³ are indicated with blue numbering and deposits <100.000 m³ are indicated with red numbering.*

4.4.2 Fracture delimited blocks

Field mapping and remote sensing on point cloud models reveal open fractures along the SE-facing aspect of the Svelgsegga ridgeline. This led to the definition of 13 possibly unstable blocks (*table 4.3)*, where 3 of the blocks exceed 100.000 m³ in volume. Inventory map is presented in *figure 4.6.* The delimiting structures of these blocks are hereunder described.

Table 4.3 *Volume estimations of fracture delimited blocks in proximation to Svelgsvatnet lake. Block number correlates with figure 4.6.*

Block (#)	Area [m2]	Volume [m3]
1A	34816	893087
1B	8440	56926
1C	1034	8407
2	9353	366504
3A	72910	1710289
3B	29101	1165373
3C	6907	134613
4	9353	60893
5	400	5452
6	303	3655
7	510	4674
8	359	1768
9	241	3622
10	184	6693
11	1708	13929
12	1705	11461
13	3185	95634

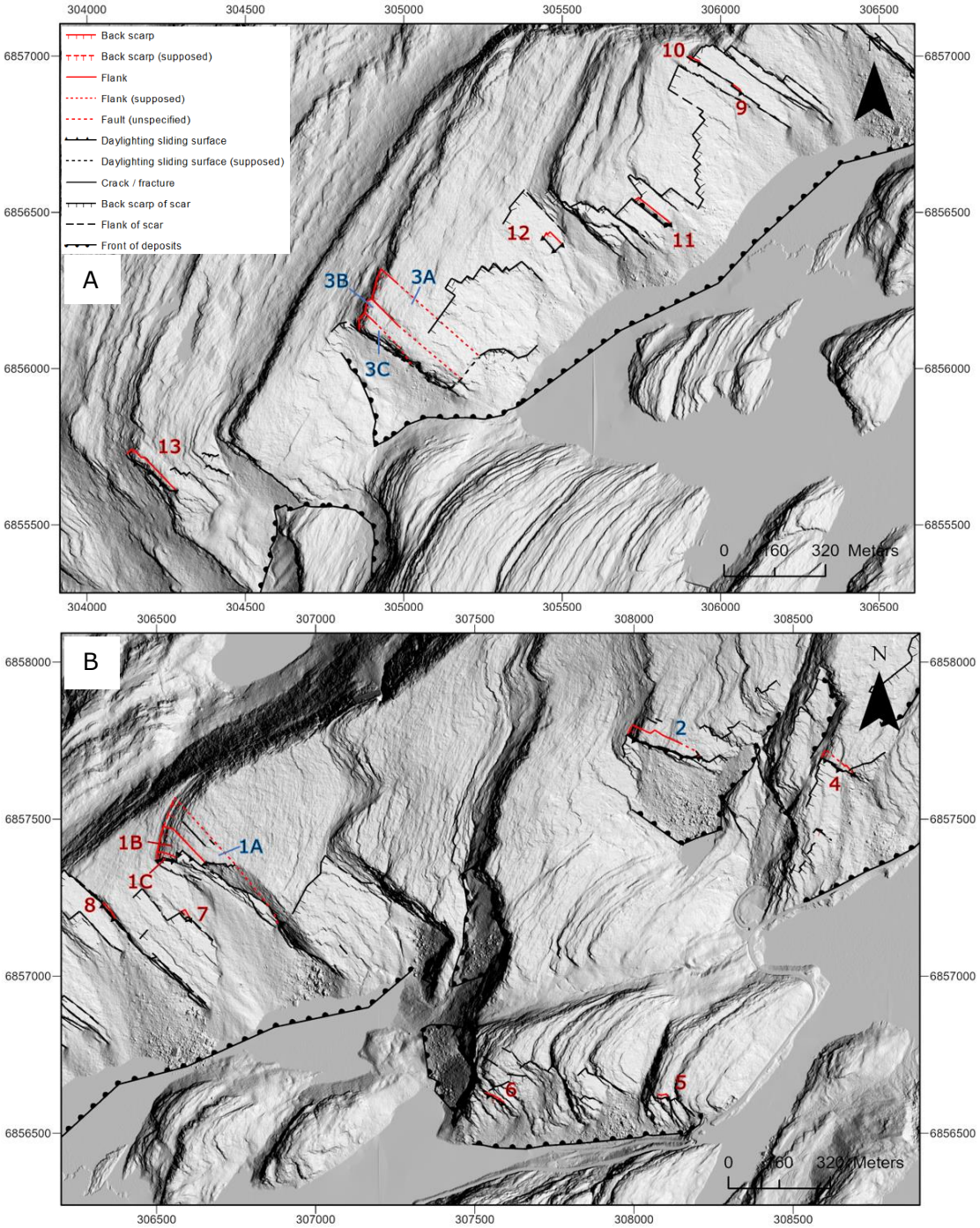

Figure 4.6 *Overview of fracture delimited blocks in proximation to Svelgsvatnet lake. Blocks of magnitude >100.000 m³ are indicated with blue numbering and blocks of magnitude <100.000 m³ are indicated with red numbering.*

4.4.2.1 Block 1

Block 1 is located NE on the Svelgsegga ridgeline. To the W the block is released by a NW-SE trending sedimentary scarp slope. For block 1A, the E-flank was defined as the eastern most NE-SW trending fracture mapped in CloudCompare. This lateral flank is less distinct compared to the more developed flanks of block 1B and 1C. Back scarp is interpreted as the top of the ridge, based on open fractures intersecting the top of the ridge. Lastly, the toe line of the block was drawn within the scarp slope. The volume of

block 1A was estimated to 0,89 mio m^3 by fitting a planar basal plane from the back scarp to the toe line.

4.4.2.2 Block 2

Block 2 is located E of the Svelgsegga ridgeline. To the west the block is released by a NW-SE trending sedimentary scarp slope. The E flank was defined according to 062/85 mean oriented fractures that were mapped in the field. Toe line was set within back scarp of the slide scar, located down-slope in relation to the block. The volume of the block was estimated to 0,37 mio m^3 by fitting a single basal plane from the back scarp to the toe line.

4.4.2.3 Block 3

Block 3 is located SW on the Svelgsegga ridgeline. Similar to block 1 and 2, block 3 is delimited to the E by a NE-SW trending sedimentary scarp slope. The E lateral flank of block 3A was defined after the easternmost NE-SW trending fracture mapped in CloudCompare. Block 3B and C were delimited after fractures located further to the SW. The fractures intersect with the top of the slope. Due to the low prominence of the fractures further down-slope, the flanks were defined by simply extrapolating the flank line to the foot of the slope. Back scarp is set in the top of the ridge. The toe line of the blocks were drawn within the back scarp of the slide scar located down-slope in relation to the block. Volume of block 3A was estimated to 1,71 mio m^3 by drawing a single basal plane from the back scarp to the toe line.

4.5 Structural Domains

The structural data that was collected at individual sites in the field and by remote sensing on ALS models was analyzed in stereonet to assess spatial variability in structural composition (*Appendix A*). By also accounting for the orientation of the slope, four structural domains were defined (*figure 4.7*). The structural domains are hereunder further described:

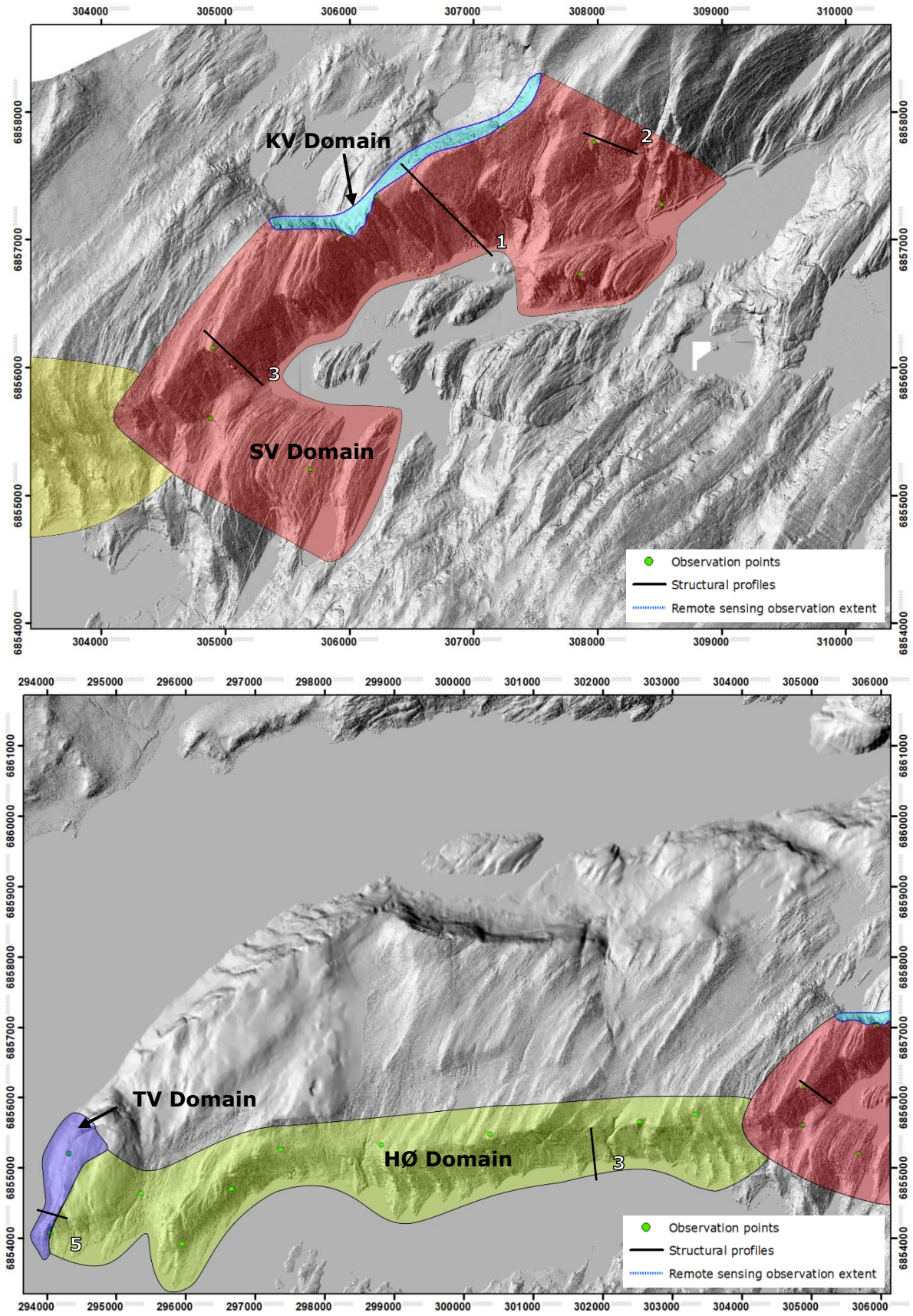

Figure 4.7 *Overview of the structural domains and locations of structural field measurements. Extent of remote structural analysis and location of structural profiles (section 4.14) are additionally indicated.*

4.5.1 Svelgsvatnet [SV] domain

The SV domain centers around the cataclinal dip-slope dominated SE-aspect of the Svelgsegga ridgeline and is comprised of field measurements along the ridge and adjacent slopes . The domain is characterized by repeating wedge-shaped slide scars along the ridgeline and corresponding deposits.

4.5.2 Kovevatna [KV] domain

The KV domain covers the mostly anaclinal NW-aspect of the Svelgsegga ridgeline and is comprised of field measurements along the ridge. Remote structural measurements on point cloud models were conducted to compare with the field measurements along the Svelgsegga ridgeline (section 4.7). Due to the regional slope-aspect, bedding dips in-slope. Compared to the SV domain, the slope appears considerably less deformed, with only some m-scale wedge-shaped slide scars occurring along the top of the ridge.

4.5.3 Hennøy [HØ] domain

The HØ domain is located along the mostly ortoclinal, S-facing edge of the Hennøy peninsula and includes field measurements along the slope. Erosion channels dig into the slope at two localities, producing N-S trending channel walls. No major deformational features or slide scars are present within the domain, distinguishing it from the SV domain. Large concentrations of rockfall deposits rest on the slope base and registered rock fall events (NVE, 2020) (appendix B) indicates frequent rockfall activity.

4.5.4 Trælvika [TV] domain

TV domain is limited to the anaclinal W-facing aspect at the horn of the Hennøy peninsula, and includes field measurements limited to two localities (90 total poles).

4.6 Geological structures

Geological structures presented in this chapter are based on field measurements. Structural analysis in Dips define five statistically significant discontinuity sets (*table 4.4*). Rough estimates of spacing, persistence and aperture were noted in the field (*table 4.5*). The documented structures are hereunder further described:

Table 4.4 *Discontinuity sets mapped in field [Dip/Dip direction ± 1σ]. Italic font indicates pole concentration below 4%. Field measurements from the KV domain are compared with structural measurements on point cloud models in section 4.7.*

Domain	SS	J1	J2	J3	J4
SV	128/35 ± 11	051/89 ± 21	289/71 ± 17	352/86 ± 20	x
KV	136/34 ± 12	030/84 ± 17	281/83 ± 9	351/79 ± 18	301/59 ± 13
HØ	119/30 ± 6	*031/82 ± 13*	298/88 ± 12	182/88 ± 11	303/27 ± 10
TV	119/32 ± 7	035/79 ± 12	265/70 ± 11	340/88 ± 20	267/31 ± 17

Table 4.5 *Spacing, persistence, shape, surface conditions and aperture of discontinuities. Note that these are rough estimates.*

Set	Spacing [m]	Persistence [m]		Shape and roughness		Aperture [mm]
		SV, KV	HØ, TV	Shape	Roughness	
SS	1,5	5 - 500	5 - 500	Planar	Smooth	1-22
J1	0,4	3 - 250	3 - 30	Planar	Smooth	x
J2	0,8	5 - 30	5 - 30	Planar	Smooth	x
J3	1,2	2 – 20	3 - 25	Undulating/Planar	Smooth	x
J4	1,4	3 - 20	3 - 12	Planar	Smooth	x

4.6.1 Bedding (SS)

Bedding is the most pronounced structure throughout the study area (global mean orientation 122/33). The regional monoclinal SW-NE striking bedding forms ridges that stand up to tens or hundreds of meters tall (*figure 4.8 A*). Bedding planes have a persistence of tens to hundreds of meters. Within the Svelgsvatnet domain, highly persistent, bedding parallel basal surfaces of slide scars span the whole length of the slope (*figure 4.8 B*).

Most bedding planes have a small aperture in the range of 1 mm – 22 mm, and are thus referred to as bedding parallel weakness zones (*figure 4.9 A*). Filling material was not specified in the field as it appeared heavily altered by weathering. Øvstedal (1971) similarly reports that most bedding planes have a thin coating of fines.

Wider, bedding parallel minor fault zones containing gouge material also occur within the study area. Field observations of the structure were confined to an open pit mine, located west on the Hennøy peninsula. Four zones with fault gouge thickness in the range 12-37 cm were mapped, containing different filling materials. The thickest zone contained a thin, brown/rust colored clayish material forming eyed structures, interlayered between thicker white and grey cemented layers (*figure 4.9 B*). The two smaller zones were composed exclusively of brown/rust colored material. Spacing between the zones was approximated to 17 m. Zones of similar characteristics are also described by Øvstedal (1971) within the Sande road tunnel, located central in Svelgen village.

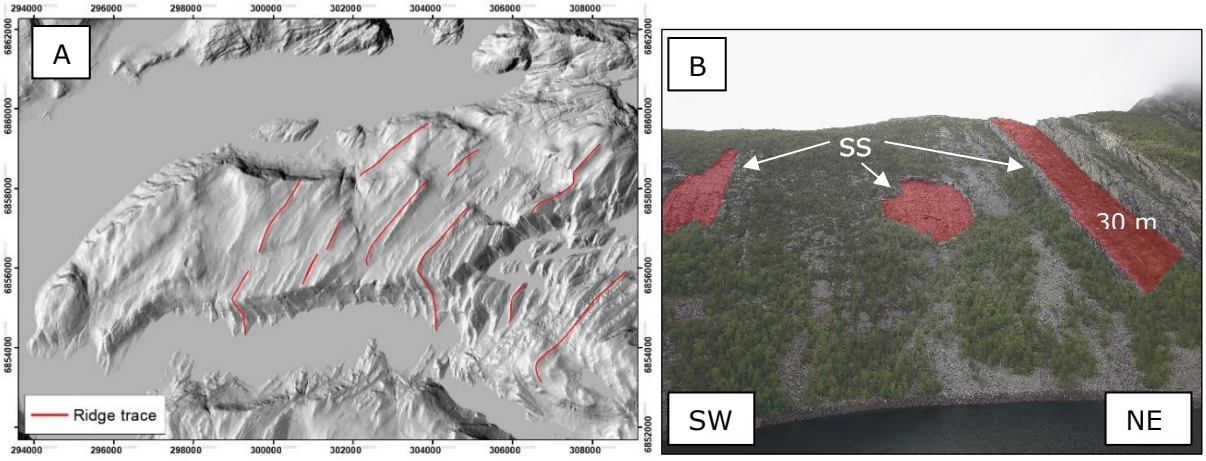

Figure 4.8 *(A) Regional scale bedding-controlled ridges. (B) Large bedding parallel planes in SV domain.*

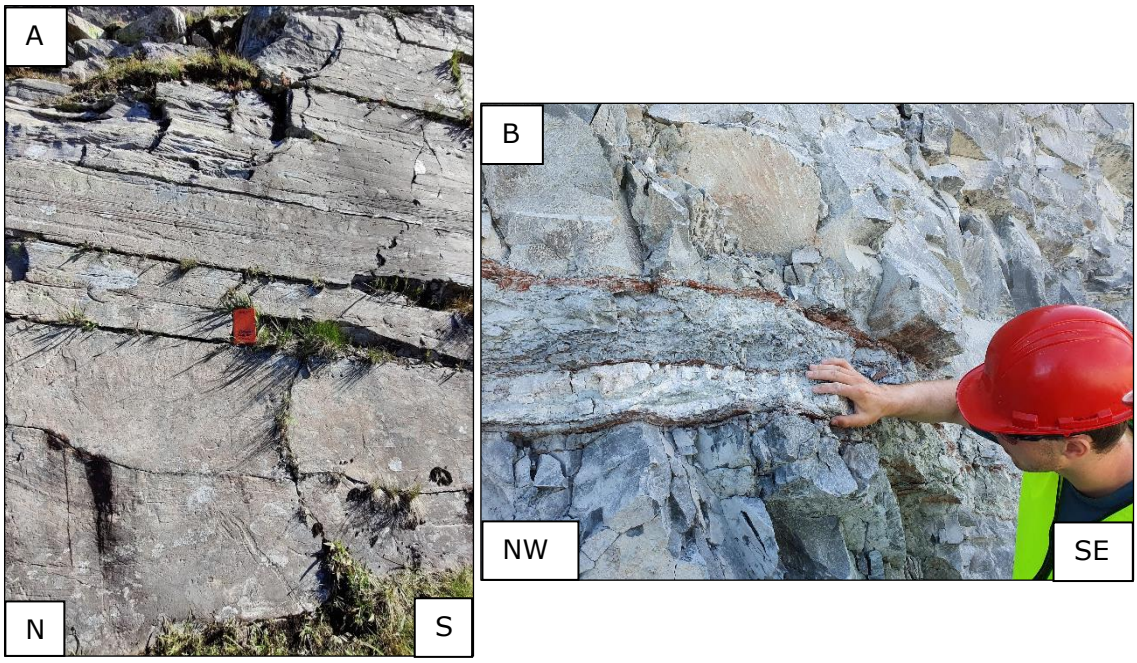

Figure 4.9 *A) Aperture on bedding planes (B) Bedding parallel minor fault zone containing fault gouge.*

4.6.2 Joint set 1 (J1)

Joint set 1 is sub-vertical, SW/NE dipping (global mean 033/83). In addition bedding, J1 is the most prevalent discontinuity set within in the SV domain. Together with bedding planes, joint set 1 form large, wedge-shaped slide scars that repeats along the SW-facing aspect of the Svelgsegga ridgeline (*figure 4.10 A and B*). Within the KV domain the structure is likewise highly persistent and can be observed as one of the intersecting joints in meter scale wedge-shaped slide scars. Within the HØ domain the joint set is only significant within the 3-4% contour range. Further inspections of point cloud models models covering the slope confirms its low regional prevalence and the was thus excluded from the kinematic analysis of the domain (section 4.13).

4.6.3 Joint set 2 (J2)

Joint set 2 is sub vertical, NW/SE dipping (global mean 292/78). The discontinuity set strikes sub parallel to the strike of the bedding and is prominent in the back scarps of slide scars in the SV domain (*Figure 4.10 A*). In the HØ and TV domain J2 delimits blocks of rockfall magnitude.

4.6.4 Joint set 3 (J3)

Joint set 3 is sub vertical, SSE/NNW dipping (global mean 354/86). Within the SV domain J3 occur in the lateral flank of slide scars (*figure 4.10B*). The intersection between J3- and J1 joints also form saw-toot shaped back scarps of slide scars (*figure 4.10 C*). In the HØ domain J3 joints create rear release for blocks on S-facing aspects (*figure 4.10 D*) and lateral release on W-facing aspects in the TV domain for blocks of rockfall magnitude.

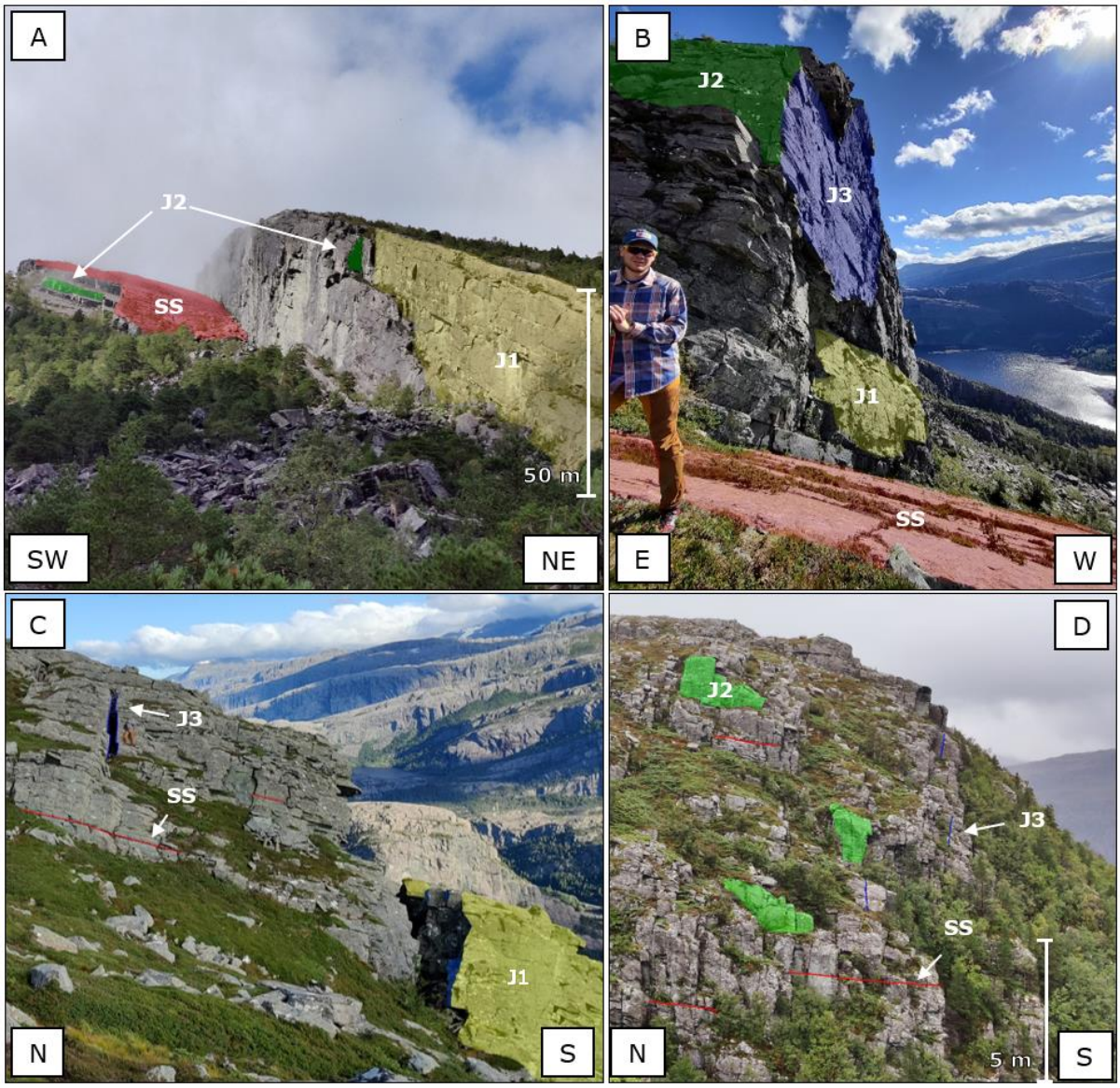

Figure 4.10 (*A and B) Interaction between SS, J1 and J2 and J3, creating wedge-shaped slide scars in the SV domain. (C) SW-striking open fracture formed by J1 and J3 in the SV domain. (D) SS, J2 and J3 delimited blocks on a S-facing slope aspect in the HØ domain.*

4.6.5 Joint set 4 (J4)

Joint set 4 is moderately, W-dipping within the TV- and HØ-domains and SW-dipping within the KV domain (global mean 303/35). In the KV domain the set form m-scale, wedge shaped slide scars in the interaction with J1 (*figure 4.11 A*). Within the TV and HØ domains the set function as basal delimitation of blocks of rockfall magnitude (*figure 4.11 B*). The set is not recognized as statistically significant within the SV-domain within the field dataset with a pole concentration <4%.

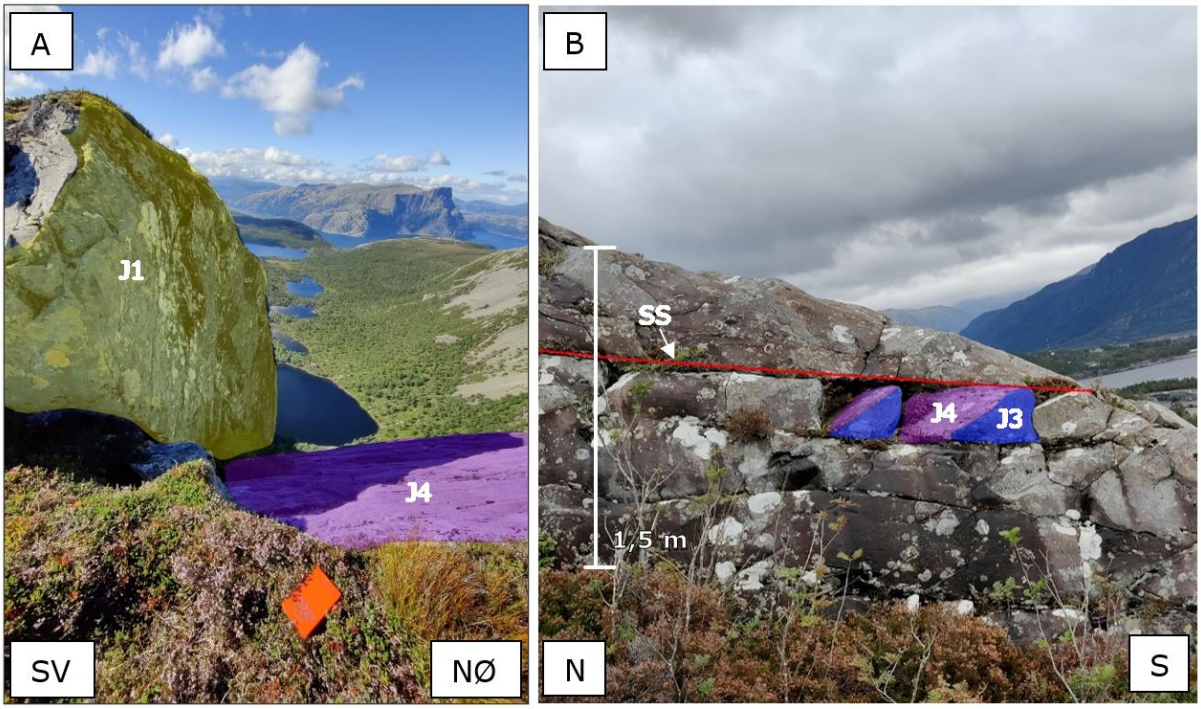

Figure 4.11 (*A) Interaction of J4 and J1 creating m-scale wedge shaped slide scars in the KV-domain and (B) J4 as basal surface in the TV-domain on a N-S striking cliff.*

4.7 Remote sensing on point cloud models

Remote structural measurements on point cloud models in CloudCompare were conducted on the NW-facing slope of the Svelgsegga ridgeline, as the slope was not accessed in the field. Additional structural measurements were conducted within the SV domain to determine the prevalence of J4.

Figure 4.12 compares the remote structural data from the KV domain to field measurements along the Svelgsegga ridgeline. The dip of discontinuities within the remote dataset score on average 14° lower when compared to the field dataset. It was therefore decided to use the field data for the kinematic analysis of the KV domain (section 4.13).

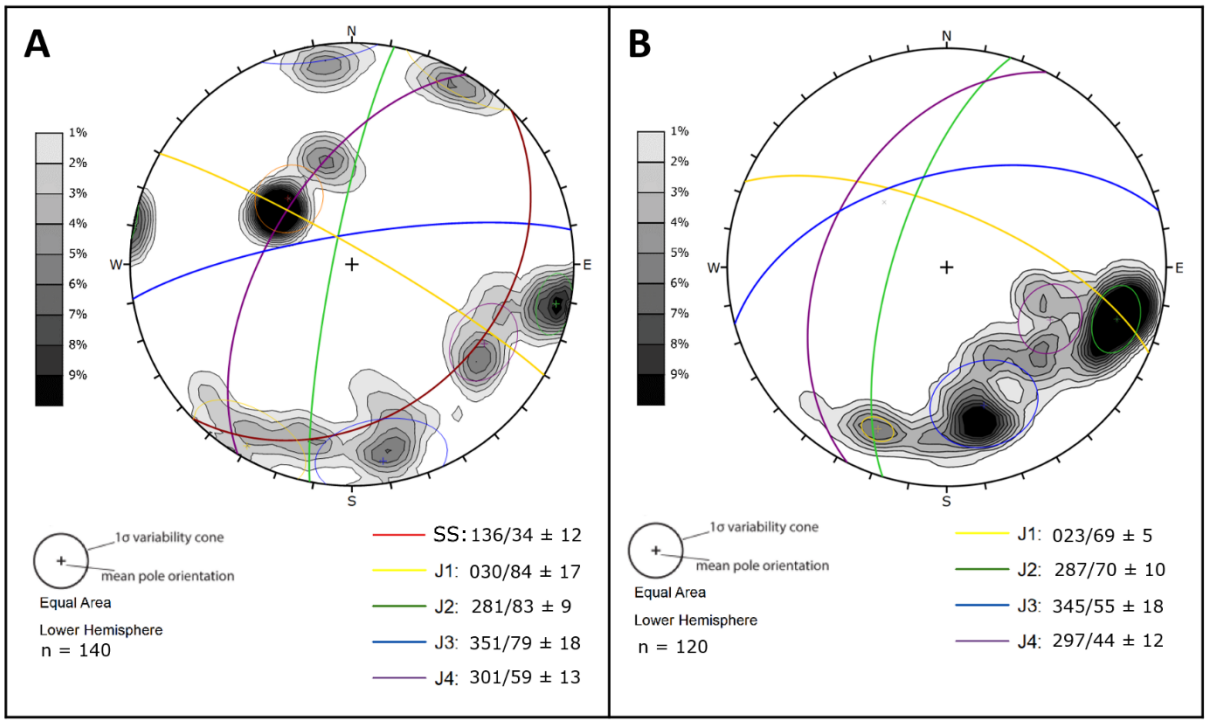

Figure 4.12 *(A) Structural field measurements from the KV domain. (B) Structural measurements from point cloud models from the KV domain.*

Joint set 4 was suspected to be prevalent within the domain, as large surfaces with persistence of ~85 m and orientation similar to J4 was seen in the field mapping, but not measured due to poor accessibility. Further observation on point cloud models in CloudCompare determines its prevalence. *Figure 4.13* presents structural measurements conducted on discontinuity J4 within the SV domain. It was therefore decided to include the structure in the kinematic analysis for the SV domain.

Appendix C compares measurements conducted with the compass method to measurements conducted with the Coltop3D method.

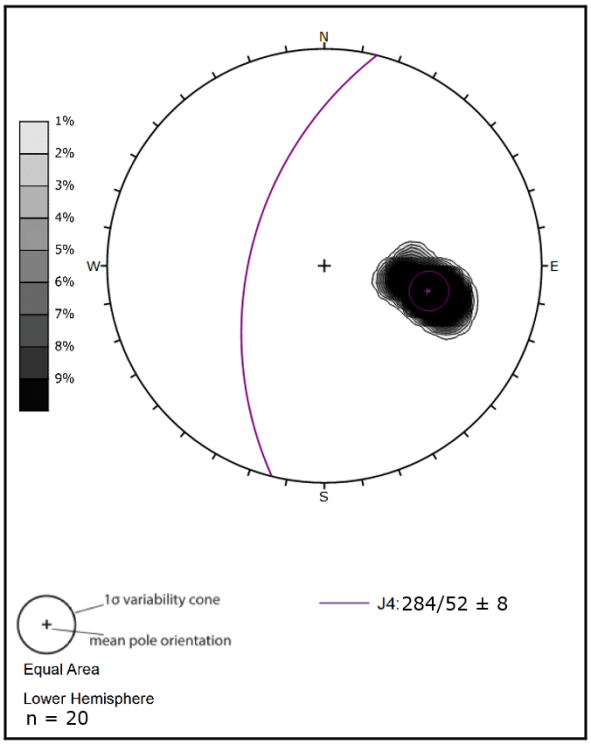

Figure 4.13 *Structural measurements from point-cloud of J4 within the SV domain.*

4.8 Structural inventory for the structural domains

Structural data from the field was structured to create regional datasets based on the structural domains (*figure 4.14)*. The regional datasets were used in further kinematic analysis to represent the kinematic feasibility for each domain (section 4.13).

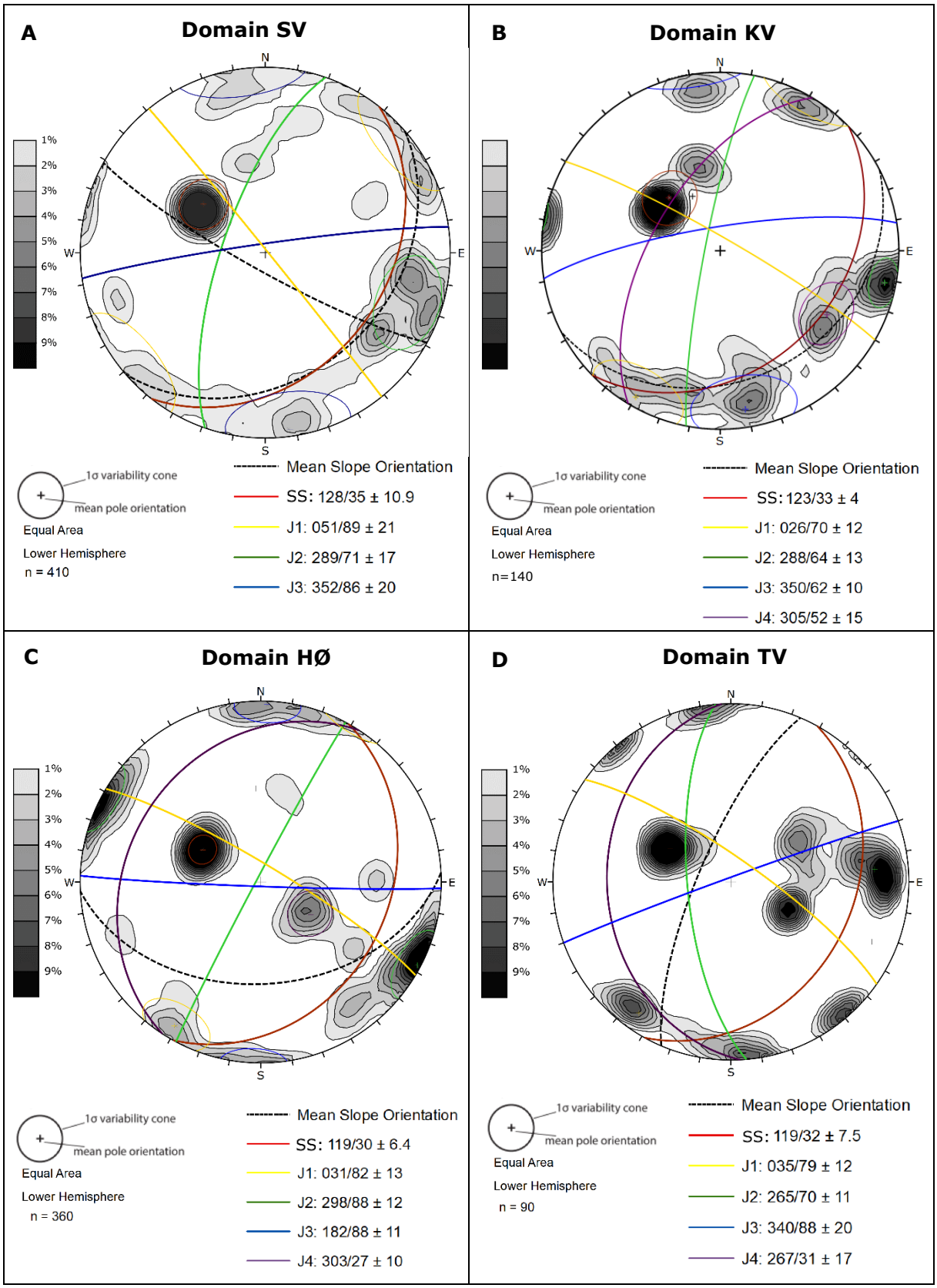

Figure 4.14 *Stereoplots of all statistically significant discontinuities within each structural domain. For the SV domain two mean slope orientations are indicated to account for two distinct slope aspects.*

4.9 Topographic conditions

The topographic conditions on the Hennøy peninsula was assessed in terms of local relief, slope angle, slope aspect. Analysis was conducted using spatial tools in ArcGIS. Slope angle-, slope aspect- and local relief maps are presented in *figure 4.15*.

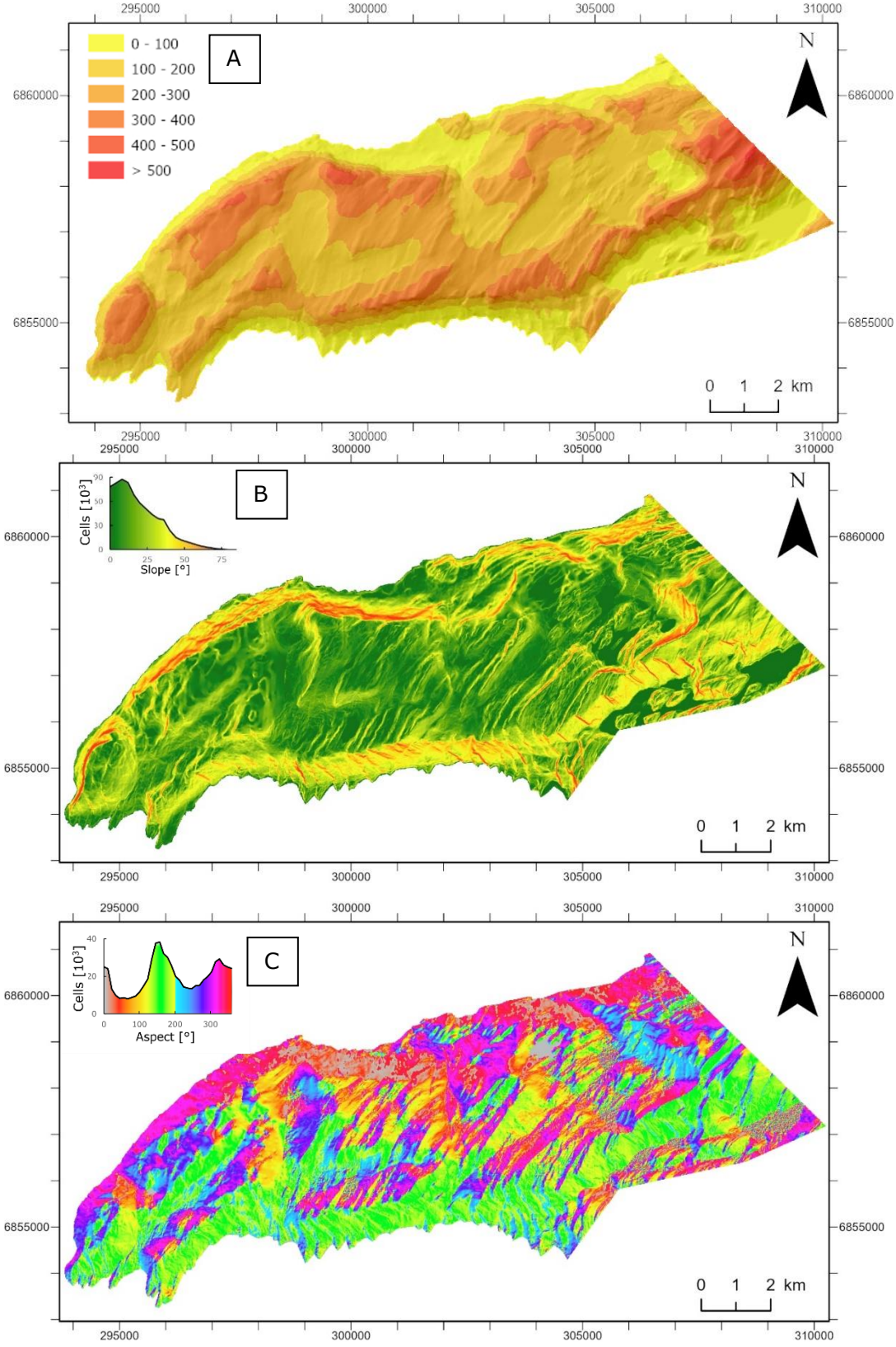

Figure 4.15 *Local relief map (elevation in m) for the Hennøy peninsula. (B) Slope gradient map for the Hennøy peninsula. (C) Slope aspect map for the Hennøy peninsula.*

It is important to note that the local relief map does not account for the seafloor topography. The waterline is within the model defined as 0 m asl. *Figure 4.16* presents a E-W transect along the southern part of the Hennøy peninsula, displaying elevation contrast when accounting for bathymetric data. Bathymetric data included has a resolution of 50m.

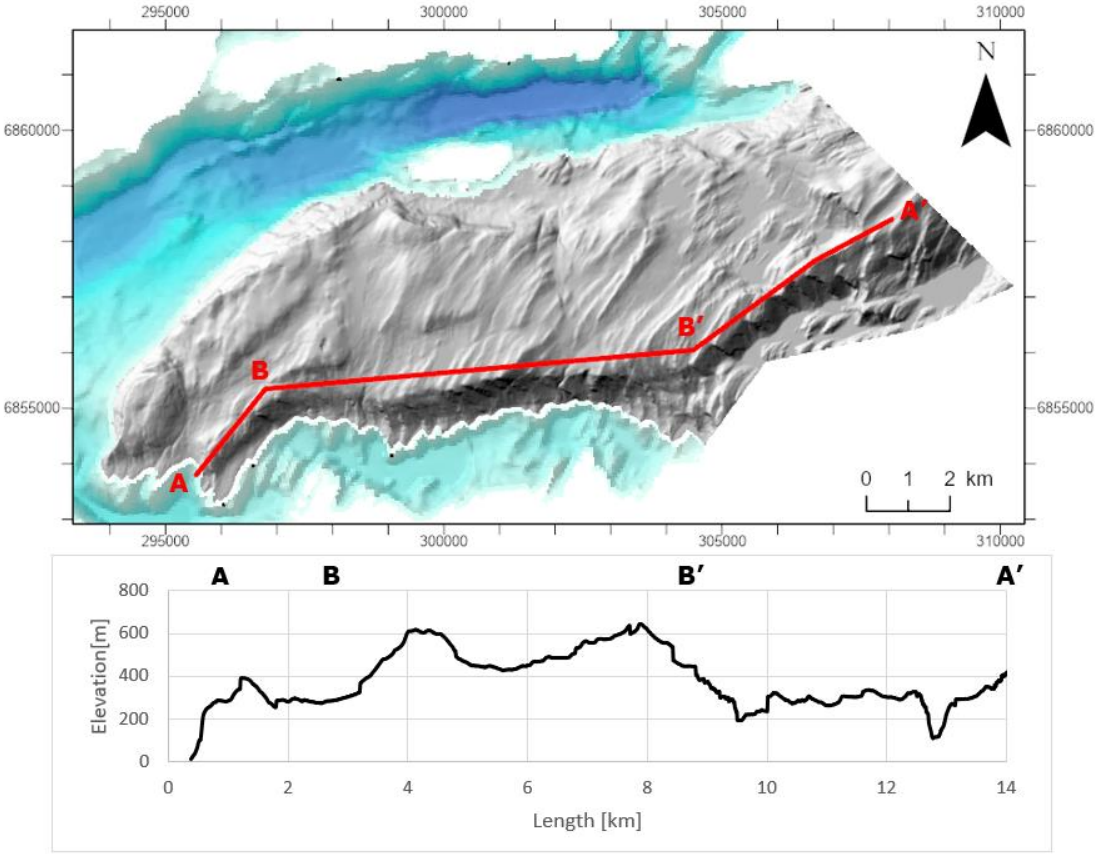

Figure 4.16 *(A) E-W transect through the southern edge of Hennøy peninsula. Blue toned DEM indicates bathymetric elevation. (B) Profile displaying relative slope height along the transect. Bathymetric data is accounted for within the profile.*

4.10 Topographic conditions vs. distribution of rock slope failures

To investigate the conditioning of topography on the distribution and abundance of rock slope failures, the local relief map (*figure 4.15 A*) and the slope angle map (*figure 4.15 B*) were overlapped with the extent of slide scars (*figure 4.3*). Spatial statistics for distribution within slide scars and the entire study area are presented in in *table 4.6*. *Figure 4.17 A and B* presents the distribution and cumulative distribution of slope angle and slope aspect within slide scar areas and the entire study area.

Table 4.6 *Spatial statistics for local relief and slope angle within slide scar areas and the entire study area.*

Analysis	Mean	STD	Distribution
Local relief – Slide scar	229 m	86	Lognormal
Local relief – Study area	233 m	75	Gamma
Slope angle – Slide scar	38 °	9	Normal
Slope angle – Study area	19 °	15	Normal

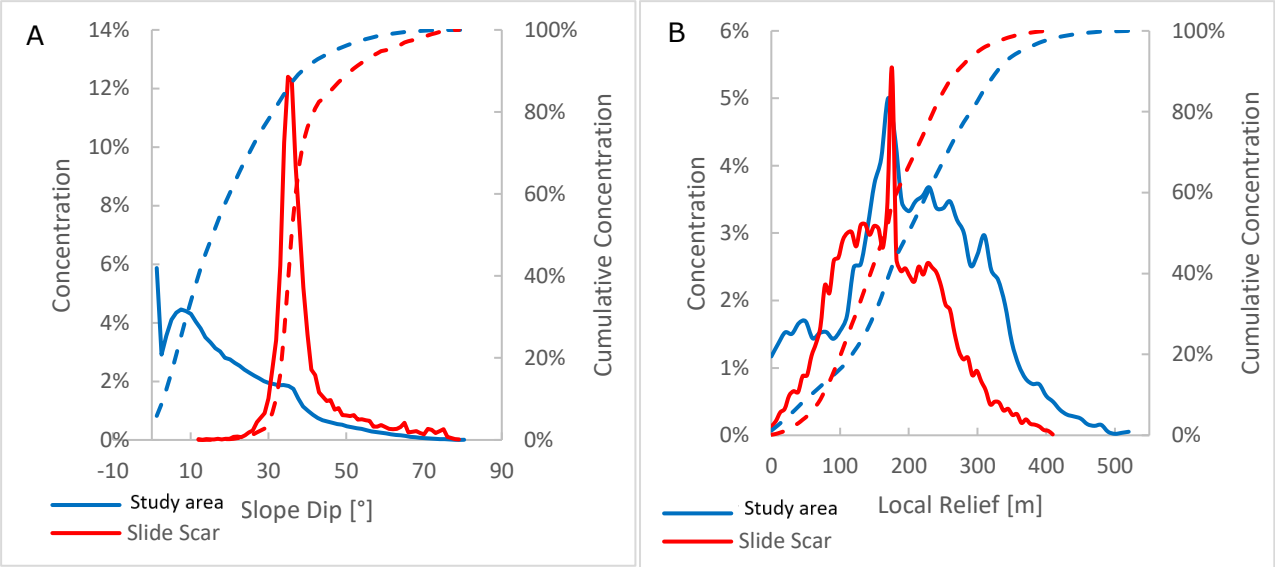

Figure 4.17 *Distribution of (A) slope angle and (B) local relief within mapped slide scars. Dashed line indicate the cumulative distribution.*

The conditioning of slope aspect on the distribution of rockfalls was assessed by overlapping the area extent of rockfall deposits (*figure 4.4*) with the slope aspect map (*figure 4.15C*). *Figure 4.18* presents rose plots for the spatial distribution of slope aspect within rockfall deposits and the entire study area.

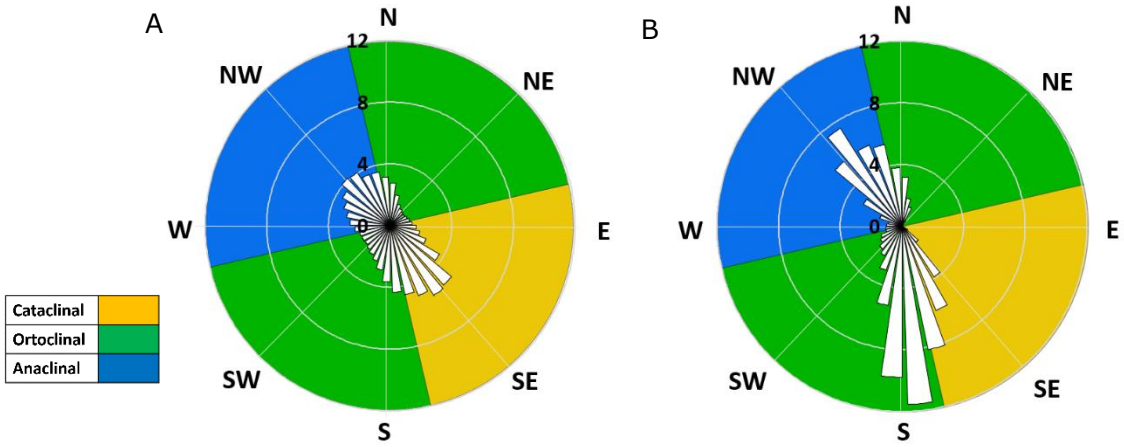

Figure 4.18 *Rose diagram A shows distribution of slope aspect within the study area. Rose diagram B shows the distribution of slope aspect within rockfall deposits. Concentration is presented in terms of percentage per interval.*

4.11 Morpho-structural domains

The slope angle- and aspect maps (*figure 4.15 B and C*) were modified and combined to create the morpho-structural map (*figure 4.19*). A fixed bedding orientation of 122/33 was defined according to the global mean from the field dataset to represent the bedding orientation within the field area. Structural domains were defined according to the methodology outlined in section 3.4.5.

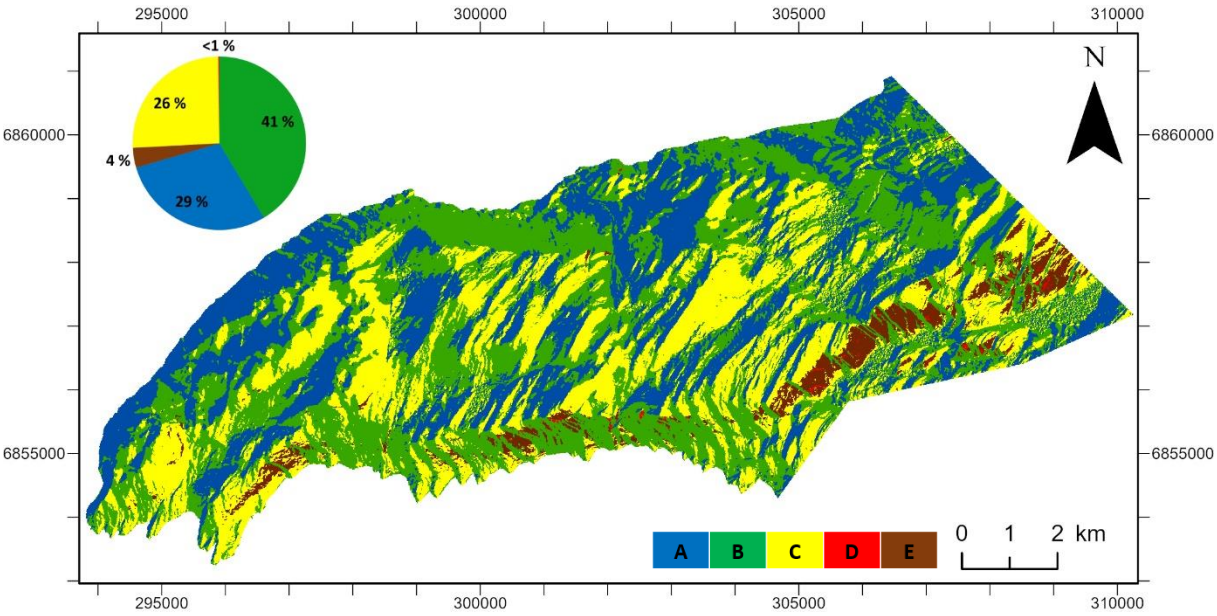

Figure 4.19 *Map showing the distribution of morpho-structural domains on the Hennøy peninsula. Pie chart shows the distribution of domains by area. (A) Anaclinal domain, (B) Orthoclinal domain, (C) Cataclinal over-dip domain, (D) Cataclinal under-dip domain, (E) Cataclinal dip domain.*

The slope angle map (*figure 4.15 B)* was overlapped with the morpho-structural map *(figure 4.19)* to project the distribution of slope angle per morpho-structural domain. Spatial statistics are presented in *table 4.7*. *Figure 4.20* show the distribution and cumulative distribution of slope angle within each domain.

Table 4.7 *Spatial statistics for slope angle within morpho-structural domains.*

Domain	Mean slope angle [°]	STD	Distribution
Cataclinal	16	11	Gamma
Ortoclinal	19	16	Gamma
Anaclinal	21	16	Gamma

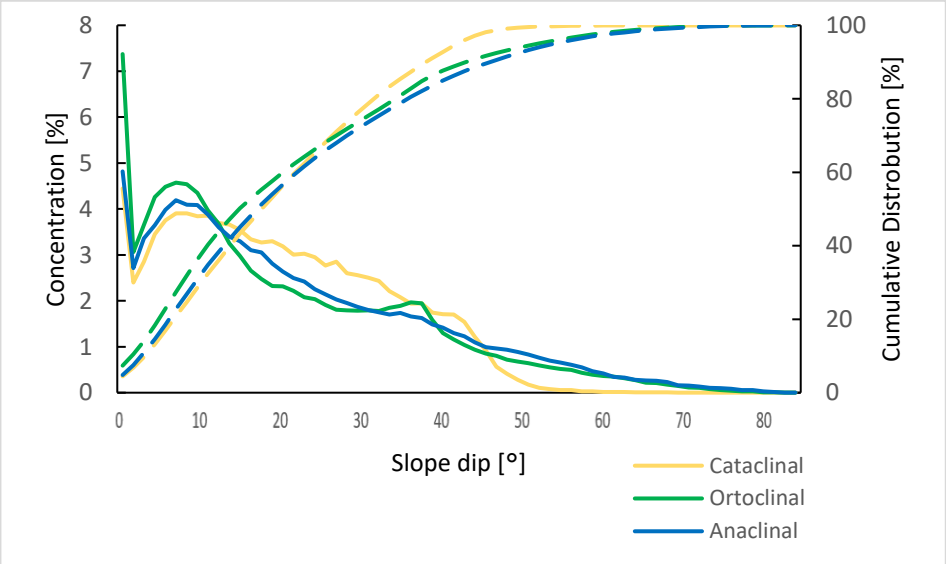

Figure 4.20 *Distribution of slope angle within morpho-structural domains. Dashed curve indicate the cumulative distribution of slope angle.*

4.12 Morpho-structural domains vs. distribution of rock slope failures

To further assess the conditioning of the morpho-structural setting on the distribution of rock slope failures, the morpho-structural map (*figure 4.19*) was overlapped with the landslide inventory map (*figure 4.4*) to produce *figure 4.21*.

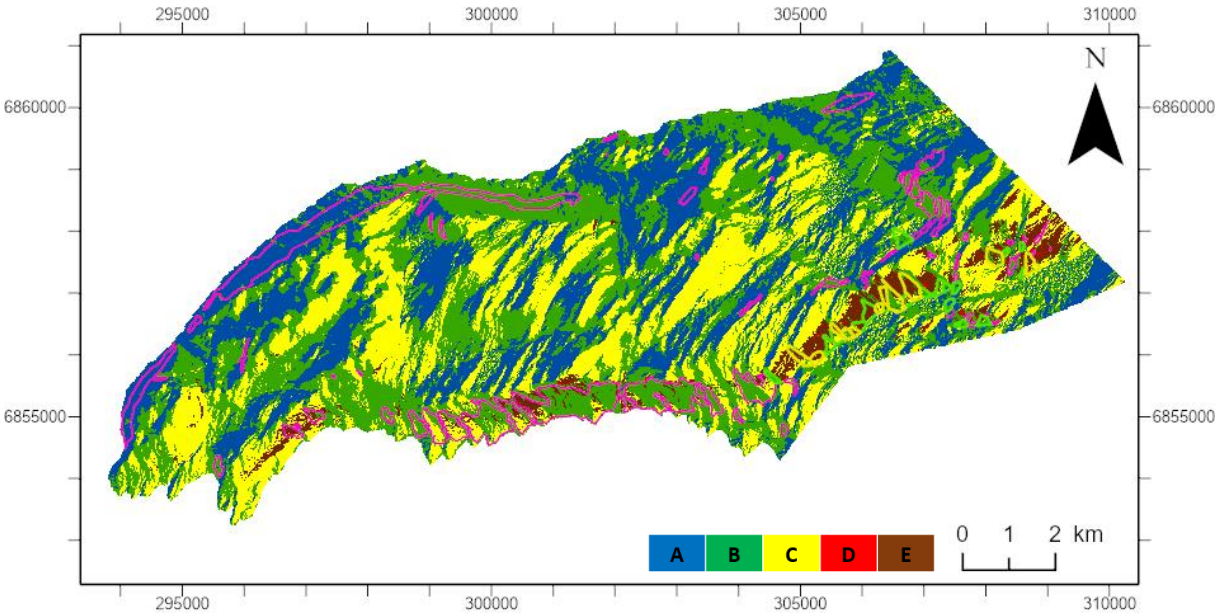

Figure 4.21 *Relation between morpho-structural domains and rock slope failure deposits. Pink outline represents rockfall-, green represents rock slope collapse- and yellow represents rock avalanche deposits. (A) Anaclinal domain, (B) Orthoclinal domain, (C) Cataclinal over-dip domain, (D) Cataclinal under-dip domain, (E) Cataclinal dip domain.*

Furthermore, *figure 4.22* presents the distribution of morpho-structural domains within rockfall- (L_{RF}), rock slope collapse- (L_{SS}) and rock avalanche (L_{RA}) deposits. Each chart indicate the following: (1) colored dots represent the proportion of the five morpho-structural domains within the area extent of the deposits. (2) Black dots represent the proportion of the five morpho-structural domains within the entire study area (equal in all tree charts).

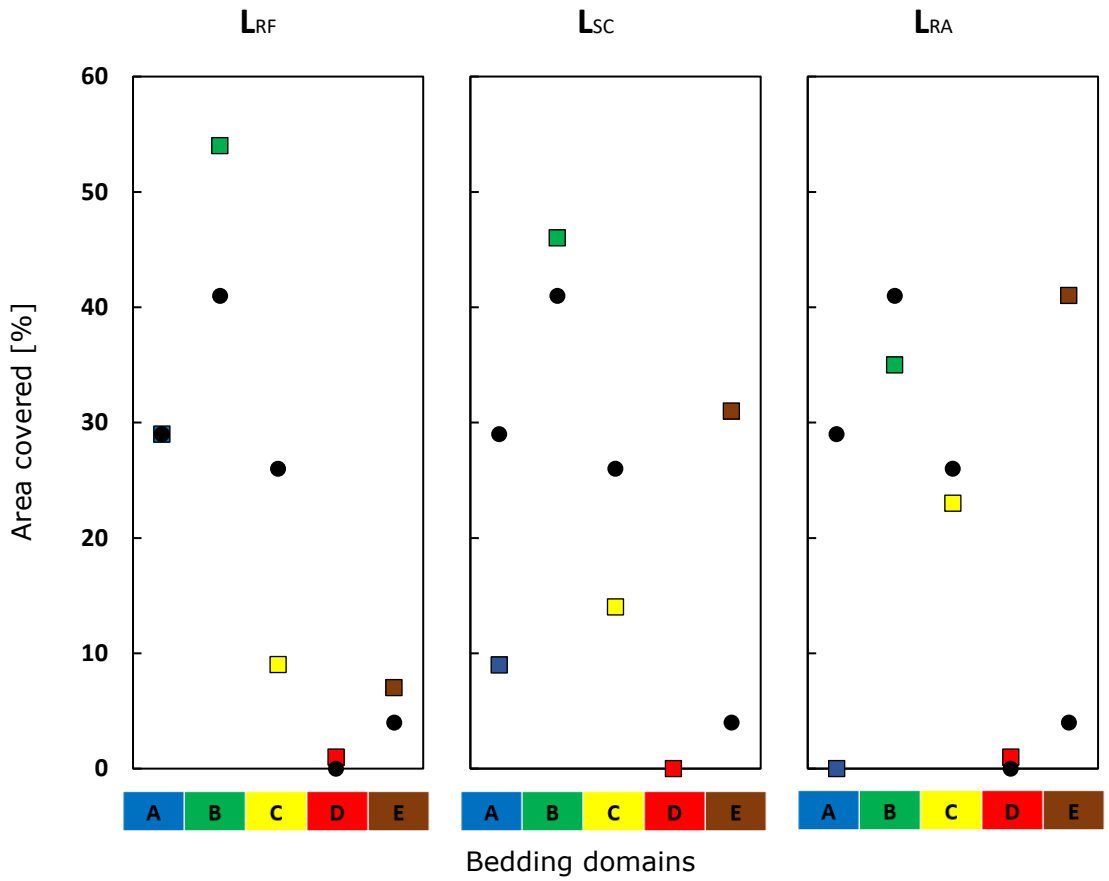

Figure 4.22 *Colored dots show the proportion of the five morpho-structural domains within rockfall deposits (L_{RF}), rock slope collapse deposits (L_{SC}) and rock avalanche deposits (L_{RA}). Black dots represent the proportion of the five morpho-structural domains within the total study area. (A) Anaclinal domain, (B) Orthoclinal domain, (C) Cataclinal over-dip domain, (D) Cataclinal under-dip domain, (E) Cataclinal dip domain.*

4.13 Kinematic analysis

Results from the kinematic analysis for each structural domain are hereunder presented. Each domain was assigned a mean dip and max angle orientation (*table 4.8*). Due to the brittle mechanical properties of the rock, flexural toppling was disregarded in the analysis. The 30° lateral limit is indicated with a shift from darker to lighter color for the critical zones of planar and wedge failure. For direct toppling lighter color indicates the critical zone for oblique toppling.

Table 4.8 *Assigned slope orientation per domain for the kinematic feasibility analysis.*

Domain	Azimuth [°]	Slope aspect [°]	Slope angle [°]	
			Mean	Max
SV	SE	139	33	84
	WSW	252	82	89
KV	-	333	62	74
HØ	-	177	43	89
TV	-	293	75	85

4.13.1 SV domain

SE-facing slopes within the SV domain are dominantly dip-slope oriented and thus limits the daylighting of SS. Planar and wedge sliding is therefore not feasible from the mean slope orientation. The shallow dip of the slope additionally limits the feasibility of direct toppling (figure 4.23 A).

Planar failure is within the max slope orientation feasible along the bedding, and wedge failure along the SS-J1 intersection line. Additionally, the bedding functions as a favorable base plane for direct toppling, forming some favorable intersections for direct toppling. Direct toppling failure is indicated as feasible from J1-J2 and J1-J3 delimited blocks and oblique toppling in the J2-J3 intersection (figure 4.23 B).

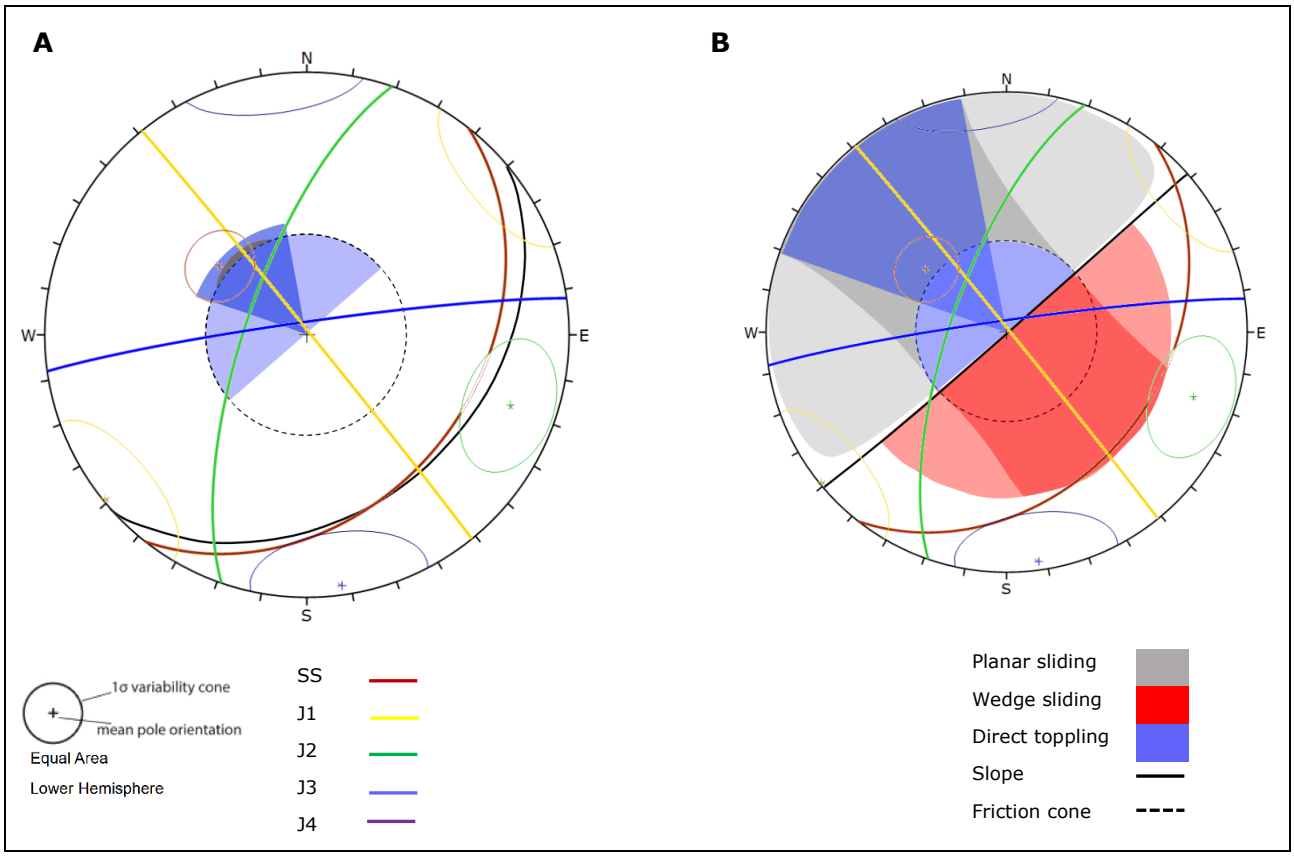

Figure 4.23 *Kinematic analysis for SE-facing slopes within the SV domain. (A) Mean slope orientation, (B) max slope orientation.*

The anaclinal WSW-facing aspect within the SV domain was represented by a single analysis due to the dominantly steep inclination of slopes. Planar sliding is indicated as partly feasible along discontinuity J4, restricted by the 30° lateral limit. Planar sliding along discontinuity J1 and J2 is restricted by its sub-vertical orientation. Wedge sliding is indicated as feasible along the J3-J4 intersection line and partly feasible from the J1-J4 intersection line. Direct toppling is indicated as feasible in the SS-J3 intersection line (*figure 4.24)*.

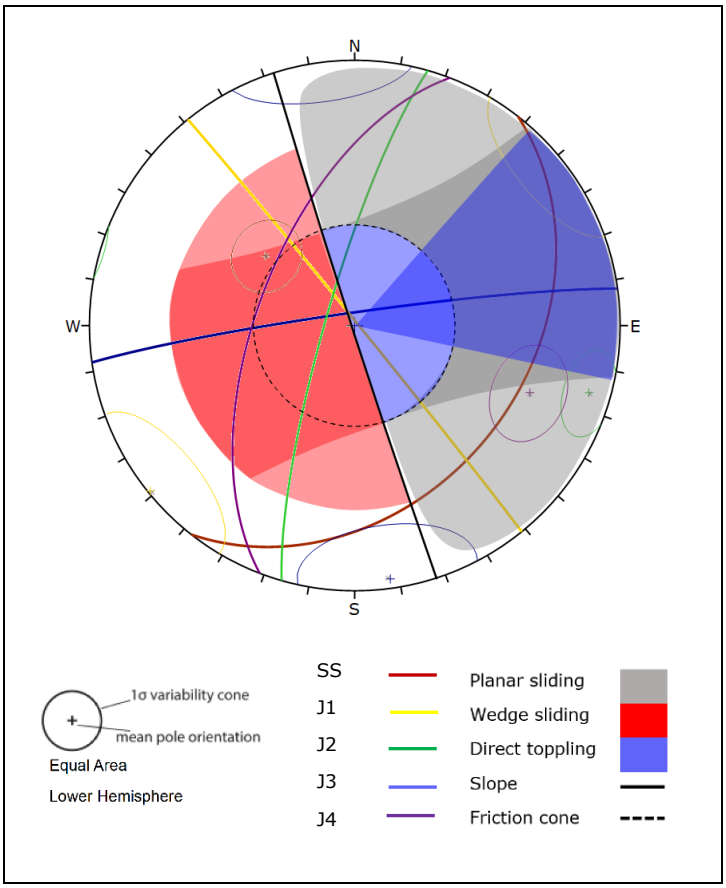

Figure 4.24 *Kinematic analysis for WSW-facing slopes within the SV domain.*

4.13.2 KV domain

The mean slope orientation within the KV domain is anaclinal oriented. Planar sliding is partly feasible along J4, limited by the daylight envelope of the slope. This is also true for wedge sliding along the J1-J4 intersection line, where the amount of critical intersections is limited by the angle of the slope. Direct toppling is not significant within this slope configuration (*figure 4.25 A*).

Within the max slope angle configuration, planar sliding along J4 is indicated as partly feasible, restricted by the 30° lateral limit. Wedge failure is feasible along the J1-J4 intersection line and partly feasible along the J1-J2 and J2-J3 intersection line, limited by the steep dip of the intersection lines. Direct toppling is neither significant within the max slope angle configuration (*figure 4.25 B*).

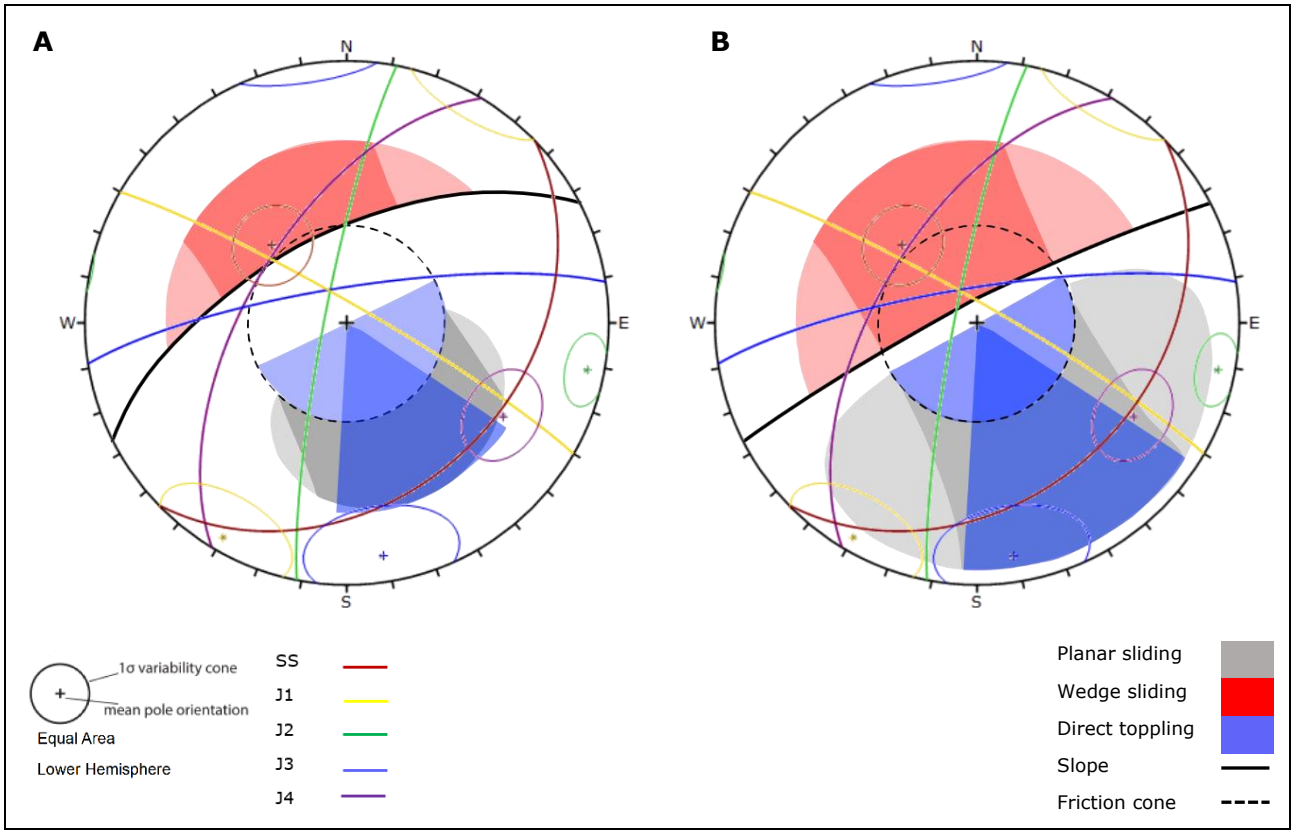

Figure 4.25 *Kinematic analysis for the KV domain. (A) Mean slope orientation, (B) max slope orientation.*

4.13.3 HØ domain

Although dominantly ortoclinal oriented, the HØ domain display a large deviation in aspect. Some sections form cataclinal orientations and some limited sections form anaclinal orientations. It was therefore decided to exclude the lateral limit from the analysis. For the mean slope configuration neither planar or wedge sliding is recognized as feasible. Discontinuity SS is favorably oriented as base plane for toppling, forming some favorable intersections with the J2-J3 intersection line for direct (*figure 4.26 A*).

Within the max slope angle configuration planar sliding is feasible along SS, J3 and partially along J2 here limited by the daylight envelope of the slope. Wedge sliding is feasible along the J2-J3 intersection line. Due to the conservative tolerance SS, J2 and J4 all form favorable orientations for base planes for direct toppling failure. The geometry of J2-J3, J2-J4, SS-J4 all form favorable intersections for toppling failure (*figure 4.26 B*).

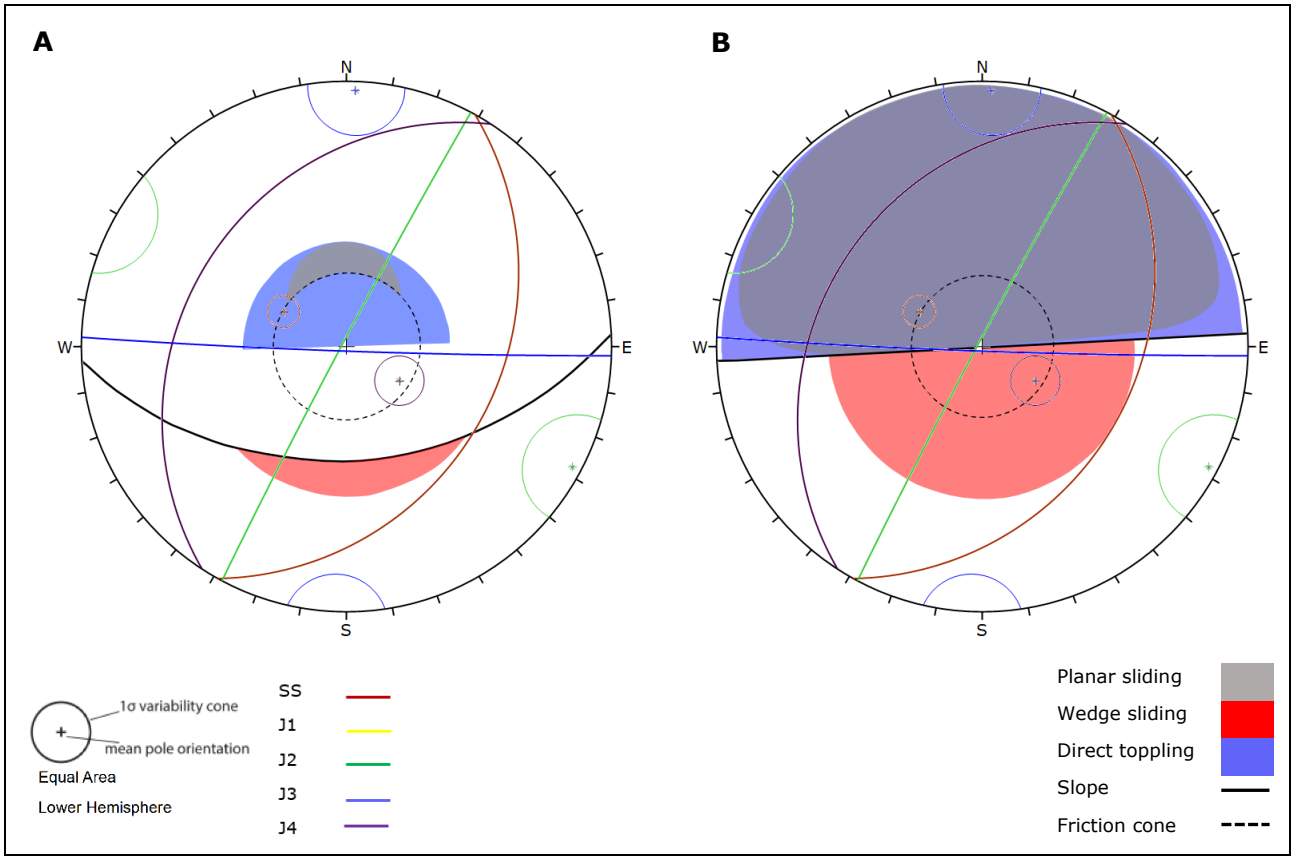

Figure 4.26 *Kinematic analysis for the KV domain. (A) Mean slope orientation, (B) max slope orientation.*

4.13.4 TV domain

The TV domain is steeply dipping and dominantly anaclinal oriented. Within the mean slope orientation, planar sliding is recognized as partly feasible along J2 with some poles limited by the 30° lateral limit. Planar failure from J4 is also recognized as partly feasible, with some poles limited by the friction cone and/or the 30° lateral limit. Wedge failure is feasible along the J1-J3 intersection line and partially feasible along the J2-J3 intersection line, here partially limited by the angle of the slope. Discontinuities J2 and J4 are both favorably oriented as basal planes for toppling, and form feasible intersections for direct toppling failure with the SS-J1 intersection (*figure 4.27 A*).

Within the max slope angle configuration the increased inclination of the slope results in more critical dataset intersection for wedge failures along the J2-J3 intersection line (*figure 4.27 B)*.

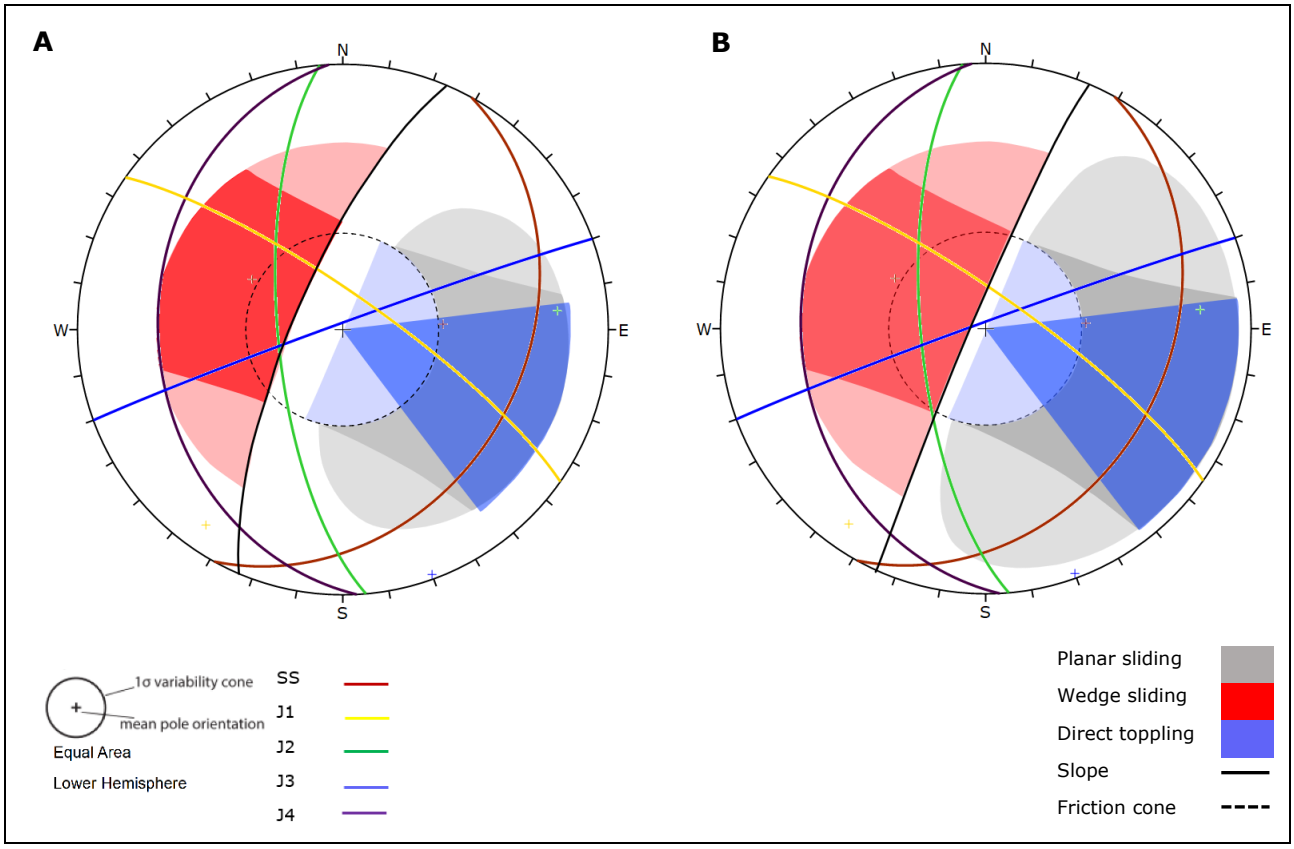

Figure 4.27 *Kinematic feasibility test for the TV domain. (A) Mean slope orientation, (B) max slope orientation.*

4.14 Structural profiles

Five structural profiles are presented in this section. Three of the profiles each intersect block 1 to 3 (section 4.4.2). These profiles strike parallel to the intersection line of SS-J1. Profile 1 transect the Svelgsegga ridge and is therefore representative of both the SV and KV domains. The two remaining profiles represent the morpho-structural interaction within the HØ and KV domains and are both striking parallel to the fall line of the slope. Structural orientation for each profile is based on the regional mean orientation of the structural domain.

Profile strike and apparent dip angles of discontinuities for each profile is presented in *table 4.9*. Structural profiles are exclusively meant as visual representation of the interaction of topography and geological structures. It is therefore important to note that persistence and spacing, as well as spatial placement of structures does not necessarily reflect in-situ conditions.

Table 4.9 *Mean apparent dip for structures belonging to defined profiles.*

Profile	Domain	Profile strike	Mean apparent dip [°]				
			SS	J1	J2	J3	J4
1	SV/KV	138	34	-	69	85	51
2	SV	141	32	-	64	90	-
3	SV	122	37	-	62	83	-
4	HØ	272	15	-	85	88	15
5	KV	023	32	77	68	87	28

4.14.1 Profile 1

Profile 1 strikes normal to the Svelgsegga ridgeline and transects block 1 (*figure 4.28*). The under-dip orientation of the upper slope does not allow for the daylighting of the bedding. Slide scars cut into the NW-SE oriented sedimentary scarp slope. The obliqueness of the scarp slope allows for the down-slope daylighting of the bedding. In the NW-most part of the profile the SV domain boundaries the KV domain. Within the KV domain J4 daylights in the slope.

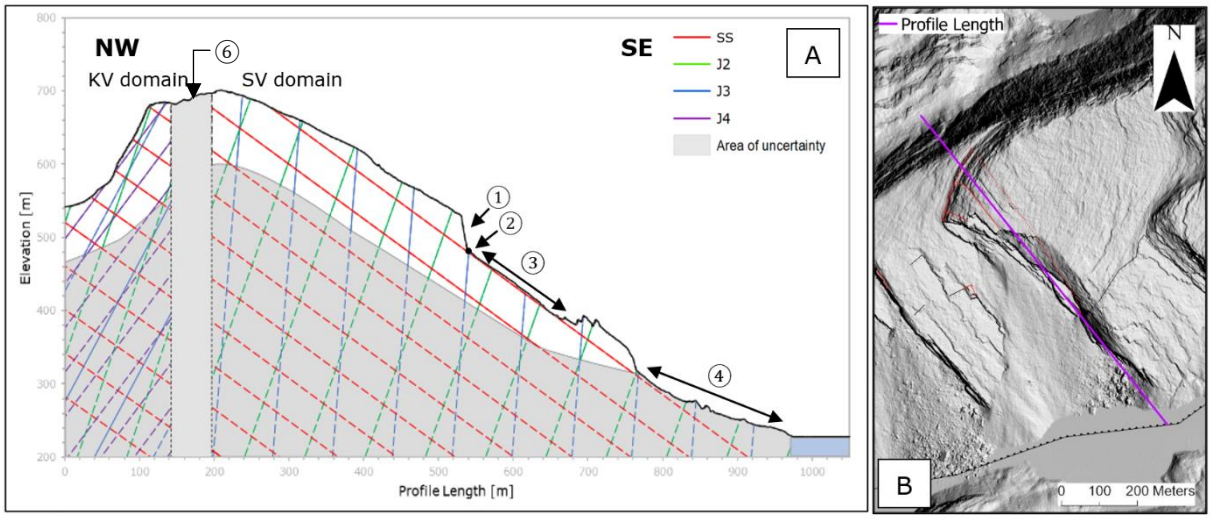

Figure 4.28 *(A) Structural profile 1. (1) Back scarp of slide scar, (2) interpreted toe line, (3) basal surface of slide scar, (4) talus cover, (6) interpreted back scarp. (B) Map cut-out of profile perimeter.*

4.14.2 Profile 2

Profile 2 strikes NW-SE, transecting block 2 east of the Svelgsegga ridgeline (*figure 4.29*). Again, the under-dip orientation does not allow for the daylighting of the bedding in the upper slope. Slide scars cut into the NW-SE oriented scarp slope. Steepening in the base of the slope in the form of a slide scar allow for the daylighting of SS.

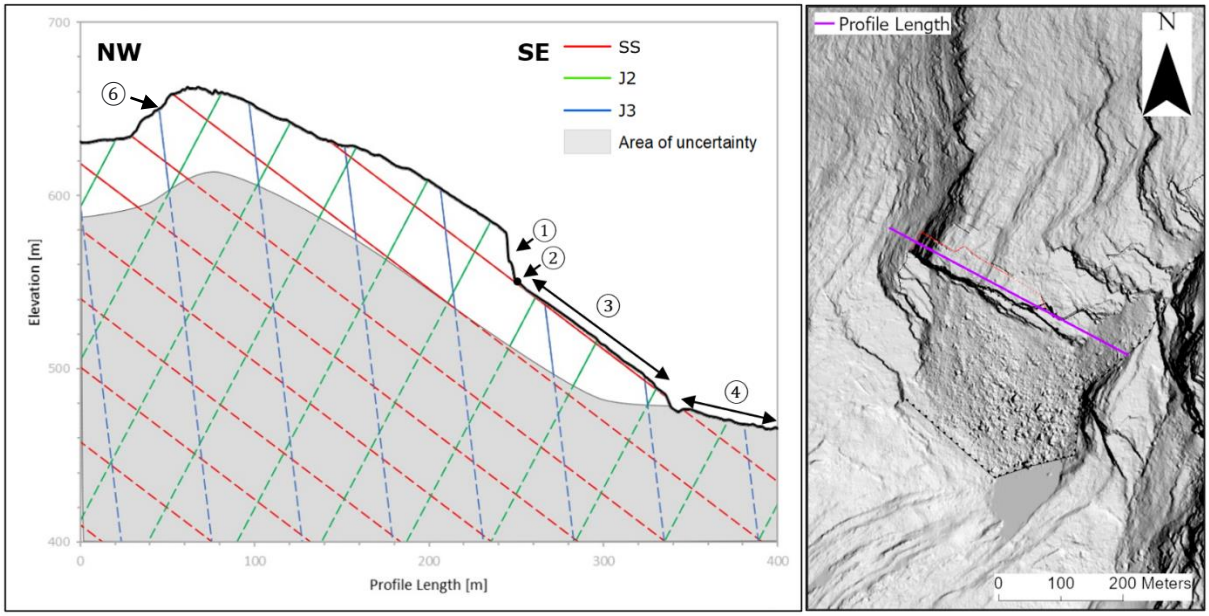

Figure 4.29 *(A) Structural profile 2. (1) Back scarp of slide scar, (2) interpreted toe line, (3) basal sliding surface of slide scar, (4) talus cover, (6) interpreted back scarp. (B) Map cut-out of profile perimeter.*

4.14.3 Profile 3

Profile 3 strikes NW-SE, transecting block 3, located on the NE part of the Svelgsegga ridge (*figure 4.30*). Some slide scars occurs along the slope, although not to the same extent as the two previous locations. Steepening in the lower part of the slope allows for daylighting of SS.

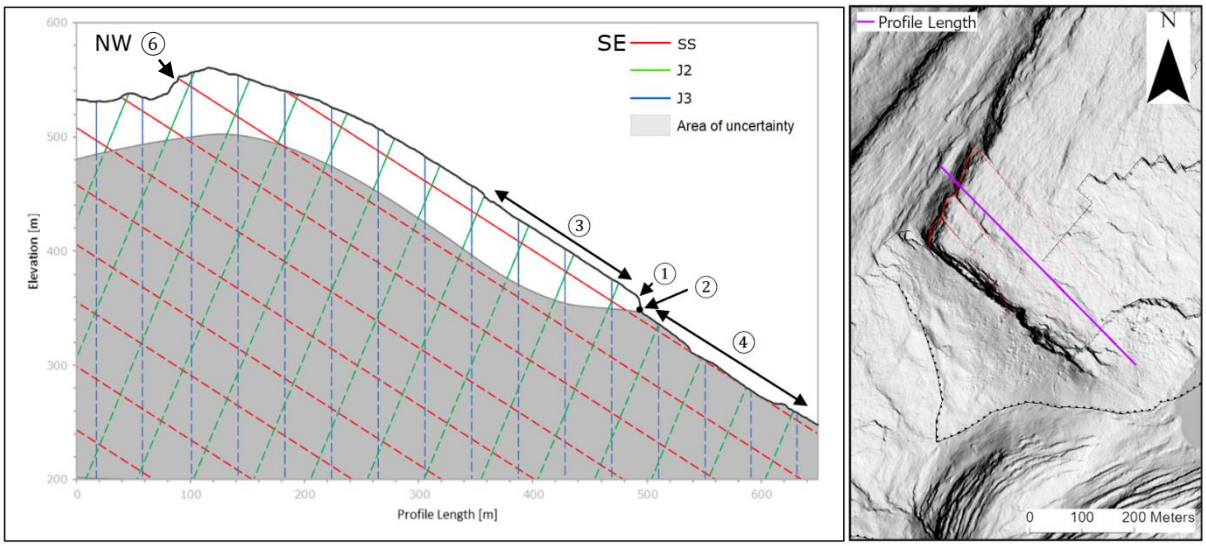

Figure 4.30 *(A) Structural profile 3. (1) Back scarp of slide, (2) potential toe line, (3) basal surface of slide scar, (4) talus cover, (6) interpreted back scarp. (B) Map cut-out of profile perimeter.*

4.14.4 Profile 4

Profile 4 strikes N-S, running parallel to the fall-line of the S-facing aspect central in the HØ domain (*figure 4.31*). As indicated in the profile, SS daylights in the slope at a shallow angle (apparent dip of 15°). Sub-vertical joint set J3 strikes normal to the profile length, interacting with J2 and SS to create favorable geometry for direct block topples in steep, SSW-facing sub-vertical cliff bands that repeats along the length of HØ domain.

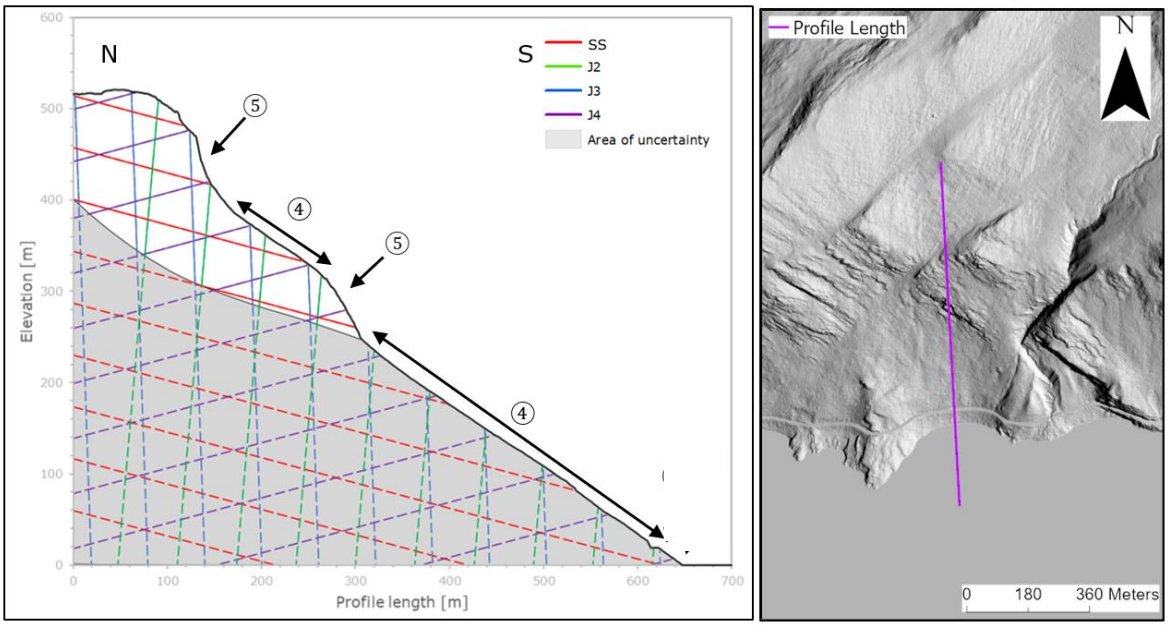

Figure 4.31 *(A) Structural profile 4. (4) Talus cover, (5) cliff band (B) Map cut-out of profile perimeter.*

4.14.5 Profile 5

Profile 5 strikes ENE-WSW, running parallel to the fall line of the anaclinal slope in the W-most part of the Hennøy peninsula (*figure 4.32*). As indicated in the profile, J4 daylights down-slope, indicated as partly feasible for planar failure restricted by the rock mass friction angle. The intersection of J2-J3 additionally form feasible intersections for wedge failure within slope sections steeper than that indicated in the profile.

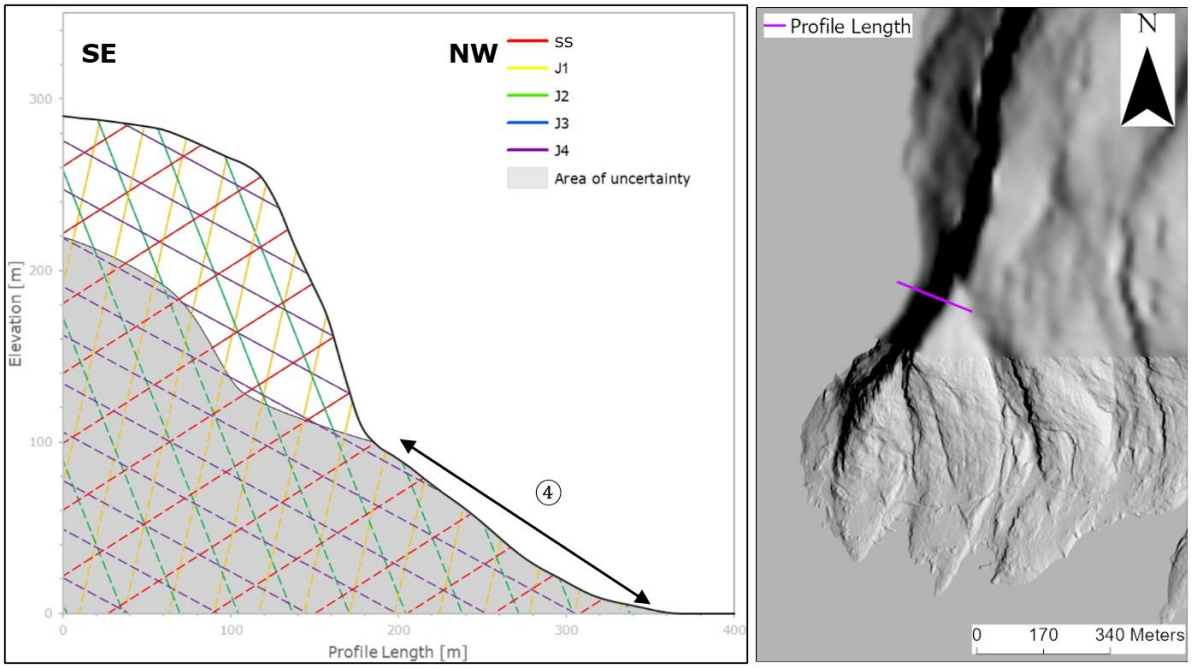

Figure 4.32 *(*A) Structural profile 5. (4) Talus cover. Note that topo line is based on DEM with cell size 10x10 m. (B) Map cut-out of profile perimeter.

4.15 Laboratory measurements

4.15.1 Uniaxial compressive test

Two cores were test uniaxially. Results from uniaxial compressive testing is presented in *table 4.10*. Stress-strain curve is drawn in *figure 4.33.*

Table 4.10 *Results from the uniaxial compressive test.*

Sample	σ_c [MPa]	E [GPa]	V	Fracture angle [°]
1	215,6	58,84	0,31	16
2	223,7	60,14	0,34	18

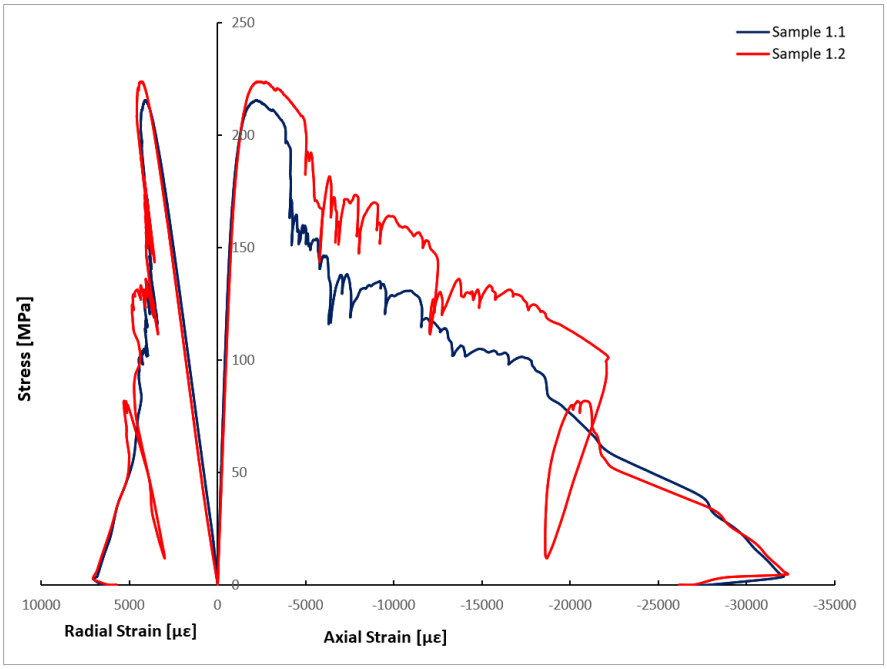

Figure 4.33 *Stress-strain curve for samples tested in the uniaxial compressive test.*

4.15.2 Triaxial compressive test

Eight cores were tested triaxially. Results from triaxial compressive testing is presented in *table 4.11*. Stress-strain curve is drawn in *figure 4.34*.

Table 4.11 *Results from the triaxial compressive test.*

Sample	σ1 [MPa]	σ3 [MPa]	Fracture angle [°]
1.3	237,7	5	18
	264,4	10	
1.4	229,9	2,5	24
	246,2	5	
	277,7	10	
1.5	234,9	2,5	22
	251,3	5	
	279,9	10	
1.6	277,7	10	21
	316,6	20	
1.7	235,4	2,5	20
	250,3	5	
	277,6	10	
1.8	238,3	2,5	22
	255,2	5	
	282,2	10	
1.9	319,5	20	24
1.10	247,7	5	22
	273,4	10	
	289,5	15	

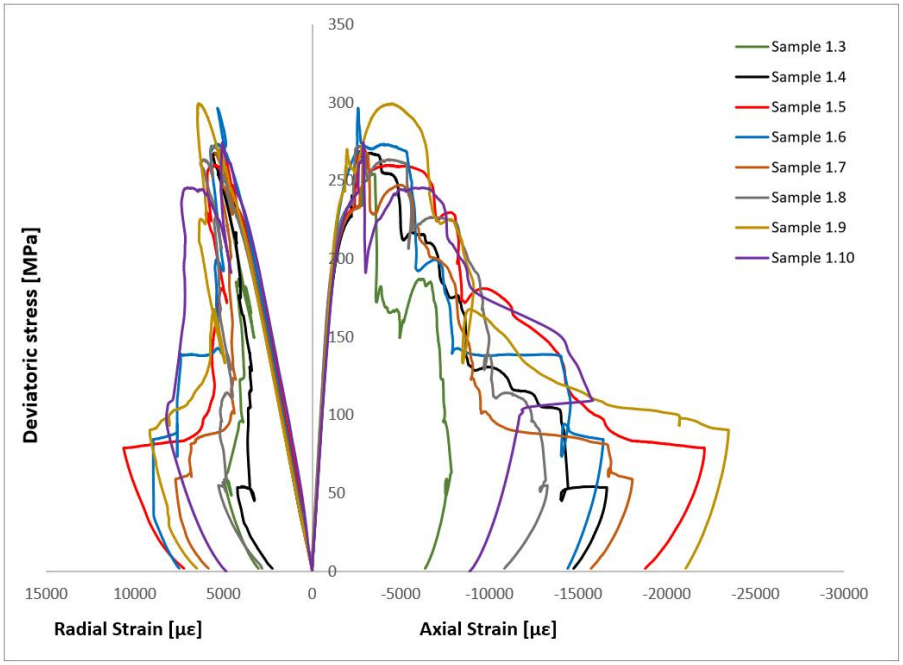

Figure 4.34 Stress-strain curve for samples tested in the triaxial compressive test.

4.15.3 Brazilian test

In total 11 samples were tested in the Brazilian test. Resulting failure pressures and estimated tensile strengths are presented in table *4.12*

Table 4.12 *Results from brazil test.*

Sample	Force [kN]	Diameter [mm]	Length [mm]	σ_t [MPa]
2.1	30,68	50,78	24,93	15,4
2.2	38,55	50,81	25,04	19,3
2.3	33,71	50,86	24,70	17,1
2.4	33,34	50,85	24,95	16,7
2.5	30,83	50,80	25,02	15,5
2.6	29,72	50,84	24,93	14,9
2.7	22	50,53	24,92	11,1
2.8	33,59	50,80	23,72	17,8
2.9	27,26	50,80	24,47	14,0
2.10	38,46	50,84	24,67	19,5
2.11	31,09	50,76	24,20	16,1
			Mean σt [MPa]	16,1
			STD	2

4.16 Analysis of laboratory measurements

4.16.1 Mohr-circle and linear regression

Figure 4.35 presents a Mohr-circle plot for the uniaxial and triaxial tests with the fitted regression curve. Values for σ_{ci} and m_i are presented within the figure.

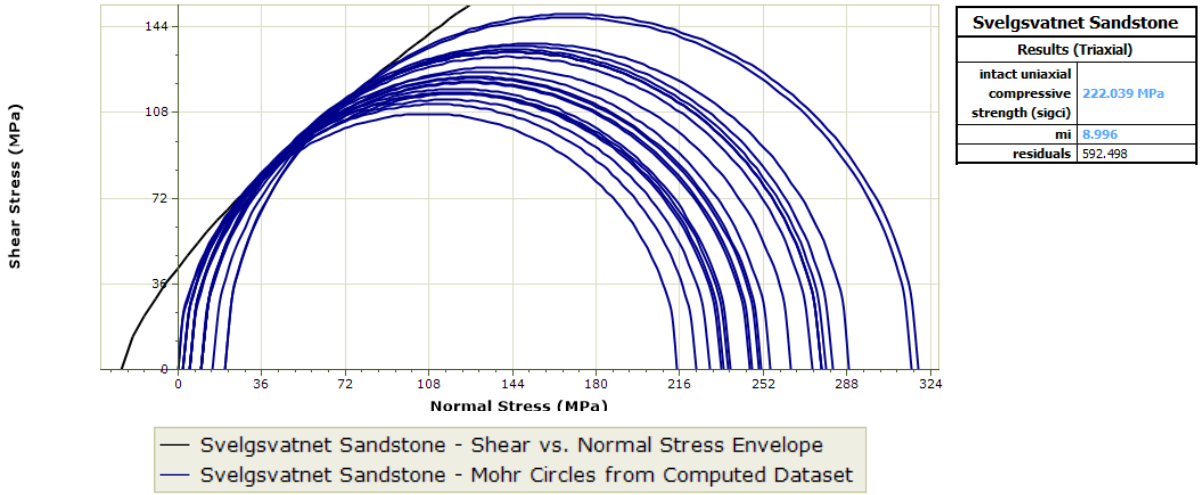

Figure 4.35 *Mohr-circle plot for the entire uniaxial and triaxial dataset with fitted regression curve.*

4.16.2 Rock strength parameters

The Hoek-Brown criterion requires an estimate of GSI. Field estimates of GSI were conducted along the Svelgsegga ridgeline. Rock structure was defined as "blocky – very blocky" and surface conditions as "good – fair". The GSI value was accordingly set to 55 ±5. As stated by Hoek (2000) it is considered more realistic to quote a range for the GSI rather than a discrete value.

Table 4.13 presents input parameters derived from uniaxial and triaxial tests and the resulting rock strength parameters. E-modulus for intact rock e_i was set as the mean e-modulus from the uniaxial compression testing . Disturbance factor D was set as 0.

Table 4.13 *Rock mass parameters according to laboratory testing and RocData analysis.*

Parameter		Value	Source
Hoek-Brown classification			
Intact uniaxial compressive strength	σ_{ci} [MPa]	222,04	RocData
Geological strength index	GSI	55±5	Field estimate
Intact Hoek-Brown constant	m_i	9,0	Rocdata
Disturbance factor	D	0	Undisturbed rock slope
Intact E-modulus	E_i [MPa]	59,49	Mean from UCS-test
Hoek-Brown criterion			
Hoek-Brown constant	M_b	1,8	RocData
Material constant	s	0,007	RocData
Material constant	a	0,5	RocData
Mohr-Coulomb fit			
Cohesion	c [MPa]	11,64	RocData
Friction angle	φ [°]	31,08	RocData
Rock Mass Parameters			
Intact tensile strength	σ_{ti} MPa]	16,1	Mean from Brazil-test
Tensile strength	σ_t [MPa]	0,83	RocData
Uniaxial compressive strength	σ_c [MPa]	17,86	RocData
Global strength	σ_{cm} [MPa]	41,21	RocData
Modulus of deformation	E_{rm} [GPa]	24,29	RocData

4.17 JRC, JCS and φ_r

Estimates of JRC, JCS and φ_r were conducted on 9 individual bedding planes in the field. The resulting parameter statistics are presented in *table 4.14*. Parameter φ_r was calculated according to *equation 3.6*. Parameter φ_b was defined from the lab results (*table 4.13*). One mean value of r and R was estimated for each of the 9 bedding planes tested in the field, resulting in 9 estimates of φ_r. Due to the resulting low data concentration, φ_r was simply assigned a normal probability distribution to represent the parameter uncertainty (*figure 4.36*). Distributions for JRC and JCS are presented in *figure 4.37*. Both variables were fitted with lognormal distributions.

Table 4.14 *Calculated values and statistics for JRC, JCS and φ_r from field data.*

Parameter	Measurements	Mean	STD	Max	Min
JRC	66	6,4	3	16	2
JCS	90	167,2	26,8	250	120
R	80	58,2	3,8	68	47
r	80	50,9	6,1	61	37
φ_r	9	29	0,9	30	27,5

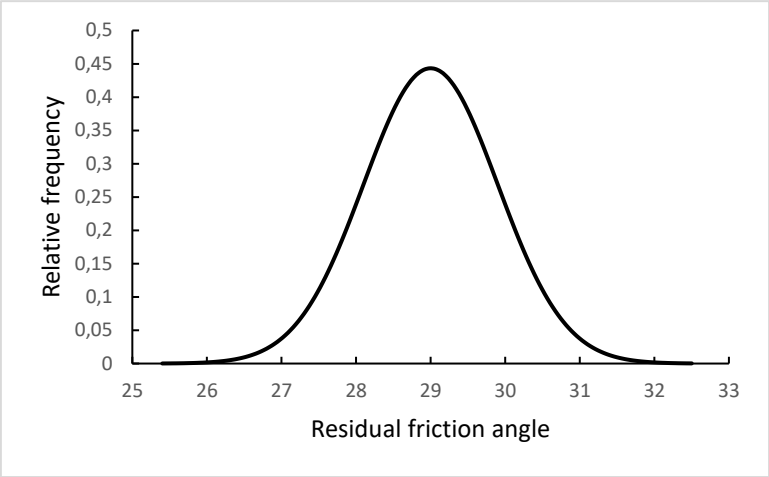

Figure 4.36 *Distribution for residual friction angle, further applied in probabilistic stability analysis*

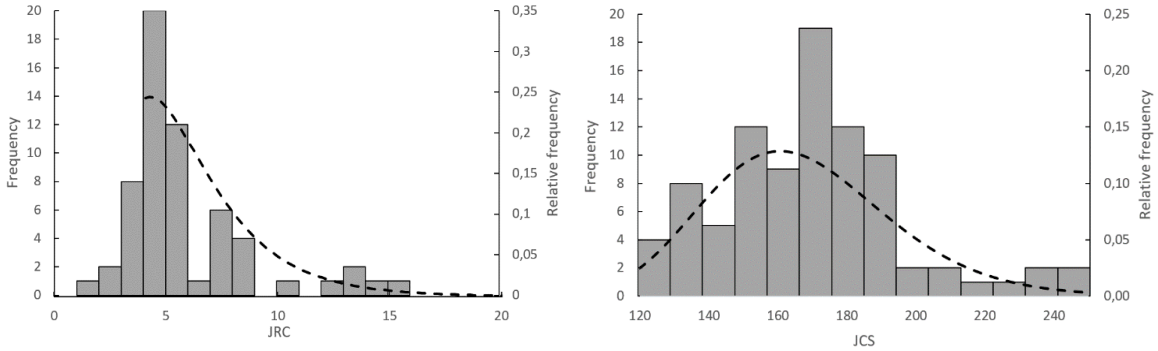

Figure 4.37 *Distribution of JRC and JCS values from field work, further applied in probabilistic stability analysis.*

The Barton-Bandis failure criterion for bedding planes was projected according to the parameter values presented in *table 4.12* (*figure 4.38*).

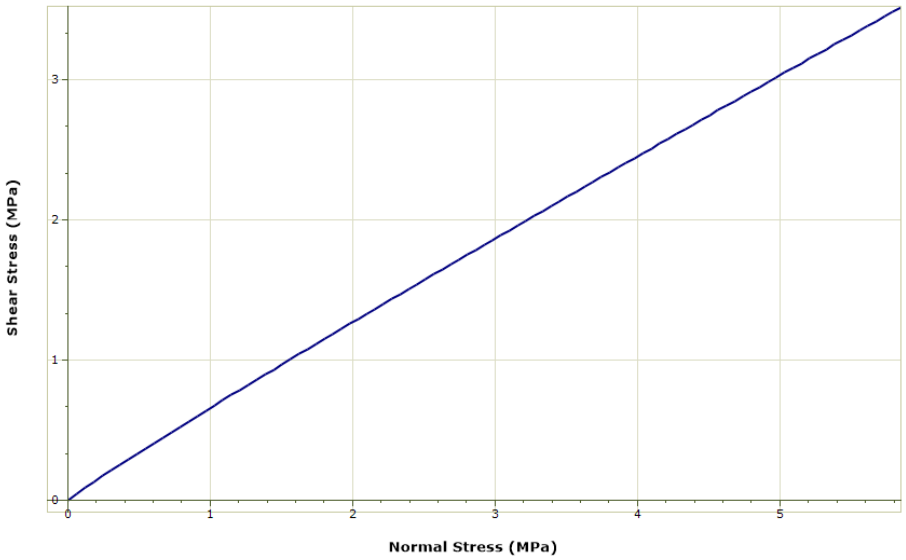

Figure 3.38 *Barton-Bandis shear strength criterion for bedding planes.*

4.18 Probabilistic stability analysis

Three probabilistic stability models 1A-C were constructed in Swedge to represent different combinations of discontinuity plane characteristics (*table 4.15*). Input- and output parameters are hereunder presented.

Table 4.15 *Overview of the modelled discontinuity characteristics.*

Model	Discontinuity SS	Discontinuity J1
1A	Filling material shear strength	Rock mass strength
1B	Filling material shear strength	Rock mass strength, c=0
1C	Bedding plane shear strength	Rock mass strength, c=0

4.18.1 Geometry

Input parameters delimiting the wedge geometry of the SWedge model is presented in *table 4.16*.

Table 4.16 *Input parameters for slope orientation for probabilistic stability analysis. Note that these are fixed parameters.*

Variable	Value [°]
Upper Face	132/20
Slope	205/89
Orientation SS	128/33
Orientation J1	051/89

The model is dimensioned after slide scar 2, presented in section 4.4.1. Volume of the model initially turned out somewhat over-dimensioned and was tweaked by lowering the rock mass unit weight. Model and in-situ wedge dimensions are presented in *table 4.17* and depicted in *figure 4.39*.

Table 4.17 *Dimensions of the wedge model and in-situ dimensions, derived from measurements on point cloud models in CloudCompare.*

Variable		Model	In-situ
Unit weight of rock mass	[MN/m^3]	0,025	0,027
Volume	[10^6 m^3]	0,825	0,833
Height of wedge max	[m]	88	74
Area SS	[m^2]	31024	31485
Area J1	[m^2]	18492	19327

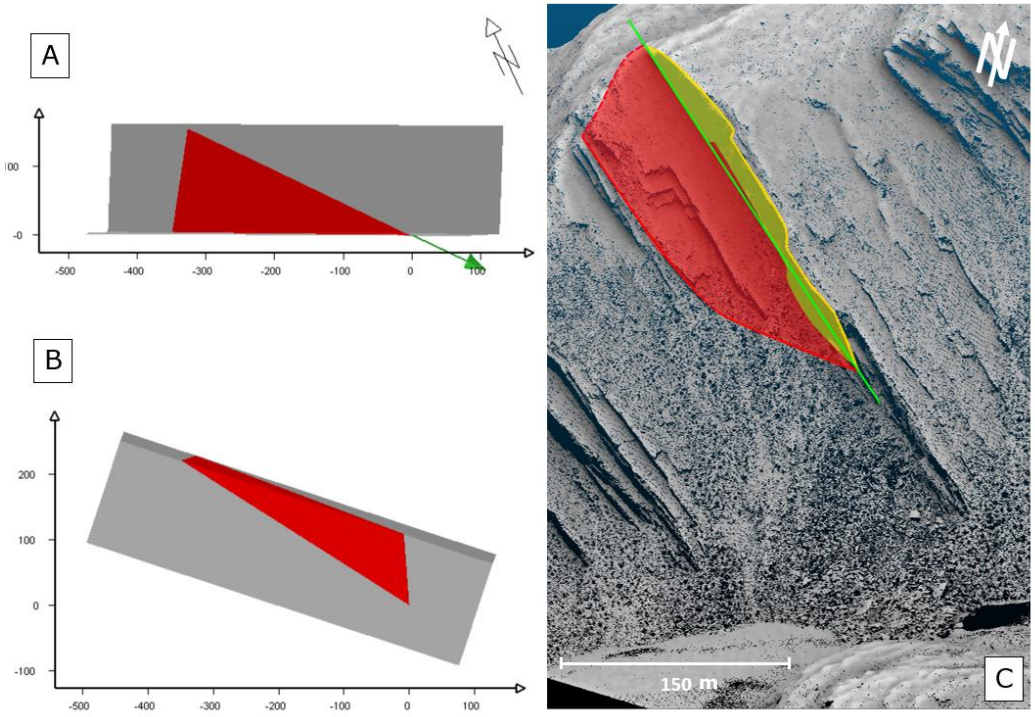

Figure 4.39 *(A) Top-down view of the Swedge wedge model [m]. Green arrow: line of intersection (B) Swedge model seen normal to the slope [m] (C) Point cloud model of the in-situ wedge. red line: interpreted toe line, red dashed line: back scarp, red filling: SS sliding plane, yellow line: flank, yellow filling: J1 sliding plane, green line: line of intersection of wedge.*

4.18.2 Discontinuity strength

Input parameters for discontinuity strength are presented in *table 4.18.*

Table 4.18 *Input parameters for joint strength for the probabilistic stability analysis in Swedge. [1]In model 1B cohesion is set to c=0. [2]Parameter values defined after estimates from Barton (1973). [3]Assumed probability distribution due to low data concentration.*

Rock mass, J1 (model 1A-C)					**Value [°]**
Friction angle φ	[°]				56
Cohesion c	[MN/m^3]				2,5[1]
Coefficient of variability					0,02
Filling material, SS (model 1A-B)					**Value**
Friction angle	[°]				12[2]
Cohesion	[MN/m^3]				0[2]
Coefficient of variability					0,25
Barton-Bandis, SS (Model 1C)	**Mean**	**STD**	**Max**	**Min**	**Distribution**
JRC	6,4	3	16	2	Lognormal
JCS	167,2	26,8	250	120	Lognormal
Φr [°]	29	0,9	30	27,5	Normal[3]

4.18.3 Water pressure

Input parameters and probability distribution for water pressure are assigned according to the recommendations of Nilsen (2000), presented in *table 4.19*. Assigned probability distribution is plotted in *figure 4.40*.

Table 4.19 *Input parameters for water pressure for probabilistic stability analysis.*

Input parameters for water pressure	Value [%]
Mean	33,3
Maximum	100
Minimum	0

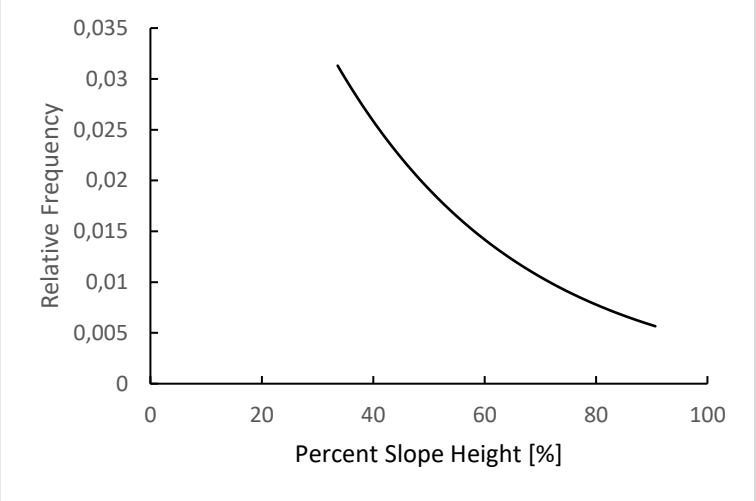

Figure 4.40 *Probability distribution for water pressure in terms of percent of slope height, as applied in the stability analysis.*

4.18.4 Seismic loading

Seismic coefficient was assigned according to ground acceleration a_{g40HZ} values derived from *figure 3.12* (Standard-Norge, 2014b). The probability distribution was assigned according to the recommendations of Nilsen (2000). Input parameters are presented in *table 4.20* and probability distribution is plotted in *figure 4.41.*

Table 4.20 *Input parameters for seismic loading for probabilistic stability analysis.*

Input parameters for seismic loading	Value
Seismic coefficient α_k	0,1
Mean	0,03
Maximum	0,1
Minimum	0

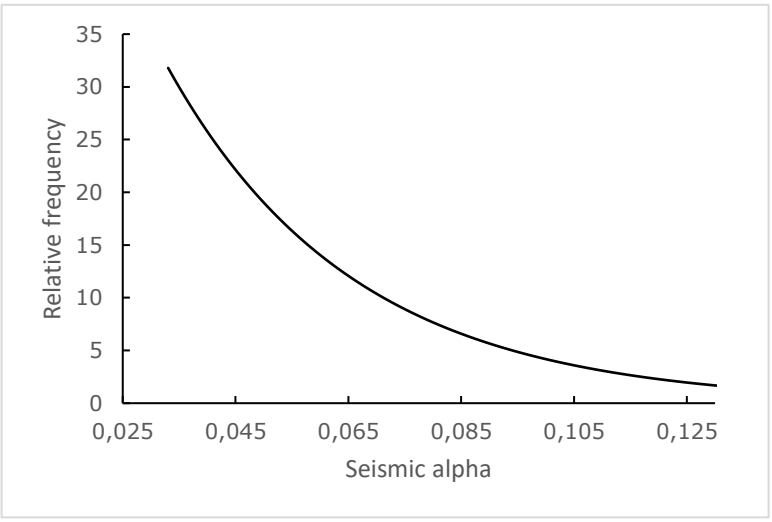

Figure 4.41 *Probability distribution for seismic coefficient α_k, as applied in the stability analysis.*

4.18.5 Factor of safety

Estimated probability of failure and factor of safety for models 1 A-C are presented in *table 4.21.* Probability distributions are illustrated in *figure 4.42*.

Table 4.21 *Output statistics for model 1 A-C.*

Model	Mean factor of safety	Probability of failure	STD	Probability distribution
1A	4,12	0	0,17	Normal
1B	0,57	0,86	0,09	Normal
1C	1,72	0,04	0,47	Lognormal

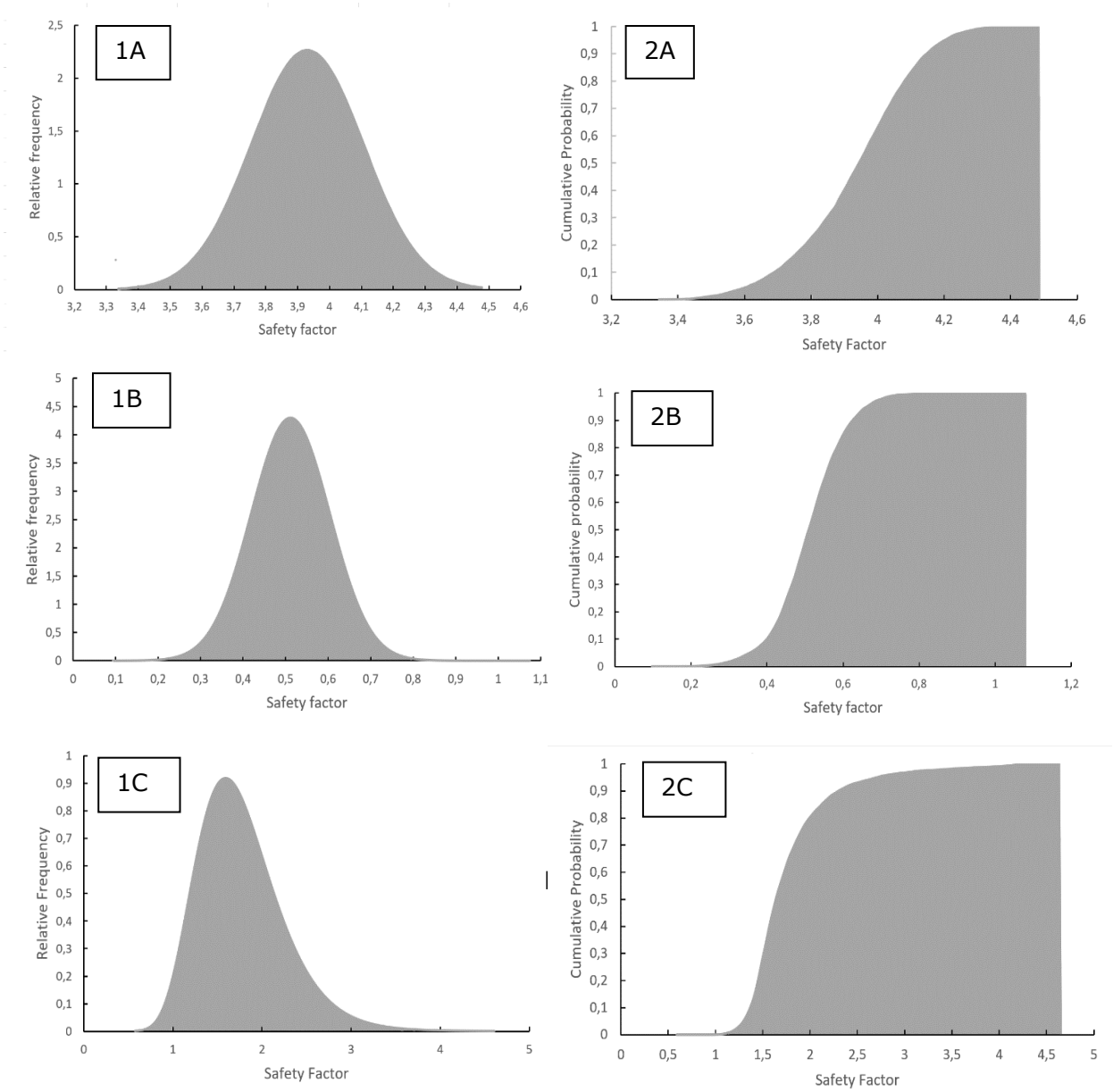

Figure 4.42 *1) Probability distribution for the factor of safety of models 1 A-C. 2) Cumulative probability distribution for the factor of safety of models 1 A-C.*

4.18.6 Sensitivity study

The sensitivity study investigates the effects of variability in joint strength, water pressure and seismic loading on the factor of safety of the wedge model. The credible variability ranges and resulting factor of safeties are hereunder presented.

Table 4.20 presents the influence of the joint strength parameters that were used for model 1A and 1B on FS and the defined boundary conditions. The boundary conditions for φ and c for the SS fracture plane was set according to values derived from Barton (1973). Variance of φ for discontinuity J1 is delimited according to the COV for the Hoek-Brown criterion. Minimum cohesion value for J1 was set as $c = 0$ to represent "worst case" conditions. Sensitivity plot is presented in *figure 4.43*. Mean values are defined according to model 1B.

Table 4.22 *Input parameter range for the sensitivity analysis for joint strength within model 1A and 1B and output min/max FS.[1]Range defined according to values from Barton (1973).*

Parameters			**FS**	
Variable	**Min**	**Max**	**Min**	**Max**
[1]SS friction angle	8,5	25	0,47	0,94
[1]SS Cohesion	0	0,27	0,57	1,25
J1 friction angle	50,4	61,6	0,52	0,63
J1 cohesion	0	2,5	0,57	4,12

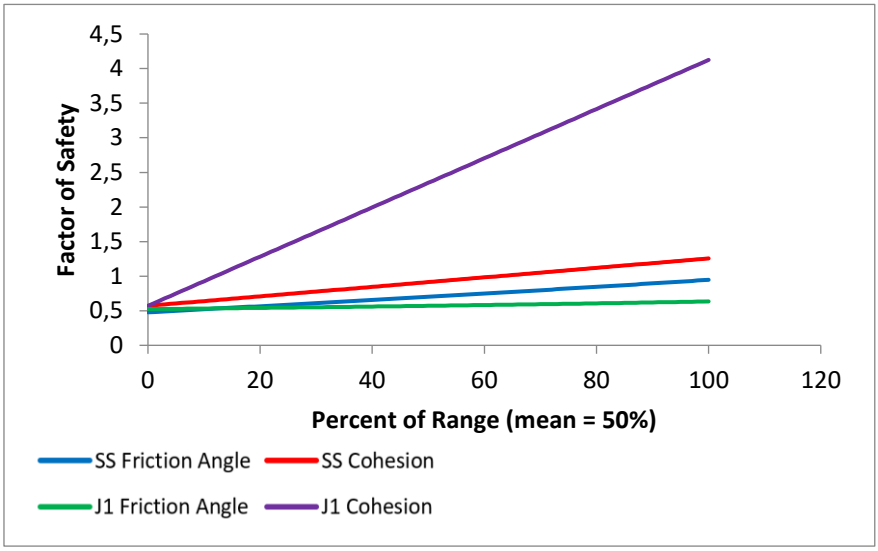

Figure 4.43 *Sensitivity plot presenting the effects of joint strength on FS according to the variability of input-parameters used in model 1A and 1B.*

Table 4.21 presents the influence of the shear strength parameters for bedding planes on FS within model 1C and the defined boundary conditions. Boundary conditions are set according to minimum and maximum values from field estimates (*table 4.14*). Sensitivity plot is presented in *figure 4.44*.

Table 4.23 *Input parameter range for the sensitivity analysis for joint strength of SS, as used in model 1C and output FS.*

Parameters			FS	
Variable	**Min**	**Max**	**Min**	**Max**
JRC	3	16	1,35	3,98
JCS	120	250	1,67	1,78
Φ_r	27,5	30	1,64	1,77

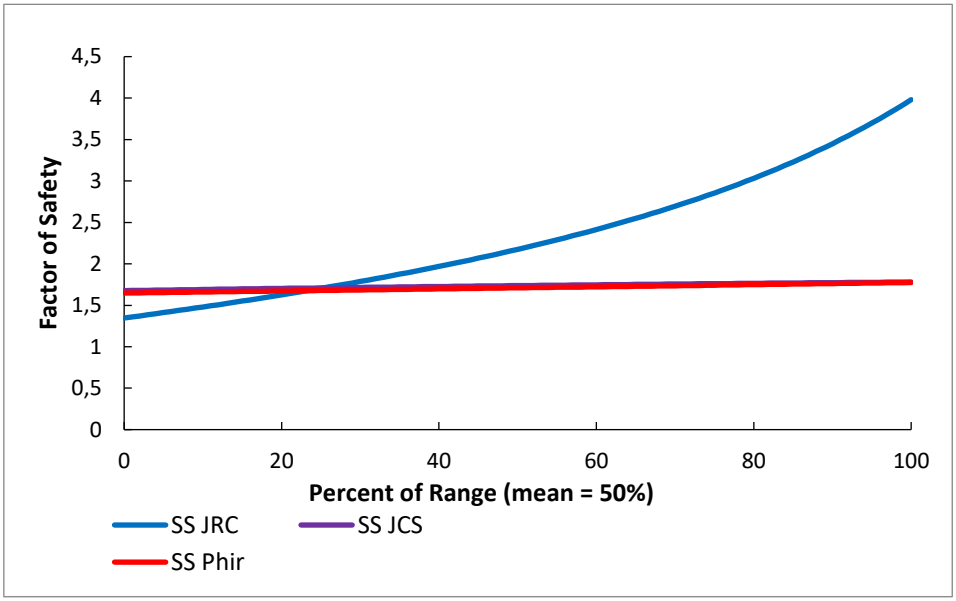

Figure 4.44 *Sensitivity plot presenting the effects of the SS joint strength parameters on FS according to the variability of input parameters used in model 1C.*

Lastly, *table 4.22* presents the effects of water pressure and seismic loading on the FS within model 1C. Boundary conditions are set according to the maximum and minimum water pressure and seismic coefficient used in the probabilistic models (*table 4.19-4.20*). Sensitivity plot is presented in *figure 4.45*.

Table 4.24 *Input parameter range for the sensitivity analysis for joint water pressure and seismic loading with joint strength parameters according to model 1C, and output FS.*

Parameters			FS	
Variable	**Min**	**Max**	**Max**	**Min**
Percent water filled	0	100	1,72	1,28
Seismic coefficient	0	0,1	1,84	1,5

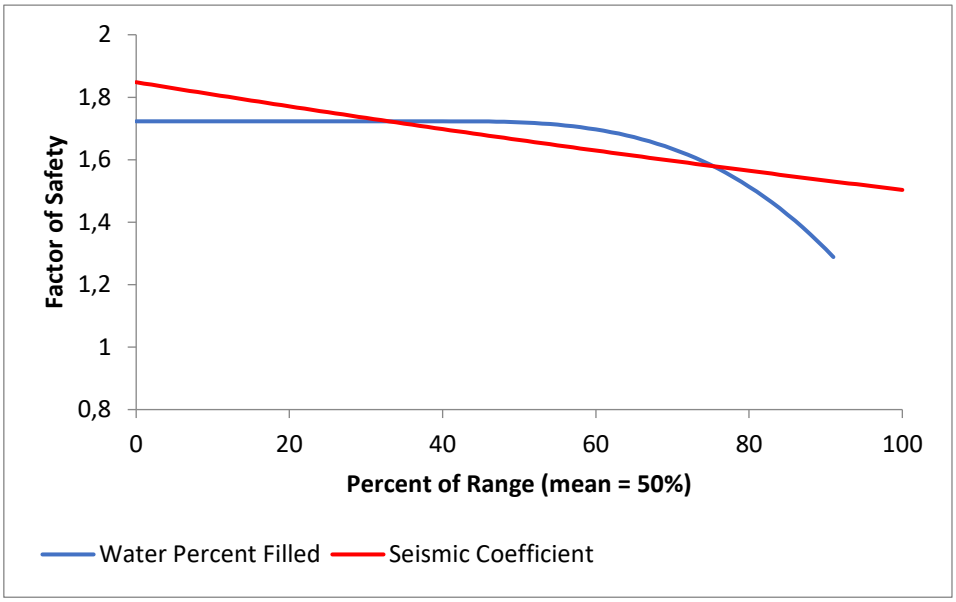

Figure 4.45 *Sensitivity plot presenting the effects of water pressure and seismic loading on FS with joint strength parameters according to model 1C.*

5 Discussion

5.1 Structural measurements on point cloud models

Remote structural measurements were conducted on point cloud models in CloudCompare to accommodate for unreachable areas where field observations suggested deviation from the structural dataset. Two remote structural datasets were constructed to determine the structural composition of the KV domain, one created using the Compass method and the other with the Coltop3D method (*appendix C*). Additionally, structural measurements were conducted to determine the prevalence of J4 within the SV domain (*figure 4.13)*. Although not recognized as statistically significant within the field dataset (pole concentration <4%), J4 was determined as both prevalent and persistent on SW facing slopes within the SV domain.

Furthermore, the remote structural datasets constructed for the KV domain was compared to structural measurements conducted along the Svelgsegga ridgeline. It is clear that the dip direction of discontinuities in the two remote datasets coincide well to the field dataset (mean deviance of ±6°). On moderately dipping discontinuities the dip match, although for the sub-vertical joint sets the remote datasets report on average 17° lower mean dip than the field dataset (*figure 4.12*). The reported discrepancy likely relates to the low point resolution on steep slopes within the point cloud models. As the models are ALS based, the steep incidence angle of the scan in relation to sub-vertical slopes limits the amount of observation points. This effect is referred to as orientation bias by Jaboyedoff et al. (2012). As a consequence of scale bias, the persistence of many steep discontinuity surfaces are smaller than the point spacing, referred to as scale bias (Sturzenegger and Stead, 2009, Lato et al., 2009). As pointed out by Jaboyedoff et al. (2012) this effect is especially important to consider when assessing the pole concentration in stereonet derived from automatic procedures (as the Colotop3D method), as "invisible" surfaces are not registered.

It was expected that the compass method would alleviate some of the bias effects, as the user has a higher degree of control over measurement points. Although, low variance in mean joint set orientation (mean deviance of ±3°) between the two methods indicate that this is not the case. This similarity in orientation displayed between the two methodologies is in of itself an interesting result, as it indicates the equal viability of the lesser acknowledged compass method. Because the discrepancy in dip between the remote and field derived datasets is expected to relate to source of error within the point cloud model, it was decided to define the structures of the KV domain according to the field data.

5.2 Spatial distribution of structures

The regional structural map (*appendix A*) indicates a study-area wide consistency in structural inventory. Bedding planes, bedding parallel minor fault zones and the four defined joint sets account for the total structural composition of the investigated area (*table 4.4*). Especially consistent is the orientation and expression of the bedding planes, displaying a small spatial variance (±7°). Field observations of bedding parallel minor fault zones were contained to the rock quarry located west on the Hennøy peninsula.

Øvstedal (1971) report the presence of similarly described weakness zones near Svelgen village. It is therefore assumed that minor fault zones are at least present within the eastern part of the study area, expressed as thicker bedding parallel layers in the rock mass (*figure 5.1*).

Spatial variance in orientation and prevalence of discontinuities is mostly contained to joint set 1 and 4. Ranked as statistically significant within all remaining structural domains, discontinuity J1 score a statistically insignificant regional pole concentration (<4%) within the HØ domain. The structure was neither recognized by further remote surveying on point cloud and was therefore excluded from the regional dataset in the kinematic analysis. Measurements conducted on J1 discontinuities within the HØ and KV domain additionally indicate a lower regional persistence (3-30 m) when compared to the SV and KV domains (5-500 m) (*table 4.5*). The structure thus appear less developed within the western part of the study area.

Variance is likewise displayed in the dip and persistence of joint set 4. Mapped J4 surfaces on point cloud within the SV and KV domains have persistence upwards of ~85 m with mean regional dip 52°. Field measurements on the persistence and dip of J4 within the HØ and TV are comparatively lower with persistence 3-30 m and dip 30°, falling below the rock mass friction angle (31°).

As the area coverage of high-resolution point cloud models was restricted to the southern part of the Hennøy peninsula, the extent of structural measurements was confined to the field area and the KV domain. Uncertainty is therefore related to the spatial variance in structures on the northern parts of the peninsula. This has to be considered when assessing further analysis related to the northern part of the peninsula.

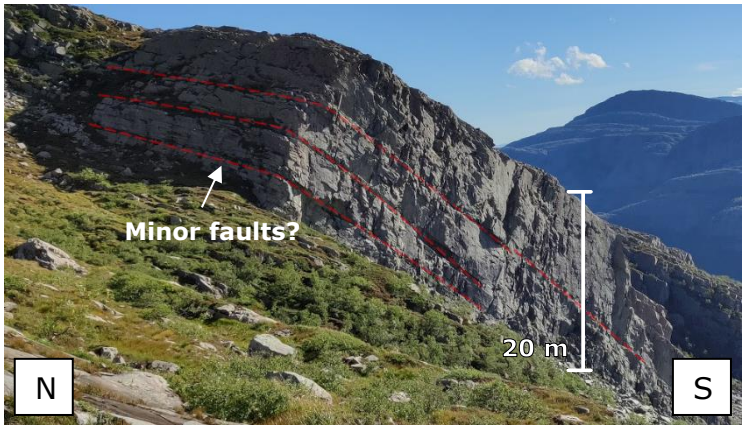

Figure 5.1 *Highly persistent bedding planes assumed to be the expression of bedding parallel minor faults within the SV domain.*

5.3 Spatial distribution of rock slope failure deposits

In total 30 rock slope failure events exceeding 10.000 m^3 are identified in the landslide inventory (*table 4.2*). Of the documented events, 11 exceed 100.000 m^3, corresponding to a density concentration of 0,3 rock-slope-collapses/km^2 and 0,2 rock-avalanches/km^2. From the landslide inventory map (*figure 4.4*) it is evident that rock slope failures exceeding 10.000 m^3 are clustered within the SV domain. The domain has a regional density concentration of 1,5 rock-slope-collapses/km^2 and 0,9 rock-avalanches/km^2. The distinction between rock slope collapse- (10.000-100.000 m^3) and rock avalanche

(>100.000 m^3) deposits and slide scars were made on the basis of volume estimations on rock slope scar geometry and corresponding failure deposits. In the case of 40% of the deposits the exact volume could not be defined due to being partially submerged within the Svelgsvatnet lake.

Rockfall deposits cover 8% of the total study area. Deposits are mostly concentrated on steep slopes around the edge of the peninsula and on the NW and SE aspects of the Svelgsegga ridgeline (*figure 4.4*). The SV domain has an apparent low abundance of rockfall deposits within the SV domain. This likely relates to the large abundance of rock slope failure deposits on SE-facing slopes. Overlapping of rockfall deposits and rock avalanche/rocks slope collapse deposits result in a the underrepresentation of the comparatively smaller rockfall deposits. A similar underrepresentation is evident within the HØ domain due to rockfall deposits fanning into the fjord.

5.4 Topographic conditions

Characterization of the topographic conditions was performed according to local relief, slope angle and slope angle. Distribution of these three parameters within mapped slide scars was assessed by overlapping the regional local relief and slope angle maps (*figure 4.15 A and B*) with the area extent of cataloged slide scars (*figure 4.3*). The conditioning of slope aspect is further discussed in context of the morpho-structural setting (*section 5.5*). A similar methodology was used by Pedrazzini et al. (2016) for assessing the topographical conditioning on the distribution and abundance of gravitational slope deformation.

The topography of the Hennøy peninsula is mostly of low local relief with 90% of the study area displaying a local relief below 300 m (*figure 4.17 B*). The height is normally distributed with a relatively large spread (mean 233 m and STD 75). Slide scars are associated with a comparatively low relief, and with an equal distribution as the study area mean (mean 229 m and STD 85,7). This similarity in distribution suggests that local relief is unimportant for the distribution of failures exceeding 10.000 m^3.

Steep slopes exceeding 31° (rock mass friction angle) are largely concentrated around the edge of the peninsula and on the NW-aspect of the Svelgseggen ridgeline, forming a plateau in the middle with mostly shallow dipping terrain (>15°) (*figure 4.15 B*). Slope angle is lognormally distributed within the study area (19° and std 15) with 90% of the terrain dipping shallower than 40° (*figure 4.17A*). The distribution within slide scars is considerable different, with 90% of slide scars concentrated on slopes with dip in the range 29-47° (mean 38° and std 9). This distribution closely resemble the mean dip of the bedding within the SV domain (mean 35° and std 10). Bedding thus represent the large majority of basal planes of documented relict rock slope failure exceeding 10.000 m^3. Approximately 10% of the total slide scar area belong to slopes steeper than 47°. This surface area is expectedly belonging to rupture surfaces not related to the bedding.

Topographic conditioning on the distribution of rockfalls was furthermore investigated by overlapping the area extent of rockfall deposits (*figure 4.4*) with the regional slope aspect map (*figure 4.15C*). The distribution of slope aspect within rockfall deposits was compared to the study area wide distribution of slope aspect. As indicated in *figure 4.18 A*, the Hennøy peninsula display an abundance of N and S oriented slopes (*figure 4.18 A*). Rockfall deposits hold a similar NW and S dominated distribution, although there exist a clear discrepancy in the relative abundance (*figure 4.18*). Rockfall deposits are 18,6 % more abundant on S-facing slopes when compared to the study area distribution of slope

aspect. Similarly, deposits on NW slope aspects are 8,9 % more abundant. It is therefore apparent that slope aspect conditions the distribution of rockfall deposits.

Some of the aspect related conditioning is likely explained by the uneven distribution of steep slopes (exceeding the rock mass friction angle) within the study area. Due to the E-W elongate shape of the peninsula, the majority of steep slopes have N and S orientations (*figure 4.15 B)*. This is likewise indicated in *figure 4.20*, revealing that ortoclinal and anaclinal slope aspects holds a larger abundance of slopes exceeding 45°, when compared to cataclinal slope aspects. A low abundance of steep slopes naturally limits the amount of potential source areas for rockfalls, likely explaining the low abundance of deposits on WSW and ENE oriented slopes. This is naturally not accounted for in *figure 4.18 A,* as it only display the slope aspect within deposits.

5.5 Morpho-structural conditioning

The morpho-structural map was constructed to illustrate how the interaction between the bedding and the topography conditions the distribution and abundance of rock slope failure (*figure 4.19)*. Due to the study area wide consistency in orientation of bedding planes it was decided to define a single global orientation (122/33) for the morpho-structural map. This was motivated by simplifying the methodology presented by Santangelo et al. (2015).

Spatial statistical analysis of the morpho-structural map (*figure 4.19*) reveals that the ortoclinal domain occupy the largest area, covering 41% of the study area. This is largely to be expected in most mature landscapes, as the two orthoclinal quadrants encompass 50% of the total angular range (0°-360°) (Santangelo et al., 2015). Its abundance is reflected on the northern and southern slope aspects of the Hennøy peninsula. Cataclinal slopes represent the second most abundant domain, accounting for 30%. Under-dip slopes occupy the majority of the area, displaying a large abundance within the relatively flat interior of the peninsula. Cataclinal-dip slopes comparatively only constitute a small portion of the study area (4%) and is mostly concentrated on the SE slope aspect of the Svelgsegga ridgeline and some portions of the predominantly orthoclinal southern slopes of the Hennøy peninsula. The abundance of cataclinal over-dip slopes is very limited (<1%), mostly expressed as back-scarping in slide scars within the SV domain and some cliff bands within the HØ domain. Lastly, the anaclinal domain constitutes approximately the same area as the cataclinal domain (29%) and is most abundant on the NW fringe of the peninsula, including the TV domain and also within the KV domain.

To further assess the morpho-structural conditioning on rock slope failure, the morpho-structural map (*figure 4.19*) was overlapped with the landslide inventory map (*figure 4.4*), following a similar methodology as presented by Santangelo et al. (2015). Rock slope failures were classified according to magnitudes: rockfall (<10.00 m^3), (2) rock slope collapse (10.000-100.000 m^3) and rock avalanche (>100.000). The distribution of domains within the different failure magnitude deposits are presented in *figure 4.22*. If landslides were not conditioned by the local morpho-structural settings, the proportion of landslides in a specific morpho-structural domain would be the same or similar to the proportion of the same domain in the study area (Santangelo et al., 2015).

For rockfall deposits, the distribution of domains correlates well to the study-area wide distribution. Although, some discrepancies to the correlation are present within the plot. Cataclinal under dip-slopes (yellow dots) display a 17% lower abundance within rockfall deposits, compared to the study area total (black tots). Similarly, the ortoclinal domain (green dots) is 12% more abundant when compared to the study area total. The discrepancy on under-dip slopes is expected to related to the shallow, sub friction angle dip (<31°) of the domain. On ortoclinal slopes the discrepancy is likely linked to the aspect related conditioning of rockfall distribution, as discussed in section 5.4. The correlation in distributions thus imply that the morpho-structural setting does not condition the distribution of rockfall deposits.

For rock slope collapse and rock avalanche deposits the morpho-structural distribution does not correlate to the study area distribution. Discrepancy is expressed in the large relative over-abundance of deposits on dip slopes (~46%, brown dots) and under-abundance on anaclinal slopes (~29%, blue dots) when compared to the study area distribution. Somewhat unexpectedly, a large abundance of rock slope collapse and rock avalanche deposits rest on orthoclinal slopes (total of 45%). Although, as indicated in *figure 20* the abundance is largely related to slope aspect change from the source area to the run-out. This is furthermore supported by the large abundance of bedding orientated slope angles within slide scars (*figure 17 A)*, as discussed in section 5.4.

5.6 Structural conditioning

As stated in section 5.5, the morpho-structural setting plays an important role in the conditioning of rock slope collapse and rock avalanches. On the other hand, the large abundance of rockfall deposits on S and NW oriented slopes remain largely unexplained by the bedding planes. On this basis, rock slope stability can be categorized according to 1) bedding plane conditioned failure and 2) failures not conditioned by the bedding.

5.6.1 Bedding plane conditioned failure

Failure conditioned by bedding planes involves simple planar failure and wedge failure formed by the interaction of bedding discontinuities and the J1 discontinuity set. The sub-vertical orientation of the J1 discontinuity set (051/89) result in wedges sliding almost exclusively on the bedding. Joint set 1 is therefore acting more as a lateral release surface. In total 93% of the documented rock slope collapses and rock avalanches in the landslide inventory (*table 4.2*) are explained by sliding along the bedding.

Of the documented failure events, failures 1-11 (*table 4.2*) can be attributed to sliding along the intersection of the bedding and interconnected J1 discontinuities. Located on the SE-facing dip-slopes, the events follow more or less the same failure geometry. To the W, the wedges are released by sedimentary scarp slopes, oriented laterally to slightly oblique relative to the dip direction of the dip slope. Due to the dip-slope dominant orientation of the slope, daylighting of bedding planes is not feasible along most of the slope. In the case of failure 2 (*table 4.2*), the obliqueness of the pre-failure scarp slope allows for the wedge intersection to daylight in the slope. The structural conditions form a slender wedge geometry that intersects the top of the mountain and narrows downslope. Accordingly, the magnitude of the failure is structurally determined by the height of the bench in relation to the bedding plane *D* and the lateral placement of the J1 discontinuity structure (*figure 5.2*). The described failure mode can be characterizes as a

planar translational failure after the classification of Glastonbury and Fell (2010) (*figure 5.3 A*).

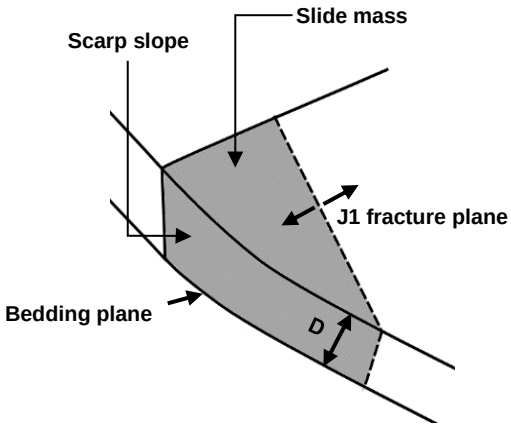

Figure 5.2 *Isometric view illustrating the structural control on the magnitude of bedding conditioned rock slope failure along the Svelgsegga ridgeline.*

In the case of failures 1 and 2-11 (*table 4.2*), the foot of the slope is covered by deposits, thus concealing the slide scar toe line (*figure 5.3 B*). It is therefore unclear whether the whether the wedge intersection line daylights in the scarp slope, illustrated in *figure 5.2*. Alternatively, daylighting can be explained by step fracturing, further described in section 5.9.

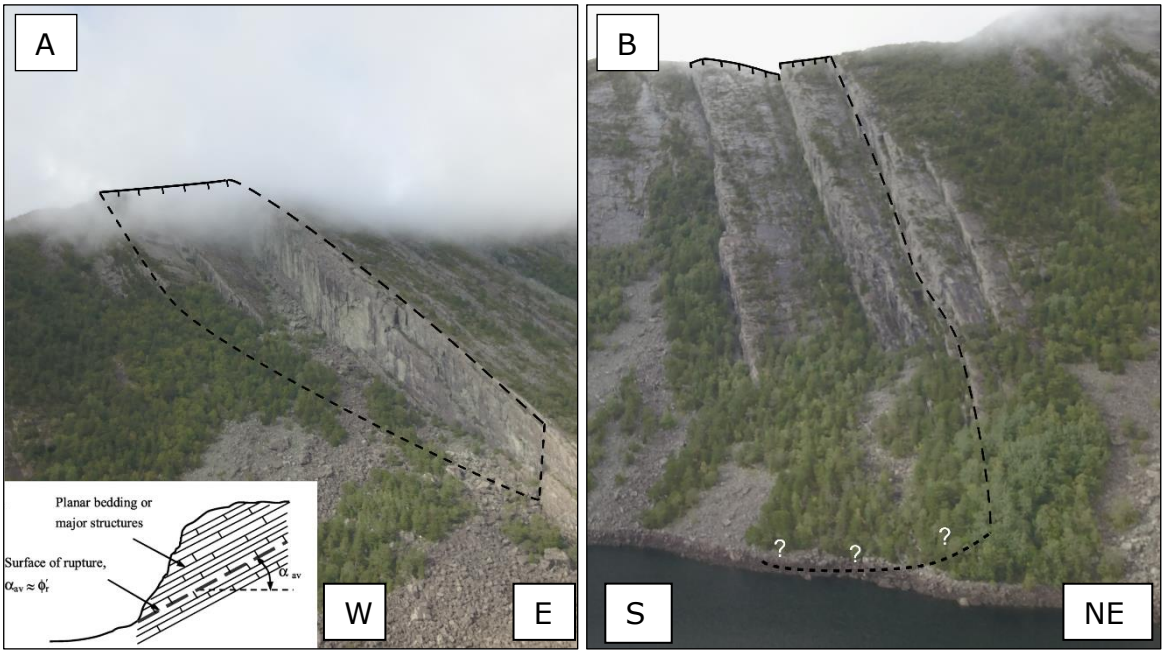

Figure 5.3 *(A) Overview photo of failure 2 (figure 4.5). Slide scar toe is defined within the scarp slope (dashed black line). Failure can thus be explained in terms of planar translational sliding according to the classification of Glastonbury and Fell (2010). (B) Overview photo of failure 4. Toe line is concealed within deposit or under the water line (dashed black line), attributing some uncertainty to the daylighting of the toe line*

In addition to the narrow wedge form documented in failures 1-11 (*table 4.2*), some slide scars are wider, more representative of planar failure. These failures are either released at both sides by J1 discontinuities, or to the W by the scarp slope. Back scarps are formed by the intersection of J1, J2 and J3 discontinuities (*figure 5.4*). Again, the

daylighting of the toe line of planar slides are concealed due to the large abundance of deposits at the foot of the slope. Daylighting might be explained by local steepening of the dip-slope down-slope, or step fracturing.

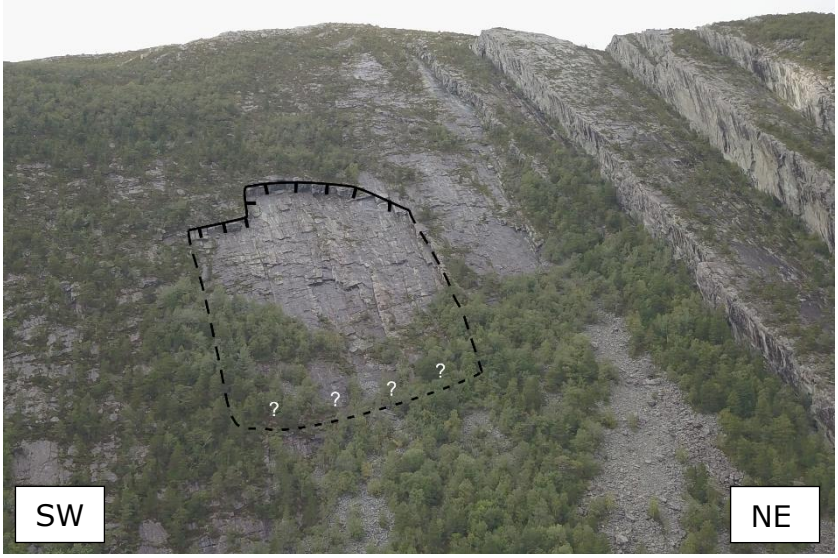

Figure 5.4 *Overview photo of failure 22 (figure 4.5). Slide scar resembles planar translational failure along the bedding plane, laterally delimited by J1 fracture planes.*

Planar failure is also indicated as kinematically feasible within cataclinal sections of the HØ domain, although the low regional prevalence of joint set J1 leaves blocks delimited by discontinuity joint sets J2 and J3. In comparison to the high persistence of joint set J1 (3-250 m), the J2 and J3 joint sets only have a persistence of 5-30 m. This persistence allows only for planar failures in the magnitude order of rockfalls.

5.6.2 Failure not conditioned by bedding planes

Failure not conditioned by bedding planes involves rock slope failures on ortoclinal and anaclinal slopes, where failure is not facilitated by sliding along the bedding plane.

Feasible failure modes for rock slope failure on the southwestern orthoclinal domain is presented by the kinematic analysis for the HØ domain (*figure 4.26*). Direct toppling is recognized as feasible from J2-J3 delimited blocks in sub-vertical cliff bands, with the bedding functioning as basal plane. The 0,8-1,2 m spacing and 3-30 m persistence of the joint sets creates tall and oblong blocks in the magnitude order of rockfalls, prevalent on S-facing slopes (*figure 4.10 D*).

The kinematic analysis for the TV, KV and NW-aspect of the SV domain all represent anaclinal slope aspects (*figure 4.24, 4.25 and 4.27*). Structural variability between the domains is as presented in section 5.2, and is mostly related to the prevalence of discontinuity J1 and the dip and persistence of discontinuity J4. Within the TV domain the shallow dip of discontinuity J4 (regional mean 303/27) restricts the feasibility of planar failure and wedge failure along the J1-J4 and J3-J4 intersection lines. Failure within the domain is therefore limited to direct toppling from J1-SS delimited blocks.

Within the SV and KV domains the comparatively steep inclination of joint set 4 (regional mean 301/59) allows for wedge failure along the J1-J4 and J3-J4 intersection lines. The large persistence of discontinuity set J4 allows for failures of magnitude order rock slope collapse. This is exemplified by failure 15 (*table 4.2*), delimited by a persistent J4 discontinuity surface and less persistent and interconnected J3 discontinuities. The sub-

vertical dip of the J3 discontinuity (regional mean 352/86) result in sliding occurring almost entirely on the J4 surface (*figure 5.5*).

Within the KV domain, wedge failure is facilitated by the J1-J4 intersection line. Meter scale slide scars formed by the J1-J4 intersection is prevalent along the NW dipping aspect of the Svelgsegga ridgeline (*Figure 4.11A*). Although not investigated within the kinematic analysis, the favorable relationship of the J1-J4 intersection line is expected to explain the large abundance of rockfall deposits on the NW aspect of the Hennøy peninsula (*figure 4.18*).

Figure 5.5 *Overview photo of failure 15. The highly persistent J4 discontinuity plane facilitate "steinskred" magnitude wedge failure along the J3-J4 intersection line.*

5.7 Shear strength models

5.7.1 Rock strength parameters

Rock mechanical testing in the laboratory was conducted to determine rock mass strength properties and Hoek-Brown failure criterion for incorporation in further stability assessment. The tested rock sample was collected in the deposit of failure 2 (*figure 4.2*). Identified as fine-grained sandstone, the sample represents the most abundant lithology within the field area. As described in section 4.1 there exist some regional variance in lithology, indicating that variability in rock strength may be larger than indicated by lab results.

In the process of preparing cores for uniaxial and triaxial compressive testing it became evident that the limited size of the rock sample collected in the field would limit the amount of test-cores. It was therefore decided to reduce the diameter from the planned 50 mm to 35 mm to increase the number of cores. As presented in section 3.7.2, sample size reduction may affect the peak strength of the sample (UCS). According to equation 3.3, UCS can be adjusted to correct for sample size effects. However, it is by Hawkins (1998) suggested that this correlation does not apply for samples of diameter lesser than 54 mm. Based on these facts no adjustment of the UCS was conducted.

The limitation in the number of cores resulted in only two samples being tested uniaxially. According to Brown (1980) at least 5 samples should be tested to get a sufficiently large dataset. The two UCS tests that were conducted displayed similar peak strength (*table 4.8*) and fracture characteristic (*figure 4.33*). It was therefore prioritized to use the remaining cores in triaxial testing. Due to the stable ductile zone displayed in uniaxial testing it was decided to conduct triaxial testing in multiple steps to maximize the data output. The confinement pressures applied in the triaxial testing (*table 3.7*) were based on values applied by Tønset (2019).

It was chosen to fit the peak strength data from the uniaxial and triaxial testing to a Hoek-Brown regression curve (*figure 4.34*). The fit was estimated to COV=0,02, indicating a very close correlation according to the definition of Hoek (2000). To fit the input parameter requirements of Swedge the Hoek-Brown criterion was adapted to the Mohr-Coulomb failure criterion. As pointed out by Hammah et al. (2005) this conversion is sensitive to the predefined normal stress that defines the tangent of the Mohr-Colomb line (*figure 3.11*). Due to the simple methodology that was used to estimate the normal stress value, some uncertainty must be attributed the instantaneous cohesion and friction angle used in the probabilistic stability analysis.

When using the Mohr-Coulomb failure criterion in further stability analysis it is important to consider the anisotropy that bedding planes and minor fault zones apply to the rock mass. As described in section 2.3.2 the Hoek-Brown failure criterion assumes isotropic rock and rock mass behavior (Hoek, 2000). As planar and wedge failure is largely facilitated by sliding on bedding planes, the Hoek-Brown criterion cannot be taken as a good fit for describing the total rock mass strength. Thus in the stability assessments the strength of the bedding fracture surface was defined according to the shear strength properties of the bedding plane and minor fault filling material.

The second wedge delimitation is largely dependent on the degree of interconnection of highly persistent J1 discontinuities. When modelling the strength of the fracture plane it is therefore important to account for the cohesion of the rock mass. Shear strength of the J1 fracture surface was therefore defined by the lab derived Hoek-Brown criterion. It is therefore assumed that the anisotropy related to bedding planes does not affect the shear strength of the J1 delimited structure.

5.7.2 Discontinuity strength parameters

Filling material on bedding planes and bedding parallel minor faults display a large variation in thickness (1 mm-37 cm) (*figure 4.9*). Accounting for the amplitude of bedding planes (10 mm – 39 mm), the variation represent a fracture geometry ranging from full- to no rock wall contact along bedding planes. As outlined by Barton (1973), filling material thickness is important for the shear strength of filled discontinuities in rock. Increased filling material thickness in relation to plane roughness induce a proportional reduction in shear strength along the discontinuity (Goodman, 1970). When the filling material thickness exceeds the amplitude of rock asperities, strength is mostly determined by the mechanical properties of the filling material (Barton, 1973). The variability in shear strength represented by filling material thickness was accounted for in further stability analysis by modelling bedding shear strength according to both: 1) full rock wall contact and 2) no rock wall contact.

Full rock contact along the bedding was represented by the Barton-Bandis failure criterion for bedding planes, presented in section 4.17. Input parameters for the criterion

was derived from field estimates of JRC, JCS and φ_r. Measurements were conducted on nine bedding planes within the field area. Some inaccuracy can be attributed to the estimation of JRC values. In similar studies (Kveldsvik et al., 2008) JRC estimates are derived from readings in four directions. Estimates conducted on the Hennøy peninsula were only conducted in strike parallel and strike normal lengths. As the variance in amplitude in the measured directions was quite small (~5 mm), the two datasets were combined to achieve a greater data concentration for the JRC estimate. This was similarly done by Kveldsvik et al. (2008).

Variability in surface wetness throughout the field work also leads to some inaccuracy in the estimation of φ_r (r value) and JCS. Conservative estimates of r and JCS should be conducted on wet surfaces as this generally result in lower Schmidt rebound values. As some estimates were conducted on dry surfaces the estimate JCS and φ_r include estimates conducted on both wet and dry surfaces. When comparing the mean JCS values of wet and dry surfaces it was found that wet surfaces scored a mean UCS of 15 MPa lower than on dry surfaces.

To quantify the shear strength of minor fault zones, gouge material was collected in the field to be mechanically and mineralogically tested in the lab. Due to restricted lab access during the writing of the thesis, testing of the material was not carried out. There is thus a large uncertainty related to the material composition of bedding parallel minor fault zones. In further stability analysis the shear strength of the filling material was simply defined according to the shear strength estimates of filling materials presented by Barton (1973) (*figure 2.10*). After a visual examination of the gouge material gathered in the field, the shear strength was simply assigned according to filling material class "clays". To account for the large uncertainty related to the filling material, the strength parameters was assigned an uncertainty of COV=0,25. In the sensitivity study the range was expanded to represent a more conservative range in shear strenght from material class "bentonite" to "clay shale".

5.8 Probabilistic stability analysis

The stability conditions of rock slope failures on the Hennøy peninsula was investigated by conducting a probabilistic stability analysis in line with Eurocode guidelines (Nilsen, 2000, Nilsen et al., 2011, Standard-Norge, 2014a, Standard-Norge, 2014b). A wedge model was constructed in SWedge based on the dimensions of the slide scar of failure 2 (*figure 4.39*). The failure mode is thus defined as planar translational sliding. Orientation and area of the bedding surface and J1 fracture plane was defined according to structural measurements on point cloud models in CloudCompare. Orientation of the slope was furthermore tweaked to correlate the volume and fracture plane area of the wedge model to the in-situ wedge (*table 4.17, figure 4.39*). Because the geometry of the in-situ wedge is known, the Swedge wedge geometry was defined as constant.

The stability analysis put an emphasis on assessing the control of rock mass strength and discontinuity strength on wedge stability. To account for the different probable discontinuity strength conditions discussed in section 5.7, three individual models were constructed according to the following assumptions:

1) No rock wall contact on the bedding plane and shear strength of discontinuity J1 according to rock mass strength.
2) No rock wall contact on the bedding plane and shear strength of discontinuity J1 according to rock mass strength, assuming a fully fractured surface.

3) Full rock wall contact on discontinuity SS and shear strength of discontinuity J1 according to rock mass strength, assuming a fully fractured surface.

To simulate a fully fractured J1 fracture surface the cohesion was set to *c*=0, assuming that displacement along the plane is facilitated at a constant residual stress value (Wyllie and Mah, 2004)

Out of the three models produced, model 1B is the only unstable wedge model with mean factor of safety FS=0,57 and probability of failure PF=0,86 (table 4.21). Both model 1A and 1C have probability of failure of PF=0. Of the two stable models, model 1A has the largest factor of safety with mean FS=4,12. Model 1C have mean FS=1,72.

The difference displayed in stability between model 1A and 1C clearly indicates the importance in the development of the J1 fracture plane. In the sensitivity study (table 4.22), the cohesion of discontinuity J1 display the biggest range in factor of safety of all joint strength parameters (FS=0,57-4,12). The range in cohesion indicates the important stabilizing factor of intact rock bridges along the failure plane. As described by Terzaghi (1962) an effective cohesion along the failure plane would simulate the increased resistance to shear failure provided by intact rock bridges.

The importance of the fracturing along the J1 fracture plane is further emphasized by the excessive length and relative thickness of the wedge geometry. According to Glastonbury and Fell (2010) a high slenderness ratio (*L/W*) indicate a long and narrow landslide mass, implying that lateral margins exert a great influence on total rupture surface length. A likewise large relative thickness (*D/W*) would reflect a large area acting on the lateral margin. Elongate and thick slide masses are therefore expected to display a greater sensitivity to the strength of lateral margins (*figure 5.6*). The friction angle of the J1 fracture surface is recognized as of lesser importance for the wedge stability (FS=0,52-0,63) in the sensitivity study (*table 4.20)*. This can be explained by the steep inclination of J1 (051/89±21). Sliding is therefore occurring almost entirely on the bedding with the J1 structure acting as a release surface. In this type of wedge, the shear strength of the release surface will be of lesser importance for stability (Wyllie and Mah, 2004).

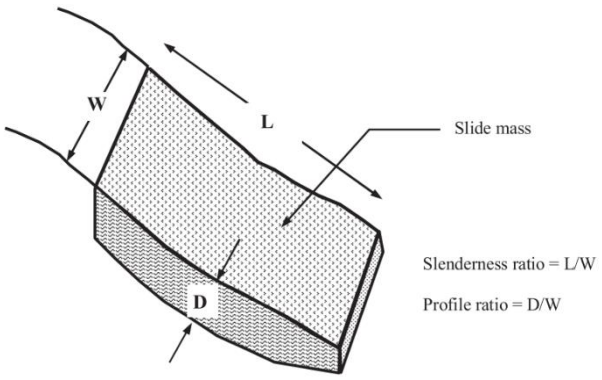

Figure 5.6 Isometric view displaying important dimensions in assessing lateral margin influence (Glastonbury and Fell, 2010).

The relative stability of model 1C in comparison to model 1B highlights the importance of filling material on the bedding plane in controlling wedge stability (*table 4.21)*. This is further emphasized by the sensitivity study for the Barton-Bandis failure criterion for bedding planes (*table 4.23*). None of the parameters within the sensitivity plot produce an unstable wedge within the credible range (FS<1). Of all the discontinuity strength

parameters, JRC is most influential on the stability of the wedge (FS=1,42-4,06). As presented by Goodman (1970) an increased filling material thickness in relation to the joint roughness will result in a lowering of the shear strength. This is naturally reflected by a reduction in the factor of safety of the model. A threshold filling material thickness in relation to the roughness of the bedding plane must therefore be met for the wedge to be unstable (FS<1). Adjustments in strength properties of the filling material additionally reflect a large variation in factor of safety. Cohesion represent a range of: FS=0,57-1,25 (*table 4.23*). Defining the exact filling material strength is therefore important in determining the stability of the fracture delimited blocks presented in section 4.4.2.

Furthermore, the stable condition of model 1C implies that neither high water pressure or seismic load is sufficient to condition failure for wedges with full rock wall contact. This is further implied by the sensitivity study for water filling and seismic load (*table 4.24*), where minimum factor of safety with maximum water pressure is calculated to FS=1,28 and FS=1,5 for seismic load. Although insufficient for triggering at full rock wall contact, both factors could represent important triggering mechanisms for wedges closer to equilibrium stability conditions (FS=1).

As indicated by the sensitivity study for , water pressure results in a substantial reduction in factor of safety when filling height exceeds 75% (FS=1,72-1,28). At lower filling heights the factor of safety remains unchanged. Although representing a large reduction in FS at higher values, it is as made clear by Nilsen (2011) that the model that is used in the stability modelling is rather unrealistic, as water normally drain out along cracks and fissures down-slope. This considerably reduce the resultant water pressure (*figure 3.12 B*). The placement of mapped slide scars near the top of ridges additionally reflect a very limited drainage basin for the accumulation of water on the fracture surface. This will further limit the potential for large joint water filling heights. It is therefore unlikely that increased joint water pressure represent an important triggering mechanism.

Topographic effects also affect the acceleration load of earthquakes. The interaction of incoming seismic waves with steep slopes in areas of strong topographic relief is documented to result in amplification of ground motion (Geli et al., 1988). This amplifying effect result in larger seismic amplitudes toward ridge crests (Boore, 1972, Boore, 1973, Bouchon, 1973, Wong and Jennings, 1975). It is therefore likely that the potential for seismic load is larger than determined by the probability distribution used in the wedge model (*figure 4.24*). It is important to note that the estimate reflects the probability and seismic load of earthquakes in the present day (Standard-Norge, 2014a). Relative dating of rock slope failures report evidence of high tectonic activity at the end of the Pleistocene and into the Holocene in Scandinavia (Mörner, 1996, Bungum et al., 2005). This would further suggest that the documented relict landslides along the Svelgsegga ridgeline (*figure 4.5*) would have been subject to more frequent and larger seismic load in this time interval.

5.9 Fracture delimited blocks

In section 4.4.2, three fracture delimited blocks exceeding a volume of 100.000 m^3 were defined along the Svelgseggen ridgeline (*figure 4.6*). Placement of delimiting structures was determined according to field mapping, fracture mapping on point cloud models and observations on DEM-model.

Block 1A and 3A-B are located along the Svelgsegga ridgeline, dipping towards the Svelgsvatnet lake. Block 2 is located 500 m to the SE along a lower elevation ridgeline.

All three blocks are delimited to the E by NW-SE striking fractures and released to the W by a NW-SE trending scarp slope (*figure 4.6*). The development of fractures vary between the blocks. Block 2 display the most well developed flank with fracturing occurring along almost the entire length of the block. Block 1A and 3A-B display less developed flanks, with fracturing limited to the top of the slope. Back scarp of the blocks are set in the top of the ridge. The placement is supported by the presence of NW-SE striking fractures intersecting the top of the ridgeline. Lastly, the toe line of block 1A is set within the NW-SE trending sedimentary scarp slope. Block 2 and 3A-B have their toe lines set within the back scarp of slide scars that occur at the toe of the slope, forming a natural lower delimitation. Due to the dip-slope orientation of the slope it is clear that deformation of the entire rock mass of the blocks cannot be explained by sliding along a single bedding plane. This is clearly indicated in the structural profiles presented in *figure 4.28-4.30*. Deformation must therefore be facilitated by a more complex failure mechanism, where the rupture surface utilize more than one surface type in order to daylight (compound failure). The process of step fracturing may explain the deformation. This mechanism involve the rupture propagation through the rock mass by combining both pre-existing discontinuities (in this case bedding) and new low-angle fractures formed by the breakage of rock bridges (Stead and Eberhardt, 2013).

Similar to the model for foliation controlled rear rupture presented by Vick et al. (2020) it is possible that the rupture surface follow the bedding at the rear and step fractures at the base (*figure 5.7A*). Fracture propagation can then be explained by an active-passive wedge model, where loading from the active part of the wedge (material at the head under tension) drives the passive wedge (material at the toe, under compression) (*figure 5.7B*).

Compound failure mechanisms normally display both tensile damage at the head and compressive damage at the toe. The general absence of internal deformation within the fracture delimited blocks would argue against the presence of a compound fracture plane. Low internal deformation is more characteristic for planar translational failure (Glastonbury and Fell, 2010). InSAR data for all three blocks indicate mean velocity values within the negligible range (<2,5 mm a^{-1}) (*Appendix E*). The limited display of internal deformation can alternatively be explained by limited deformation.

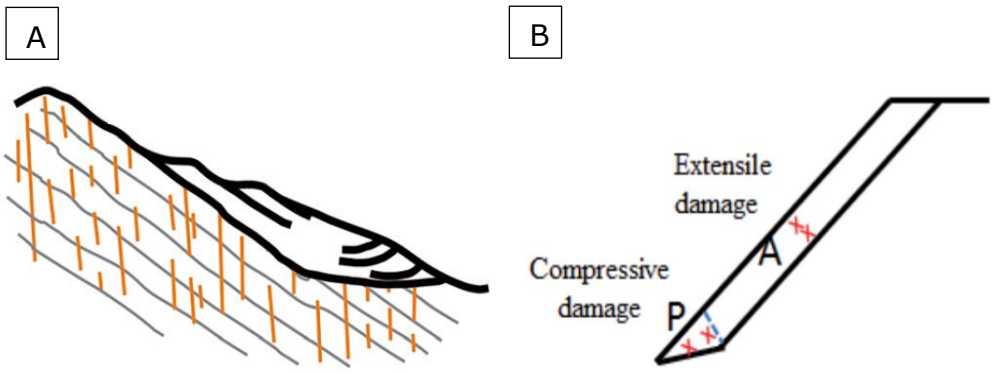

Figure 5.7 *(A) Schematic illustrating bedding plane rear rupture controlled failure. The orientation of the bedding allows kinematically for bedding-parallel sliding at the head of the slope. Modified after Vick et al. (2020). (B) Schematic of an active-passive footwall failure surface morphology, displaying tensile deformation at the head and compression damage in the toe (Stead and Eberhardt, 2013).*

Conclusion

The main goal of this study has been to investigate the structural and lithological controls for rock slope failures on the Hennøy peninsula and how the geometrical interaction with topographic factors influence the size, mode, and distribution of failure.

Structural analysis reveals a study-area wide consistency in the spatial distribution of discontinuities. The total structural composition of the Hennøy peninsula can be attributed to five discontinuity sets (dipdir/dip): SS (122/33), J1 (033/83), J2 (292/78), J3 (354/86), J4 (303/35). Parallel to the bedding occur minor fault zones that transect the rock mass.

Structural and topographical controls on the spatial distribution and abundance of rock slope failure on the Hennøy peninsula were investigating using a multidisciplinary approach. This involved comparing the spatial distribution of the landslide inventory map with topographic and structural characteristics of the adjacent rock slopes. A special emphasis was placed on the morpho-structural conditioning related to the regional prevalence and persistence of bedding planes and bedding parallel minor faults.

The detailed landslide inventory map revealed the presence of a minimum of 30 rock slope failures exceeding 10.000 m^3 since last glacial maximum. Events are not uniformly distributed, revealing an apparent clustering on predominantly cataclinal dip-slopes within the eastern portion of the study area. Orientation of the bedding is the strongest conditioning factor for failures exceeding 10.000 m^3. A total of 93% of documented events failed along the bedding surface. Interpretation of slide scar morphology and spatial variability in structures suggests that clustering of failures exceeding 10.000 m^3 is also conditioned by the presence of a highly persistent and laterally oriented J1 structure. The bedding-joint intersection form long, wedge-shaped slide scars, involving most relict rock slope failures exceeding 10.000 m^2, indicating simple planar translational sliding.

Rockfalls are abundant on the Hennøy peninsula, covering more than 8% of the total study area. Deposits are not uniformly distributed, displaying an apparent clustering on southern and northwestern slope aspects. The distribution of rockfalls correlate to the distribution of steep slopes within the study area. Kinematic analysis further relates rockfalls on these slope aspects to favorable joint geometries. On southern slope aspects the kinematic feasibility tests indicate that rockfalls are mostly related to joint set delimited direct toppling from steep cliff bands. Failure on northwestern aspects are largely facilitated by joint delimited wedge failure. The large persistence of discontinuity set J4 allows for wedge failure exceeding 10.000 m^3 on anaclinal slopes, although display limited abundance.

Furthermore, the lithological controls on bedding conditioned failure exceeding 100.000 m^3 were assessed in the probabilistic stability analysis, conducted in accordance with Eurocode recommendations. Lab and in-situ testing of the rock mass delimited the shear strength criterions applied in the modelling of rock mass strength. Analysis emphasizes the degree of fracturing along the J1 fracture surface and emplacement of bedding parallel minor faults as the most important controls for bedding parallel failure. Discontinuity filling on bedding planes and bedding parallel minor faults reveal a large range in thickness, ranging from full- to no rock wall contact (1 mm to 37 cm). Full rock

wall contact does not produce feasible conditions for failure, indicating the importance of filling material thickness. Seismic loading from earthquakes represent a feasible triggering mechanisms for failures.

Furthermore, three fracture delimited instabilities exceeding 100.000 m^3 were identified along the Svelgsegga ridgeline. InSAR data indicate no significant movement within either of the scenarios. It is recommended that a full hazard assessment is conducted to elaborate the conditions of stability and consequence of failure.

References

AGLIARDI, F., ZANCHI, A. & CROSTA, G. B. 2009. Tectonic vs. gravitational morphostructures in the central Eastern Alps (Italy): Constraints on the recent evolution of the mountain range. *Tectonophysics,* 474**,** 250-270.

ANDERSEN, T., EIDE, E. & WALDERHAUG, H. 1997. The age and tectonic significance of dolerite dykes in western Norway. *Journal of the Geological Society,* 154**,** 961-973.

BALLANTYNE, C. K. 2002. Paraglacial geomorphology. *Quaternary Science Reviews,* 21**,** 1935-2017.

BALLANTYNE, C. K., SANDEMAN, G. F., STONE, J. O. & WILSON, P. 2014. Rock-slope failure following Late Pleistocene deglaciation on tectonically stable mountainous terrain. *Quaternary Science Reviews,* 86**,** 144-157.

BARTON, N. 1973. *Barton, 1973. A review of the shear strength of filled discontinuities in rock. Bergmekanikk, Oslo*.

BARTON, N. The shear strength of rock and rock joints. International Journal of rock mechanics and mining sciences & Geomechanics abstracts, 1976. Elsevier, 255-279.

BARTON, N. & BANDIS, S. 1982. Effects of block size on the shear behaviour of jointed rock. 23rd US Symp. on Rock Mechanics. *Berkeley, CA***,** 739-760.

BARTON, N. & CHOUBEY, V. 1977. The shear strength of rock joints in theory and practice. *Rock mechanics,* 10**,** 1-54.

BJERRUM, L. & JRSTAD, F. 1968. Stability of rock slopes in Norway. *Norwegian Geotechnical Institute Publ*.

BLAIS-STEVENS, A., BEHNIA, P., KREMER, PAGE, KUNG, R. & AND 2012. Landslide susceptibility mapping of the Sea to Sky transportation corridor, British Columbia, Canada: Comparison of two methods. *Bulletin of Engineering Geology and the Environment,* 71**,** 447-466.

BLIKRA, L., LONGVA, O., BRAATHEN, A., ANDA, E., DEHLS, J. & STALSBERG, K. 2006. Rock slope failures in Norwegian fjord areas: examples, spatial distribution and temporal pattern. *Landslides from massive rock slope failure.* Springer.

BLIKRA, L. H. & CHRISTIANSEN, H. H. 2014. A field-based model of permafrost-controlled rockslide deformation in northern Norway. *Geomorphology,* 208**,** 34-49.

BOORE, D. M. 1972. A note on the effect of simple topography on seismic SH waves. *Bulletin of the seismological Society of America,* 62**,** 275-284.

BOORE, D. M. 1973. The effect of simple topography on seismic waves: implications for the accelerations recorded at Pacoima Dam, San Fernando Valley, California. *Bulletin of the seismological society of America,* 63**,** 1603-1609.

BOUCHON, M. 1973. Effect of topography on surface motion. *Bulletin of the Seismological Society of America,* 63**,** 615-632.

BRAATHEN, A. 1999. Kinematics of post-Caledonian polyphase brittle faulting in the Sunnfjord region, western Norway. *Tectonophysics,* 302**,** 99-121.

BROWN, E. & HOEK, E. 1980. *Underground excavations in rock*, CRC Press.

BROWN, E. T. 1981. *Rock characterization testing and monitoring*, Pergamon press.

BRYHNI, I. 1978. Flood deposits in the Hornelen Basin, west Norway (Old Red Sands tone) *Norsk Geologisk Tidsskrift* Vol. 58.

BUNGUM, H., LINDHOLM, C. & FALEIDE, J. 2005. Postglacial seismicity offshore mid-Norway with emphasis on spatio-temporal–magnitudal variations. *Marine and Petroleum Geology,* 22**,** 137-148.

BÖHME, M. 2014. *Spatial and temporal variability of rock slope instability in western Norway : implications for susceptibility and hazard assessment.* 2014:82,

Norwegian University of Science and Technology, Faculty of Engineering Science and Technology, Department of Geology and Mineral Resources Engineering.
BÖHME, M., HERMANNS, R. L., OPPIKOFER, T., FISCHER, L., BUNKHOLT, H. S., EIKEN, T., PEDRAZZINI, A., DERRON, M.-H., JABOYEDOFF, M. & BLIKRA, L. H. 2013. Analyzing complex rock slope deformation at Stampa, western Norway, by integrating geomorphology, kinematics and numerical modeling. *Engineering geology,* 154**,** 116-130.
BÖHME, M., OPPIKOFER, T., LONGVA, O., JABOYEDOFF, M., HERMANNS, R. & DERRON, M.-H. 2015. Analyses of past and present rock slope instabilities in a fjord valley: Implications for hazard estimations. *Geomorphology,* 248**,** 464-474.
CARDINALI, M., CARRARA, A., GUZZETTI, F. & PAOLA, R. 2002. Landslide Hazard Map of The Upper Tiber River Basin, Central Italy.
CARRARA, A., CARDINALI, M. & GUZZETTI, F. 1992. Uncertainty in assessing landslide hazard and risk. *ITC journal***,** 172-183.
CRUDEN, D. 1989. Limits to common toppling. *Canadian Geotechnical Journal,* 26**,** 737-742.
CRUDEN, D. M. 2003. The shapes of cold, high mountains in sedimentary rocks. *Geomorphology,* 55**,** 249-261.
CRUDEN, D. M. & HU, X. Q. 1996. Hazardous modes of rock slope movement in the Canadian Rockies. *Environmental & Engineering Geoscience,* 2**,** 507-516.
DEERE, D. U. & MILLER, R. 1966. Engineering classification and index properties for intact rock. Illinois Univ At Urbana Dept Of Civil Engineering.
DEVOLI, G., EIKENÆS, O., TAURISANO, A., HERMANNS, R., FISCHER, L., OPPIKOFER, T. & BUNKHOLT, H. 2011. *Plan for skredfarekartlegging - Delrapport steinsprang, steinskred og fjellskred*.
DEWEY, J. F., RYAN, P. D. & ANDERSEN, T. B. 1993. Orogenic uplift and collapse, crustal thickness, fabrics and metamorphic phase changes: the role of eclogites. *Geological Society, London, Special Publications,* 76**,** 325.
DEWEZ, T. J. B., GIRARDEAU-MONTAUT, D., ALLANIC, C. & ROHMER, J. 2016. FACETS : A CLOUDCOMPARE PLUGIN TO EXTRACT GEOLOGICAL PLANES FROM UNSTRUCTURED 3D POINT CLOUDS. *Int. Arch. Photogramm. Remote Sens. Spatial Inf. Sci.,* XLI-B5**,** 799-804.
DSB 2011. Guidelines for technical regulations according to the

planning and construction law,—Chapter 7: safety requirements

regarding nature disasters (in Norwegian). *In:* PUBLIC, D. F. & (DSB), P. (eds.). Oslo.
EBERHARDT, E. 2003. Rock slope stability analysis–utilization of advanced numerical techniques. *Earth and Ocean sciences at UBC*.
EIDE, E., TORSVIK, T. & ANDERSEN, T. 1997. Absolute dating of brittle fault movements: Late Permian and late Jurassic extensional fault breccias in western Norway. *Terra Nova,* 9**,** 135-139.
EIDE, E. A., TORSVIK, T. H., ANDERSEN, T. B. & ARNAUD, N. O. 1999. Early Carboniferous Unroofing in Western Norway: A Tale of Alkali Feldspar Thermochronology. *The Journal of Geology,* 107**,** 353-374.
EVANS, S. G. & CLAGUE, J. J. 1994. Recent climatic change and catastrophic geomorphic processes in mountain environments. *Geomorphology and Natural Hazards.* Elsevier.
FOSSEN, H. 1992. The role of extensional tectonics in the Caledonides of south Norway. *Journal of Structural Geology,* 14**,** 1033-1046.
FOSSEN, H. Advances tn understanding the post-Caledonian structural evolution of the Bergen area, West Norway. 1998.
FOSSEN, H. & DUNLAP, W. J. 1999. On the age and tectonic significance of Permo-Triassic dikes in the Bergen-Sunnhordland region, southwestern Norway. *Norsk Geologisk Tidsskrift,* 79**,** 169-178.
FRATTINI, P., CROSTA, G., CARRARA, A. & AGLIARDI, F. 2008. Assessment of rockfall susceptibility by integrating statistical and physically-based approaches. *Geomorphology,* 94**,** 419-437.

GALADINI, F. 2006. Quaternary tectonics and large-scale gravitational deformations with evidence of rock-slide displacements in the Central Apennines (central Italy). *Geomorphology,* 82**,** 201-228.
GEERTSEMA, M., CLAGUE, J. J., SCHWAB, J. W. & EVANS, S. G. 2006. An overview of recent large catastrophic landslides in northern British Columbia, Canada. *Engineering geology,* 83**,** 120-143.
GELI, L., BARD, P.-Y. & JULLIEN, B. 1988. The effect of topography on earthquake ground motion: a review and new results. *Bulletin of the Seismological Society of America,* 78**,** 42-63.
GLASTONBURY, J. & FELL, R. 2010. Geotechnical characteristics of large rapid rock slides. *Canadian Geotechnical Journal,* 47**,** 116-132.
GOODMAN, R. 1970. The deformability of joints. *Determination of the in situ Modulus of Deformation of rock.* ASTM International.
GOODMAN, R. E. Toppling of rock slopes. Proc. Speciality Conference on Rock Engineering for Foundation and Slopes, 1976. ASCE, 201-234.
GRÄMIGER, L., MOORE, J. R., GISCHIG, V. S. & LOEW, S. Paraglacial rock mass damage during repeat glacial cycles in preparing slope instabilities (Aletsch region, Switzerland). EGU General Assembly Conference Abstracts, 2016. EPSC2016-15114.
GRØNENG, G. 2010. *Stability analyses of the Åknes Rock Slope, Western Norway.* 2010:30, Norwegian University of Science and Technology, Faculty of Engineering Science and Technology, Department of Geology and Mineral Resources Engineering.
GUZZETTI, F., CARDINALI, M. & REICHENBACH, P. 1996. The influence of structural setting and lithology on landslide type and pattern. *Environmental & Engineering Geoscience,* 2**,** 531-555.
GÜNTHER, A. 2003. SLOPEMAP: programs for automated mapping of geometrical and kinematical properties of hard rock hill slopes. *Computers & Geosciences,* 29**,** 865-875.
HAEBERLI, W. 1997. Slope stability problems related to glacier shrinkage and permafrost degradation in the Alps. *Eclogae Geologicae Helvetiae,* 90**,** 407-414.
HARBOR, J. M., HALLET, B. & RAYMOND, C. F. 1988. A numerical model of landform development by glacial erosion. *Nature,* 333**,** 347-349.
HARDIE, R. A. 2017. PETROGRAPHIC EXAMINATION OF

A ROCK SAMPLE, Bremanger Quarry

Norway. Heath & Hardie Geosciences Ltd.
HARTZ, E. & ANDRESEN, A. 1997. From collision to collapse: Complex strain permutation in the hinterland of the Scandinavian Caledonides. *Journal of Geophysical Research,* 1022**,** 24697-24710.
HAWKINS, A. 1998. Aspects of rock strength. *Bulletin of Engineering Geology and the Environment,* 57**,** 17-30.
HEIM, A. 1932. *Bergsturz und menschenleben*, Fretz & Wasmuth.
HENDERSON, I. H. C. & SAINTOT, A. 2011. Regional spatial variations in rockslide distribution from structural geology ranking: an example from Storfjorden, western Norway. *Geological Society, London, Special Publications,* 351**,** 79-95.
HERMANNS, R., HANSEN, L., SLETTEN, K., BÖHME, M., BUNKHOLT, H., DEHLS, J., EILERTSEN, R., FISCHER, L., L'HEUREUX, J.-S., HØGAAS, F., NORDAHL, B., OPPIKOFER, T., RUBENSDOTTER, L., SOLBERG, I.-L., STALSBERG, K. & YUGSI MOLINA, F. X. 2013a. Systematic geological mapping for landslide understanding in the Norwegian context.
HERMANNS, R., OPPIKOFER, T., ANDA, E., BLIKRA, L., BÖHME, M., BUNKHOLT, H., CROSTA, G., DAHLE, H., DEVOLI, G., FISCHER, L., JABOYEDOFF, M., LOEW, S., SÆTRE, S. & YUGSI MOLINA, F. X. 2012. *Recommended hazard and risk classification system for large unstable rock slopes in Norway*.
HERMANNS, R. L., BLIKRA, L. H., ANDA, E., SAINTOT, A., DAHLE, H., OPPIKOFER, T., FISCHER, L., BUNKHOLT, H., BÖHME, M. & DEHLS, J. F. 2013b. Systematic

mapping of large unstable rock slopes in Norway. *Landslide science and practice.* Springer.
HERMANNS, R. L. & LONGVA, O. 2012. Rapid rock-slope failures. *Landslides: types, mechanisms and modeling***,** 59-70.
HERMANNS, R. L., SCHLEIER, M., BÖHME, M., BLIKRA, L. H., GOSSE, J., IVY-OCHS, S. & HILGER, P. Rock-avalanche activity in W and S Norway peaks after the retreat of the Scandinavian Ice Sheet. Workshop on World Landslide Forum, 2017. Springer, 331-338.
HOEK, E. 2000. Practical rock engineering.
HOEK, E. & BRAY, J. 1981a. Graphical presentation of geological data. Rock Slope Engineering. *Institution of Mining and Metallurgy, Spon Press. London*.
HOEK, E. & BRAY, J. D. 1981b. *Rock slope engineering*, CRC Press.
HOEK, E. & BROWN, E. 1980a. Graphical presentation of geological data. *underground excavations in rock. London: Instn. Min. Metall***,** 61-86.
HOEK, E. & BROWN, E. T. 1980b. Empirical strength criterion for rock masses. *Journal of the geotechnical engineering division,* 106**,** 1013-1035.
HOEK, E., CARRANZA-TORRES, C. & CORKUM, B. 2002. Hoek-Brown failure criterion-2002 edition. *Proceedings of NARMS-Tac,* 1**,** 267-273.
HORN, H. & DEERE, D. 1962. Frictional characteristics of minerals. *Geotechnique,* 12**,** 319-335.
HUGGEL, C., SALZMANN, N., ALLEN, S., CAPLAN-AUERBACH, J., FISCHER, L., HAEBERLI, W., LARSEN, C., SCHNEIDER, D. & WESSELS, R. 2010. Recent and future warm extreme events and high-mountain slope stability. *Philosophical Transactions of the Royal Society A: Mathematical, Physical and Engineering Sciences,* 368**,** 2435-2459.
HUNGR, O., LEROUEIL, S. & PICARELLI, L. 2014. The Varnes classification of landslide types, an update. *Landslides,* 11**,** 167-194.
HØEG, K., LIED, K., KARLSRUD, K., GREGORY, T. & NORGES GEOTEKNISKE, I. 2014. *Skred : skredfare og sikringstiltak : praktiske erfaringer og teoretiske prinsipper,* Oslo, NGI Universitetsforl.
JABOYEDOFF, M., AILLIFARD, F., DERRON, M.-H., COUTURE, R., LOCAT, J. & LOCAT, P. 2005. *Switzerland Modular and evolving rock slope hazard assessment methods*.
JABOYEDOFF, M. & DERRON, M.-H. 2005. A new method to estimate the infilling of alluvial sediment of glacial valleys using a sloping local base level. *Geografia Fisica e Dinamica Quaternaria,* 28**,** 37-46.
JABOYEDOFF, M., METZGER, R., OPPIKOFER, T., COUTURE, R., DERRON, M.-H., LOCAT, J. & TURMEL, D. 2007. New insight techniques to analyze rock-slope relief using DEM and 3D-imaging cloud points: COLTOP-3D software.
JABOYEDOFF, M., OPPIKOFER, T., ABELLÁN, A., DERRON, M.-H., LOYE, A., METZGER, R. & PEDRAZZINI, A. 2012. Use of LIDAR in landslide investigations: a review. *Natural hazards,* 61**,** 5-28.
KAYNIA, A. M., TORGERSRUD, Ø., JOHANSSON, J., BRUUN, H. & HAUGEN, E. 2017. Jordskjelvdesign i Statens vegvesen: Anbefalinger for geoteknisk prosjektering av veger og samvirke jord-konstruksjoner. *Statens vegvesens rapporter.*
KENNEY, T. C. 1967. The influence of mineral composition on the residual strength of natural soils.
KRABBENDAM, M. & DEWEY, J. F. 1998. Exhumation of UHP rocks by transtension in the Western Gneiss Region, Scandinavian Caledonides. *Geological Society, London, Special Publications,* 135**,** 159.
KRISTENSEN, L., CZEKIRDA, J., PENNA, I., ETZELMÜLLER, B., NICOLET, P., PULLARELLO, J. S., BLIKRA, L. H., SKREDE, I., OLDANI, S. & ABELLAN, A. 2021. Movements, failure and climatic control of the Veslemannen rockslide, Western Norway. *Landslides*.
KVELDSVIK, V., NILSEN, B., EINSTEIN, H. & NADIM, F. 2008. Alternative approaches for analyses of a 100,000 m 3 rock slide based on Barton–Bandis shear strength criterion. *Landslides,* 5**,** 161-176.

LATO, M., DIEDERICHS, M., HUTCHINSON, D. & HARRAP, R. 2009. Optimization of LiDAR scanning and processing for automated structural evaluation of discontinuities in rockmasses. *International Journal of Rock Mechanics and Mining Sciences - INT J ROCK MECH MINING SCI,* 46**,** 194-199.
LI , C. C. 2018. *Rock Mechanics*, Norwegian University of Science og Technology (NTNU).
LI, C. C. 2018. TGB 4210, Rock Mechanics
LOEW, S., GSCHWIND, S., GISCHIG, V., KELLER-SIGNER, A. & VALENTI, G. 2017. Monitoring and early warning of the 2012 Preonzo catastrophic rockslope failure. *Landslides,* 14**,** 141-154.
LONGLEY, P. A., GOODCHILD, M. F., MAGUIRE, D. J. & RHIND, D. W. 2015. *Geographic information science and systems*, John Wiley & Sons.
MACGREGOR, K. R., ANDERSON, R. S. & WADDINGTON, E. D. 2009. Numerical modeling of glacial erosion and headwall processes in alpine valleys. *Geomorphology,* 103**,** 189-204.
MARINOS, P. & HOEK, E. GSI: a geologically friendly tool for rock mass strength estimation. ISRM international symposium, 2000. International Society for Rock Mechanics and Rock Engineering.
MARKLAND, J. T. 1972. *A useful technique for estimating the stability of rock slopes when the rigid wedge slide type of failure is expected*, Interdepartmental Rock Mechanics Project, Imperial College of Science and ….
MARQUINEZ, J., DUARTE, R. M., FARIAS, P. & SANCHEZ, M. J. 2003. Predictive GIS-based model of rockfall activity in mountain cliffs. *Natural Hazards,* 30**,** 341-360.
MARTINO, S., MOSCATELLI, M. & MUGNOZZA, G. S. 2004. Quaternary mass movements controlled by a structurally complex setting in the central Apennines (Italy). *Engineering Geology,* 72**,** 33-55.
MARZORATI, S., LUZI, L. & DE AMICIS, M. 2002. Rock falls induced by earthquakes: a statistical approach. *Soil Dynamics and Earthquake Engineering,* 22**,** 565-577.
MASOUMI, H., DOUGLAS, K., SAYDAM, S. & HAGAN, P. Experimental study of size effects of rock on UCS and point load tests. 46th US Rock Mechanics/Geomechanics Symposium, 2012. American Rock Mechanics Association.
MCBRIDE, E. F. 1963. A classification of common sandstones. *Journal of Sedimentary Research,* 33**,** 664-669.
MEENTEMEYER, R. & MOODY, A. 2000. Automated mapping of alignment between topography and geologic bedding planes. *Comput Geosci,* 26**,** 815-829.
MENÉNDEZ-DUARTE, R. & MARQUÍNEZ, J. 2002. The influence of environmental and lithologic factors on rockfall at a regional scale: an evaluation using GIS. *Geomorphology,* 43**,** 117-136.
MO, K. 2018. *Stability Analysis of Preikestolen.* NTNU.
MYRVANG, A. 2001. Kompendium i Bergmekanikk. *Norwegian University of Science and Technology, department of Geology and Mineral Resources, Trondheim*.
MÖRNER, N.-A. 1996. Liquefaction and varve deformation as evidence of paleoseismic events and tsunamis. The autumn 10,430 BP case in Sweden. *Quaternary Science Reviews,* 15**,** 939-948.
NILSEN, B. 2000. New trends in rock slope stability analyses. *Bulletin of Engineering Geology and the Environment,* 58**,** 173-178.
NILSEN, B. 2017. Rock slope stability analysis according to Eurocode 7, discussion of some dilemmas with particular focus on limit equilibrium analysis. *Bulletin of Engineering Geology and the Environment,* 76**,** 1229-1236.
NILSEN, B., LINDSTRØM, M., MATHIESEN, T., HOLMØY, K., OLSSON, R. & PALMSTRØM, A. 2011. Veileder for bruk av Eurokode 7 til bergteknisk prosjektering. *URL: https://bergmekanikk. no/wp-content/uploads/2014/02/Veiledning-Eurokode-7-Versjon-1-november-2011. pdf (Hentet: 10.03. 2019)*.
NILSEN, B. & PALMSTRÖM, A. 2000. *Engineering Geology and Rock Engineering: Handbook No. 2*, Norwegian Group for Rock Mechanics.
NORTON, M. G. 1987. The Nordfjord-Sogn Detachment, W. Norway. *Norsk Geologisk Tidsskrift,* 67.

NOVÁK, D. 2014. *Local Relief Model (LRM) Toolbox for ArcGIS (UPDATE 2016-05 - new download link)*.
NVE 2019. Bransjestandard for kartlegging av fare for steinsprang og steinskred. *Vedlegg 1 - Steinsprang og steinskred.* NVE.
NVE. 2020. *NVE Atlas* [Online]. Available: https://atlas.nve.no/Html5Viewer/index.html?viewer=nveatlas# [Accessed].
ODLING, N. E. & LARSEN, Ø. 2000. Vein architecture in the Devonian sandstones of the Hornelen basin, western Norway, and implications for the palaeostrain history. *Norsk Geologisk Tidsskrift,* 80**,** 289-299.
OPPIKOFER, T. 2009. *Detection, analysis and monitoring of slope movements by high-resolution digital elevation models.* Université de Lausanne, Faculté des géosciences et de l'environnement.
OSMUNDSEN, ANDERSEN, MARKUSSEN & SVENDBY 1998. Tectonics and sedimentation in the hangingwall of a major extensional detachment: the Devonian Kvamshesten Basin, western Norway. *Basin Research,* 10**,** 213-234.
PATTON, F. D. Multiple modes of shear failure in rock. 1st ISRM Congress, 1966. International Society for Rock Mechanics and Rock Engineering.
PEDRAZZINI, A. 2012. *Characterization of gravitational rock slope deformations at different spatial scales based on field, remote sensing and numerical approaches.* Université de Lausanne, Faculté des géosciences et de l'environnement.
PEDRAZZINI, A., HUMAIR, F., JABOYEDOFF, M. & TONINI, M. 2016. Characterisation and spatial distribution of gravitational slope deformation in the Upper Rhone catchment (Western Swiss Alps). *Landslides,* 13**,** 259-277.
PERSAUD, M. & PFIFFNER, O.-A. 2004. Active deformation in the eastern Swiss Alps: post-glacial faults, seismicity and surface uplift. *Tectonophysics,* 385**,** 59-84.
RADBRUCH-HALL, D. H. 1978. Gravitational creep of rock masses on slopes. *Developments in Geotechnical Engineering.* Elsevier.
RICHARDS, L., LEG, G. & WHITTLE, R. 1978. Appraisal of stability conditions in rock slopes. *Foundation engineering in difficult ground. Newnes-Butterworths, London***,** 449-512.
ROCSCIENCE. 2021. *Joint Strength in an SWedge Probabilistic Analysis* [Online]. Available: https://www.rocscience.com/help/swedge/swedge/joint_strength_(probabilistic).htm [Accessed 24.03 2021].
ROSSI, M., GUZZETTI, F., REICHENBACH, P., MONDINI, A. C. & PERUCCACCI, S. 2010. Optimal landslide susceptibility zonation based on multiple forecasts. *Geomorphology,* 114**,** 129-142.
RUFF, M. & CZURDA, K. 2008. Landslide susceptibility analysis with a heuristic approach in the Eastern Alps (Vorarlberg, Austria). *Geomorphology,* 94**,** 314-324.
SANTANGELO, M., MARCHESINI, I., CARDINALI, M., FIORUCCI, F., ROSSI, M., BUCCI, F. & GUZZETTI, F. 2015. A method for the assessment of the influence of bedding on landslide abundance and types. *Landslides,* 12**,** 295-309.
SELBY, M. J. 1975. SLOPES. By Anthony Young. Edinburgh: Oliver and Boyd, 1972. *New Zealand Geographer,* 31.
SELBY, M. J., AUGUSTINUS, P., MOON, V. G. & STEVENSON, R. J. 1988. Slopes on strong rock masses: modelling and influences of stress distributions and geomechanical properties. *Modelling geomorphological systems***,** 341-374.
SERANNE, M. & SEGURET, M. 1987. The Devonian basins of western Norway: tectonics and kinematics of an extending crust. *Geological Society, London, Special Publications,* 28**,** 537.
SHAN, J. & TOTH, C. K. 2018. *Topographic laser ranging and scanning: principles and processing*, CRC press.
SHIRZADI, A., SARO, L., JOO, O. H. & CHAPI, K. 2012. A GIS-based logistic regression model in rock-fall susceptibility mapping along a mountainous road: Salavat Abad case study, Kurdistan, Iran. *Natural hazards,* 64**,** 1639-1656.
SKEMPTON, A. 1964. Long-term stability of clay slopes. *Geotechnique,* 14**,** 77-102.

STANDARD-NORGE 2014a. Eurokode 8: Prosjektering av konstruksjonar for seismisk påvirkning : Del 5: Fundamenter, støttekonstruksjoner og geotekniske forhold.
STANDARD-NORGE 2014b. Eurokode 8: Prosjektering av konstruksjonar for seismisk påvirkning : Samling av Nasjonale tillegg. Lysaker.
STEAD, D. & COGGAN, J. 2012. 13 Numerical modeling of rock-slope instability. *Landslides: Types, mechanisms and modeling***,** 144.
STEAD, D. & EBERHARDT, E. 2013. Understanding the mechanics of large landslides. *Ital. J. Eng. Geol. Environ. Book Ser,* 6**,** 85-112.
STEAD, D., EBERHARDT, E. & COGGAN, J. S. 2006. Developments in the characterization of complex rock slope deformation and failure using numerical modelling techniques. *Engineering Geology,* 83**,** 217-235.
STEEL, R. J. 1976. Devonian basins of western norway - sedimentary response to tectonism and to varying tectonic context. *Tectonophysics,* 36**,** 207-224.
STURZENEGGER, M. & STEAD, D. 2009. Quantifying discontinuity orientation and persistence on high mountain rock slopes and large landslides using terrestrial remote sensing techniques. *Natural Hazards and Earth System Sciences,* 9.
TANARRO, L. M. & MUÑOZ, J. 2012. Rockfalls in the Duratón canyon, central Spain: Inventory and statistical analysis. *Geomorphology,* 169-170**,** 17-29.
TERZAGHI, K. 1962. Stability of Steep Slopes on Hard Unweathered Rock. *Geotechnique,* 12**,** 251-270.
THIELE, S. T., GROSE, L., SAMSU, A., MICKLETHWAITE, S., VOLLGGER, S. A. & CRUDEN, A. R. 2017. Rapid, semi-automatic fracture and contact mapping for point clouds, images and geophysical data. *Solid Earth,* 8**,** 1241-1253.
THIERY, Y., MALET, J.-P., STERLACCHINI, S., PUISSANT, A. & MAQUAIRE, O. 2007. Landslide susceptibility assessment by bivariate methods at large scales: application to a complex mountainous environment. *Geomorphology,* 92**,** 38-59.
TORSVIK, T. H., STURT, B. A., RAMSAY, D. M., BERING, D. & FLUGE, P. R. 1988. Palaeomagnetism, magnetic fabrics and the structural style of the Hornelen Old Red Sandstone, Western Norway. *Journal of the Geological Society,* 145**,** 413.
TRAVELLETTI, J., DEMAND, J., JABOYEDOFF, M. & MARILLIER, F. 2010. Mass movement characterization using a reflexion and refraction seismic survey with the sloping local base level concept. *Geomorphology,* 116**,** 1-10.
TØNSET, L. 2019. *Verdien av kjerneborehull for økt forståelse av stabilitetsforhold ved Åknes skredområde.* NTNU.
VARNES, D. J. 1978. Slope movement types and processes. *Special report,* 176**,** 11-33.
VELARDI, G., HERMANNS, R., PENNA, I. & BÖHME, M. Prediction of the reach of rock slope failures based on empirical data from Norway. ISRM International Symposium-EUROCK 2020, 2020. International Society for Rock Mechanics and Rock Engineering.
VESTØL, O. 2006. Determination of postglacial land uplift in Fennoscandia from leveling, tide-gauges and continuous GPS stations using least squares collocation. *Journal of Geodesy,* 80**,** 248-258.
VICK, L. M., BÖHME, M., ROUYET, L., BERGH, S. G., CORNER, G. D. & LAUKNES, T. R. 2020. Structurally controlled rock slope deformation in northern Norway. *Landslides,* 17**,** 1745-1776.
WENNBERG, O., MILNES, A. & WINSVOLD, I. 1998. The northern Bergen Are Shear Zone - an oblique-lateral ramp In the Devonian extensional detachment system of western Norway. *Norsk Geologisk Tiddsskrift,* 78**,** 169-184.
WILKS, W. J. & CUTHBERT, S. J. 1994. The evolution of the Hornelen Basin detachment system, western Norway: Implications for the style of late orogenic extension in the southern Scandinavian Caledonides. *Tectonophysics,* 238**,** 1-30.
WONG, H. & JENNINGS, P. 1975. Effects of canyon topography on strong ground motion. *Bulletin of the Seismological Society of America,* 65**,** 1239-1257.
WYLLIE, D. C. 2004. *Rock slope engineering : civil and mining,* London, Spon Press.
WYLLIE, D. C. & MAH, C. 2004. *Rock slope engineering : civil and mining,* London, Spon Press.

ZAHIRI, H., PALAMARA, D. R., FLENTJE, P., BRASSINGTON, G. M. & BAAFI, E. 2006. A GIS-based weights-of-evidence model for mapping cliff instabilities associated with mine subsidence. *Environmental Geology,* 51**,** 377-386.
ØVSTEDAL, E. 1971. TUNNEL PÅ FYLKESVEGEN SVELGEN - SANDE Sikring av rasfarlig parti. Oslo: Staten Vegvesen.

6 Appendix

6.1 Appendix A – Structural analysis

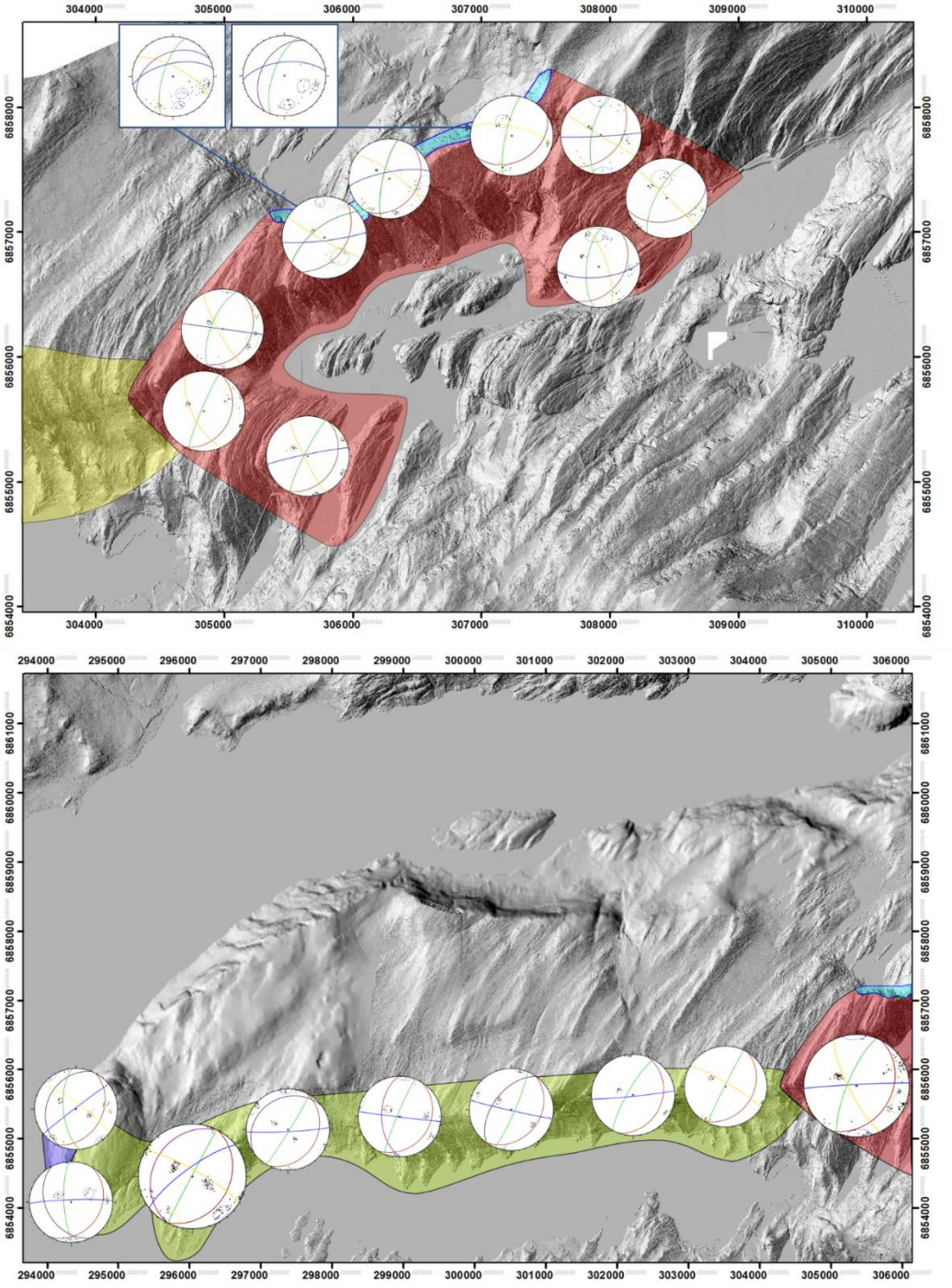

Figure 6.1 *Structural measurement stations. Enlarged stereo nets represents data from three stations to limit clutter. Remote structural measurements on ALS models are indicated with blue outline.*

6.2 Appendix B – NVE Skredhendelser

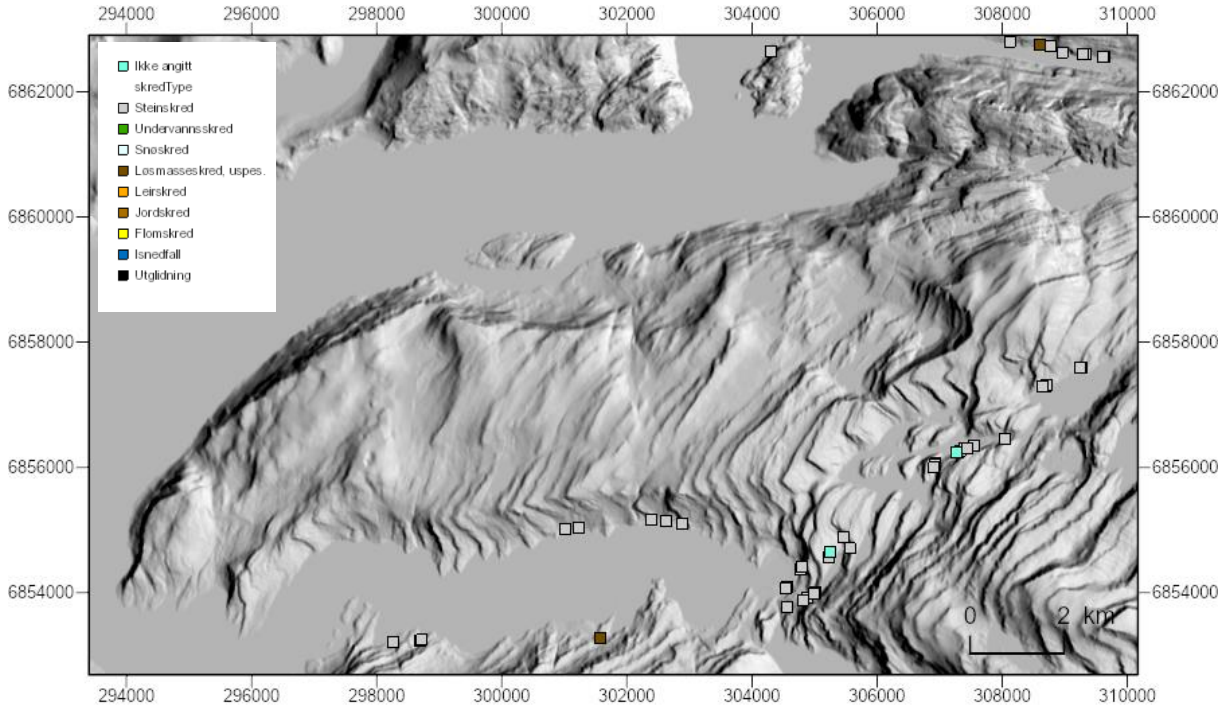

Figure 6.2 *Registered landslide events in the NVE Atlas database (NVE, 2020).*

6.3 Appendix C – Coltop3D method vs. Compass method

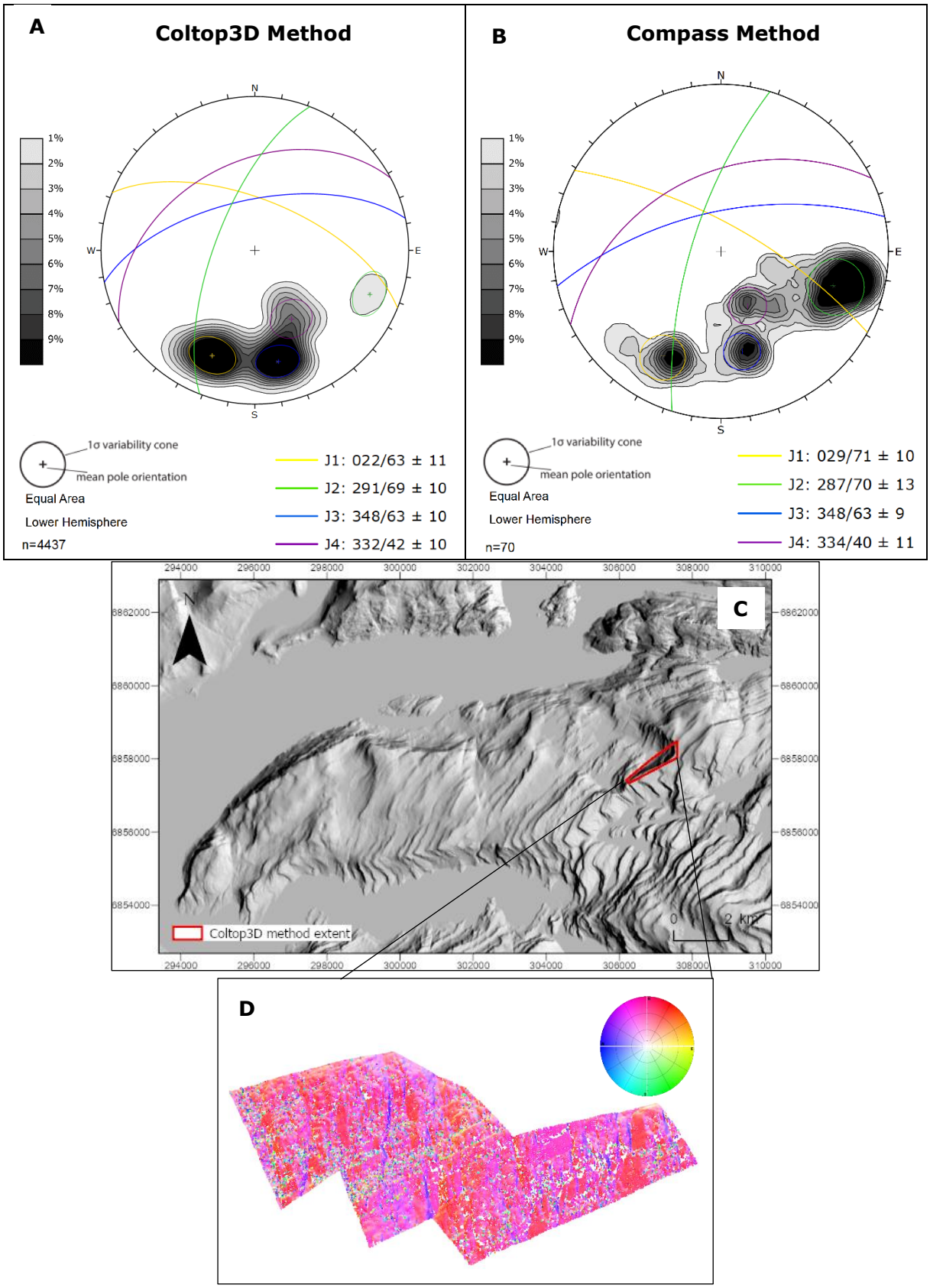

Figure 3.4 *(A) Structural measurements collected using the Coltop3D method. (B) Structural measurements collected using the Compass method. (C) Extent of the survey area for the Coltop3D and Compass datasets. (D) Coltop3D projection of the slope.*

6.4 Appendix D – InSAR data

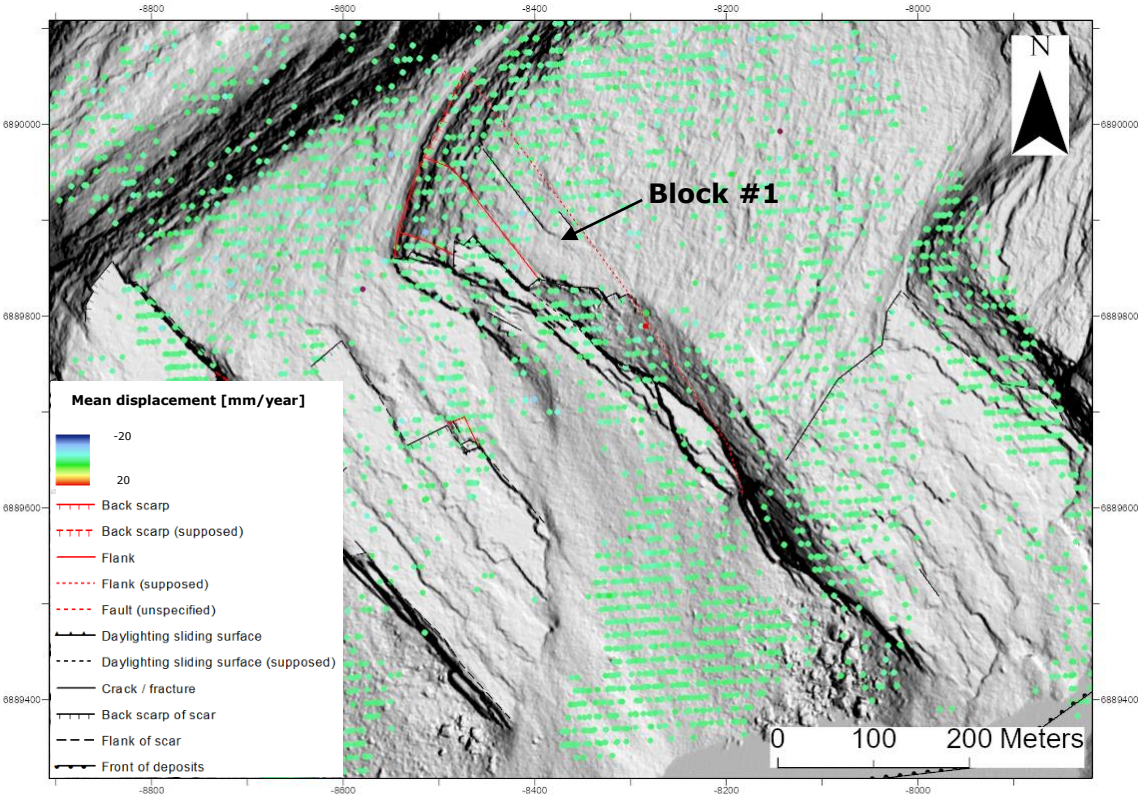

Figure *InSAR data from Sentinel ascending satellite for block #1 (NGU, 2021).*

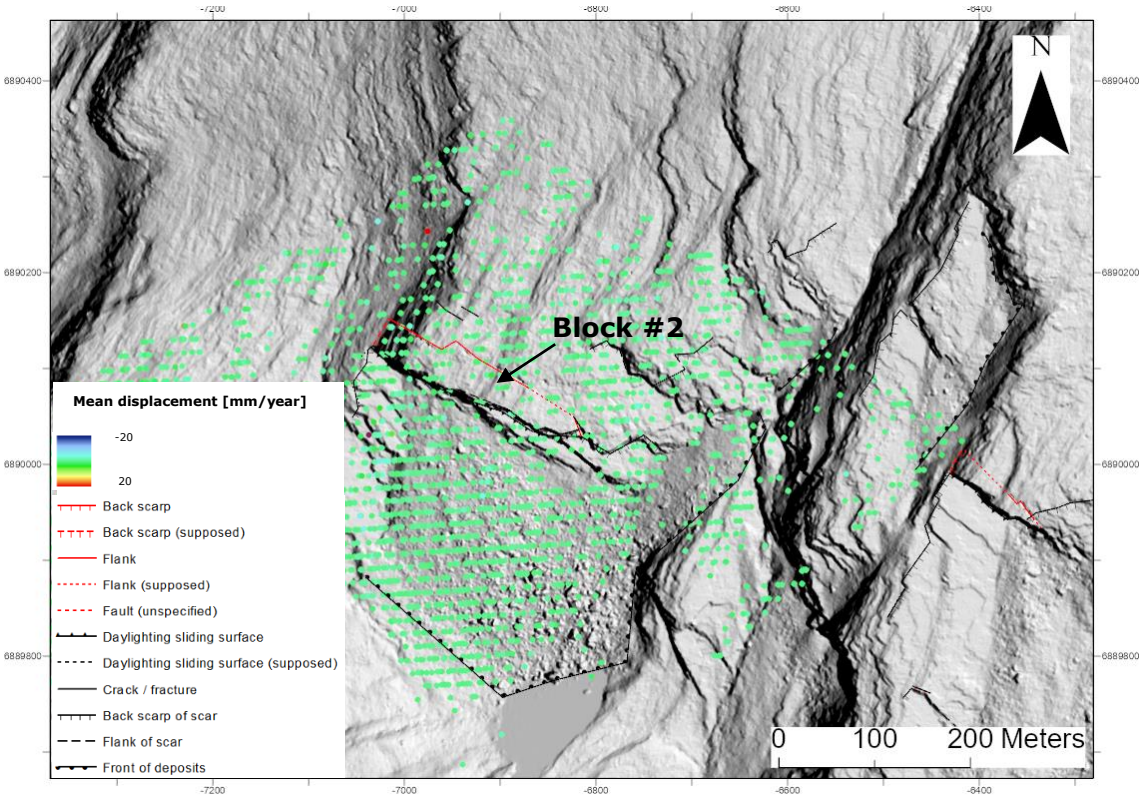

Figure *InSAR data from Sentinel ascending satellite for block #2 (NGU, 2021).*

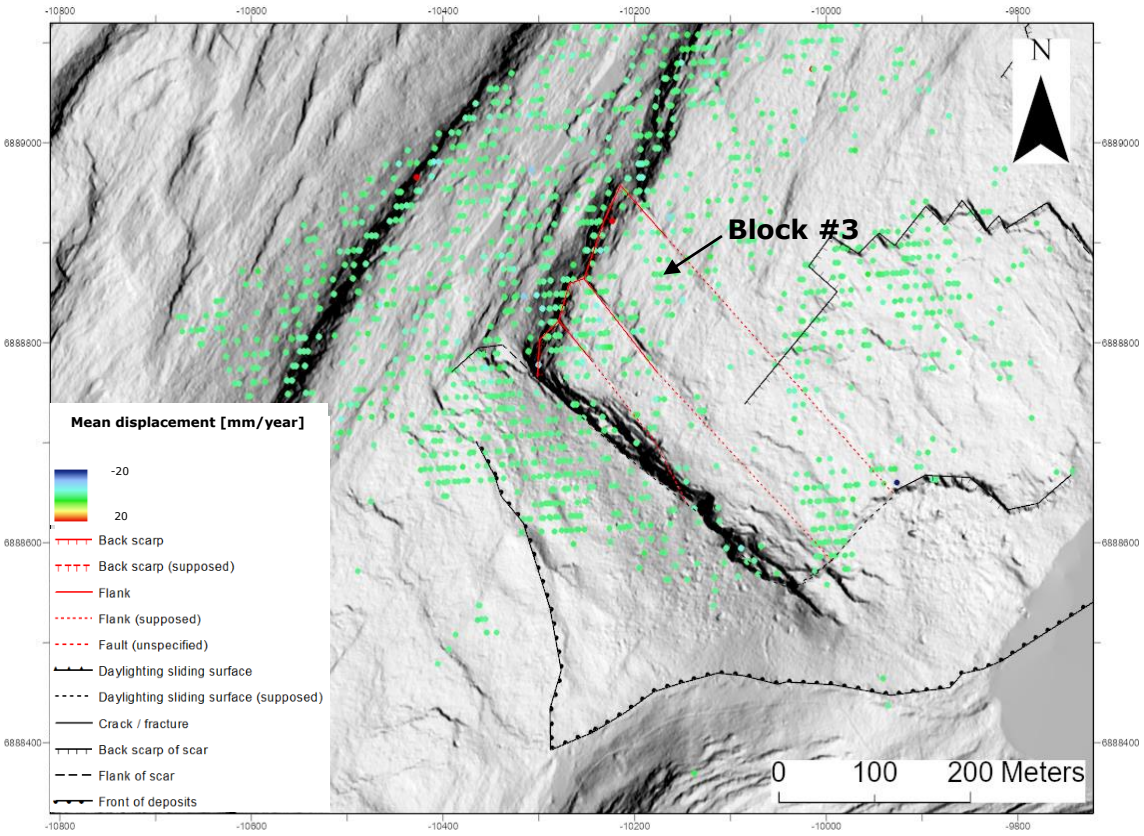

Figure *InSAR data from Sentinel ascending satellite for block #3 (NGU, 2021).*

Martin Valand Feldmann

NTNU
Kunnskap for en bedre verden

NORGES GEOLOGISKE UNDERSØKELSE
NGU